Searches for the Higgs boson decaying to W[superscript +]W[superscript -] → #[superscript +]##[superscript -][¯ over v] with the CDF II detector

Searches for the Higgs boson decaying to $W^+W^- \to \ell^+\nu\ell^-\bar{\nu}$ with the CDF II detector

T. Aaltonen,[22] S. Amerio,[41a] D. Amidei,[33] A. Anastassov,[16,y] A. Annovi,[18] J. Antos,[13] G. Apollinari,[16] J. A. Appel,[16] T. Arisawa,[55] A. Artikov,[14] J. Asaadi,[50] W. Ashmanskas,[16] B. Auerbach,[2] A. Aurisano,[50] F. Azfar,[40] W. Badgett,[16] T. Bae,[26] A. Barbaro-Galtieri,[27] V. E. Barnes,[45] B. A. Barnett,[24] P. Barria,[43c,43a] P. Bartos,[13] M. Bauce,[41b,41a] F. Bedeschi,[43a] S. Behari,[16] G. Bellettini,[43b,43a] J. Bellinger,[57] D. Benjamin,[15] A. Beretvas,[16] G. Bertoli,[51a] A. Bhatti,[47] K. R. Bland,[5] B. Blumenfeld,[24] A. Bocci,[15] A. Bodek,[46] D. Bortoletto,[45] J. Boudreau,[44] A. Boveia,[12] L. Brigliadori,[6b,6a] C. Bromberg,[34] E. Brucken,[22] J. Budagov,[14] H. S. Budd,[46] K. Burkett,[16] G. Busetto,[41b,41a] P. Bussey,[20] P. Butti,[43b,43a] A. Buzatu,[20] A. Calamba,[11] S. Camarda,[4] M. Campanelli,[29] F. Canelli,[12,16,ee] A. Canepa,[32] B. Carls,[23] D. Carlsmith,[57] R. Carosi,[43a] S. Carrillo,[17,n] B. Casal,[10,l] M. Casarsa,[51a] A. Castro,[6b,6a] P. Catastini,[21] D. Cauz,[51a] V. Cavaliere,[23] M. Cavalli-Sforza,[4] A. Cerri,[27,f] L. Cerrito,[29,t] Y. C. Chen,[1] M. Chertok,[7] G. Chiarelli,[43a] G. Chlachidze,[16] K. Cho,[26] D. Chokheli,[14] M. A. Ciocci,[43c,43a] A. Clark,[19] C. Clarke,[56] M. E. Convery,[16] J. Conway,[7] M. Corbo,[16] M. Cordelli,[18] C. A. Cox,[7] D. J. Cox,[7] M. Cremonesi,[43a] D. Cruz,[50] J. Cuevas,[10,aa] R. Culbertson,[16] N. d'Ascenzo,[16,x] M. Datta,[16,gg] P. De Barbaro,[46] L. Demortier,[47] M. Deninno,[6a] M. d'Errico,[41b,41a] F. Devoto,[22] A. Di Canto,[43b,43a] B. Di Ruzza,[16,r] J. R. Dittmann,[5] M. D'Onofrio,[28] S. Donati,[43b,43a] M. Dorigo,[51b,51a] A. Driutti,[51a] K. Ebina,[55] R. Edgar,[33] A. Elagin,[50] R. Erbacher,[7] S. Errede,[23] B. Esham,[23] R. Eusebi,[50] S. Farrington,[40] J. P. Fernández Ramos,[30] R. Field,[17] G. Flanagan,[16,v] R. Forrest,[7] M. Franklin,[21] J. C. Freeman,[16] H. Frisch,[12] Y. Funakoshi,[55] A. F. Garfinkel,[45] P. Garosi,[43c,43a] H. Gerberich,[23] E. Gerchtein,[16] S. Giagu,[48a] V. Giakoumopoulou,[3] K. Gibson,[44] C. M. Ginsburg,[16] N. Giokaris,[3] P. Giromini,[18] G. Giurgiu,[24] V. Glagolev,[14] D. Glenzinski,[16] M. Gold,[36] D. Goldin,[50] A. Golossanov,[16] G. Gomez,[10] G. Gomez-Ceballos,[31] M. Goncharov,[31] O. González López,[30] I. Gorelov,[36] A. T. Goshaw,[15] K. Goulianos,[47] E. Gramellini,[6a] S. Grinstein,[4] C. Grosso-Pilcher,[12] R. C. Group,[52,16] J. Guimaraes da Costa,[21] S. R. Hahn,[16] J. Y. Han,[46] F. Happacher,[18] K. Hara,[52] M. Hare,[53] R. F. Harr,[56] T. Harrington-Taber,[16,o] K. Hatakeyama,[5] C. Hays,[40] J. Heinrich,[42] M. Herndon,[57] D. Hidas,[49] A. Hocker,[16] Z. Hong,[50] W. Hopkins,[16,g] S. Hou,[1] S.-C. Hsu,[27] R. E. Hughes,[37] U. Husemann,[58] M. Hussein,[34,h] J. Huston,[34] G. Introzzi,[43e,43a] M. Iori,[48b,48a] A. Ivanov,[7,q] E. James,[16] D. Jang,[11] B. Jayatilaka,[16] E. J. Jeon,[26] S. Jindariani,[16] M. Jones,[45] K. K. Joo,[26] S. Y. Jun,[11] T. R. Junk,[16] M. Kambeitz,[25] T. Kamon,[25,50] P. E. Karchin,[56] A. Kasmi,[5] Y. Kato,[39,p] W. Ketchum,[12,hh] J. Keung,[42] B. Kilminster,[16,ee] D. H. Kim,[26] H. S. Kim,[26] J. E. Kim,[26] M. J. Kim,[18] S. B. Kim,[26] S. H. Kim,[52] Y. J. Kim,[26] Y. K. Kim,[12] N. Kimura,[55] M. Kirby,[16] K. Knoepfel,[16] K. Kondo,[55,a] D. J. Kong,[26] J. Konigsberg,[17] A. V. Kotwal,[15] M. Kreps,[25] J. Kroll,[42] M. Kruse,[15] T. Kuhr,[25] M. Kurata,[52] A. T. Laasanen,[45] S. Lammel,[16] M. Lancaster,[29] K. Lannon,[37,z] G. Latino,[43c,43a] H. S. Lee,[26] J. S. Lee,[26] S. Leo,[43a] S. Leone,[43a] J. D. Lewis,[16] A. Limosani,[15,u] E. Lipeles,[42] A. Lister,[19,b] H. Liu,[54] Q. Liu,[45] T. Liu,[16] S. Lockwitz,[58] A. Loginov,[58] A. Lucà,[18] D. Lucchesi,[41b,41a] J. Lueck,[25] P. Lujan,[27] P. Lukens,[16] G. Lungu,[47] J. Lys,[27] R. Lysak,[13,e] R. Madrak,[16] P. Maestro,[43c,43a] S. Malik,[47] G. Manca,[28,c] A. Manousakis-Katsikakis,[3] F. Margaroli,[48a] P. Marino,[43d,43a] M. Martínez,[4] K. Matera,[23] M. E. Mattson,[56] A. Mazzacane,[16] P. Mazzanti,[6a] R. McNulty,[28,k] A. Mehta,[28] P. Mehtala,[22] C. Mesropian,[47] T. Miao,[16] D. Mietlicki,[33] A. Mitra,[1] H. Miyake,[52] S. Moed,[16] N. Moggi,[6a] C. S. Moon,[16,bb] R. Moore,[16,ff] M. J. Morello,[43a,43d] S. Mrenna,[16] A. Mukherjee,[16] Th. Muller,[25] P. Murat,[16] M. Mussini,[6b,6a] J. Nachtman,[16,o] Y. Nagai,[52] J. Naganoma,[55] I. Nakano,[38] A. Napier,[53] J. Nett,[50] C. Neu,[54] M. S. Neubauer,[23] T. Nigmanov,[44] L. Nodulman,[2] S. Y. Noh,[26] O. Norniella,[23] L. Oakes,[40] S. H. Oh,[15] Y. D. Oh,[26] I. Oksuzian,[54] T. Okusawa,[39] R. Orava,[22] L. Ortolan,[4] S. Pagan Griso,[27] C. Pagliarone,[51a] E. Palencia,[10,f] P. Palni,[36] V. Papadimitriou,[16] W. Parker,[57] G. Pauletta,[51c,51a] M. Paulini,[11] C. Paus,[31] T. J. Phillips,[15] G. Piacentino,[43a] E. Pianori,[42] J. Pilot,[37] K. Pitts,[23] C. Plager,[8] L. Pondrom,[57] S. Poprocki,[16,g] K. Potamianos,[27] A. Pranko,[27] F. Prokoshin,[14,cc] F. Ptohos,[18,i] G. Punzi,[43b,43a] J. Pursley,[57] N. Ranjan,[45] I. Redondo Fernández,[30] P. Renton,[40] M. Rescigno,[48a] F. Rimondi,[6a,a] L. Ristori,[43a,16] A. Robson,[20] T. Rodriguez,[42] S. Rolli,[53,j] M. Ronzani,[43b,43a] R. Roser,[16] J. L. Rosner,[12] F. Ruffini,[43c,43a] A. Ruiz,[10] J. Russ,[11] V. Rusu,[16] W. K. Sakumoto,[46] Y. Sakurai,[55] L. Santi,[51c,51a] K. Sato,[52] V. Saveliev,[16,x] A. Savoy-Navarro,[16,bb] P. Schlabach,[16] E. E. Schmidt,[16] T. Schwarz,[33] L. Scodellaro,[10] F. Scuri,[43a] S. Seidel,[36] Y. Seiya,[39] A. Semenov,[14] F. Sforza,[43b,43a] S. Z. Shalhout,[7] T. Shears,[28] P. F. Shepard,[44] M. Shimojima,[52,w] M. Shochet,[12] I. Shreyber-Tecker,[35] A. Simonenko,[14] P. Sinervo,[32] K. Sliwa,[53] J. R. Smith,[7] F. D. Snider,[16] H. Song,[44] V. Sorin,[4] M. Stancari,[16] R. St. Denis,[20] B. Stelzer,[32] O. Stelzer-Chilton,[32] D. Stentz,[16,y] J. Strologas,[36] Y. Sudo,[52] A. Sukhanov,[16] I. Suslov,[14] K. Takemasa,[52] Y. Takeuchi,[52] J. Tang,[12] M. Tecchio,[33] P. K. Teng,[1] J. Thom,[16,g] A. S. Thompson,[20] E. Thomson,[42] V. Thukral,[50] D. Toback,[50] S. Tokar,[13] K. Tollefson,[34] T. Tomura,[52] D. Tonelli,[16,f] S. Torre,[18] D. Torretta,[16] P. Totaro,[41a] M. Trovato,[43d,43a] F. Ukegawa,[52] S. Uozumi,[26] F. Vázquez,[17,n] G. Velev,[16] C. Vellidis,[16] C. Vernieri,[43d,43a] M. Vidal,[45] R. Vilar,[10] J. Vizán,[10,dd] M. Vogel,[36] G. Volpi,[18] P. Wagner,[42] R. Wallny,[8] S. M. Wang,[1] A. Warburton,[32] D. Waters,[29] W. C. Wester III,[16] D. Whiteson,[42,d]

A. B. Wicklund,[2] S. Wilbur,[12] H. H. Williams,[42] J. S. Wilson,[33] P. Wilson,[16] B. L. Winer,[37] P. Wittich,[16,g] S. Wolbers,[16] H. Wolfe,[37] T. Wright,[33] X. Wu,[19] Z. Wu,[5] F. Würthwein,[9] K. Yamamoto,[39] D. Yamato,[39] T. Yang,[16] U. K. Yang,[12,s] Y. C. Yang,[26] W.-M. Yao,[27] G. P. Yeh,[16] K. Yi,[16,o] J. Yoh,[16] K. Yorita,[55] T. Yoshida,[39,m] G. B. Yu,[15] I. Yu,[26] A. M. Zanetti,[51a] Y. Zeng,[15] C. Zhou,[15] and S. Zucchelli[6b,6a]

(CDF Collaboration)

[1]*Institute of Physics, Academia Sinica, Taipei, Taiwan 11529, Republic of China*
[2]*Argonne National Laboratory, Argonne, Illinois 60439, USA*
[3]*University of Athens, 157 71 Athens, Greece*
[4]*Institut de Fisica d'Altes Energies, ICREA, Universitat Autonoma de Barcelona, E-08193 Bellaterra (Barcelona), Spain*
[5]*Baylor University, Waco, Texas 76798, USA*
[6a]*Istituto Nazionale di Fisica Nucleare Bologna, I-40127 Bologna, Italy*
[6b]*University of Bologna, I-40127 Bologna, Italy*
[7]*University of California, Davis, California 95616, USA*
[8]*University of California, Los Angeles, California 90024, USA*
[9]*University of California, San Diego, La Jolla, California 92093, USA*
[10]*Instituto de Fisica de Cantabria, CSIC-University of Cantabria, 39005 Santander, Spain*
[11]*Carnegie Mellon University, Pittsburgh, Pennsylvania 15213, USA*
[12]*Enrico Fermi Institute, University of Chicago, Chicago, Illinois 60637, USA*
[13]*Comenius University, 842 48 Bratislava, Slovakia; Institute of Experimental Physics, 040 01 Kosice, Slovakia*
[14]*Joint Institute for Nuclear Research, RU-141980 Dubna, Russia*
[15]*Duke University, Durham, North Carolina 27708, USA*
[16]*Fermi National Accelerator Laboratory, Batavia, Illinois 60510, USA*
[17]*University of Florida, Gainesville, Florida 32611, USA*
[18]*Laboratori Nazionali di Frascati, Istituto Nazionale di Fisica Nucleare, I-00044 Frascati, Italy*
[19]*University of Geneva, CH-1211 Geneva 4, Switzerland*
[20]*Glasgow University, Glasgow G12 8QQ, United Kingdom*
[21]*Harvard University, Cambridge, Massachusetts 02138, USA*
[22]*Division of High Energy Physics, Department of Physics, University of Helsinki and Helsinki Institute of Physics, FIN-00014, Helsinki, Finland*
[23]*University of Illinois, Urbana, Illinois 61801, USA*
[24]*The Johns Hopkins University, Baltimore, Maryland 21218, USA*
[25]*Institut für Experimentelle Kernphysik, Karlsruhe Institute of Technology, D-76131 Karlsruhe, Germany*
[26]*Center for High Energy Physics: Kyungpook National University, Daegu 702-701, Korea; Seoul National University, Seoul 151-742, Korea; Sungkyunkwan University, Suwon 440-746, Korea; Korea Institute of Science and Technology Information, Daejeon 305-806, Korea; Chonnam National University, Gwangju 500-757, Korea; Chonbuk National University, Jeonju 561-756, Korea; Ewha Womans University, Seoul, 120-750, Korea*
[27]*Ernest Orlando Lawrence Berkeley National Laboratory, Berkeley, California 94720, USA*
[28]*University of Liverpool, Liverpool L69 7ZE, United Kingdom*
[29]*University College London, London WC1E 6BT, United Kingdom*
[30]*Centro de Investigaciones Energeticas Medioambientales y Tecnologicas, E-28040 Madrid, Spain*
[31]*Massachusetts Institute of Technology, Cambridge, Massachusetts 02139, USA*
[32]*Institute of Particle Physics: McGill University, Montréal, Québec H3A 2T8, Canada; Simon Fraser University, Burnaby, British Columbia V5A 1S6, Canada; University of Toronto, Toronto, Ontario M5S 1A7, Canada; and TRIUMF, Vancouver, British Columbia V6T 2A3, Canada*
[33]*University of Michigan, Ann Arbor, Michigan 48109, USA*
[34]*Michigan State University, East Lansing, Michigan 48824, USA*
[35]*Institution for Theoretical and Experimental Physics, ITEP, Moscow 117259, Russia*
[36]*University of New Mexico, Albuquerque, New Mexico 87131, USA*
[37]*The Ohio State University, Columbus, Ohio 43210, USA*
[38]*Okayama University, Okayama 700-8530, Japan*
[39]*Osaka City University, Osaka 588, Japan*
[40]*University of Oxford, Oxford OX1 3RH, United Kingdom*
[41a]*Istituto Nazionale di Fisica Nucleare, Sezione di Padova-Trento, I-35131 Padova, Italy*
[41b]*University of Padova, I-35131 Padova, Italy*
[42]*University of Pennsylvania, Philadelphia, Pennsylvania 19104, USA*
[43a]*Istituto Nazionale di Fisica Nucleare Pisa, I-56127 Pisa, Italy*
[43b]*University of Pisa, I-56127 Pisa, Italy*

[43c]*University of Siena, I-56127 Pisa, Italy*
[43d]*Scuola Normale Superiore, I-56127 Pisa, Italy*
[43e]*INFN Pavia and University of Pavia, I-27100 Pavia, Italy*
[44]*University of Pittsburgh, Pittsburgh, Pennsylvania 15260, USA*
[45]*Purdue University, West Lafayette, Indiana 47907, USA*
[46]*University of Rochester, Rochester, New York 14627, USA*
[47]*The Rockefeller University, New York, New York 10065, USA*
[48a]*Istituto Nazionale di Fisica Nucleare, Sezione di Roma 1, I-00185 Roma, Italy*
[48b]*Sapienza Università di Roma, I-00185 Roma, Italy*
[49]*Rutgers University, Piscataway, New Jersey 08855, USA*
[50]*Mitchell Institute for Fundamental Physics and Astronomy, Texas A&M University, College Station, Texas 77843, USA*
[51a]*Istituto Nazionale di Fisica Nucleare Trieste/Udine, I-34127 Trieste, Italy*
[51b]*University of Trieste, I-34127 Trieste, Italy*
[51c]*University of Udine, I-33100 Udine, Italy*
[52]*University of Tsukuba, Tsukuba, Ibaraki 305, Japan*
[53]*Tufts University, Medford, Massachusetts 02155, USA*
[54]*University of Virginia, Charlottesville, Virginia 22906, USA*
[55]*Waseda University, Tokyo 169, Japan*
[56]*Wayne State University, Detroit, Michigan 48201, USA*
[57]*University of Wisconsin, Madison, Wisconsin 53706, USA*
[58]*Yale University, New Haven, Connecticut 06520, USA*
(Received 4 June 2013; published 17 September 2013)

We present a search for a standard model Higgs boson decaying to two W bosons that decay to leptons using the full data set collected with the CDF II detector in $\sqrt{s} = 1.96$ TeV $p\bar{p}$ collisions at the Fermilab Tevatron, corresponding to an integrated luminosity of 9.7 fb^{-1}. We obtain no evidence for production of a standard model Higgs boson with mass between 110 and 200 GeV$/c^2$, and place upper limits on the production cross section within this range. We exclude standard model Higgs boson production at the

[a]Deceased.
[b]Visitor from University of British Columbia, Vancouver, BC V6T 1Z1, Canada.
[c]Visitor from Istituto Nazionale di Fisica Nucleare, Sezione di Cagliari, 09042 Monserrato (Cagliari), Italy.
[d]Visitor from University of California Irvine, Irvine, CA 92697, USA.
[e]Visitor from Institute of Physics, Academy of Sciences of the Czech Republic, 182 21, Czech Republic.
[f]Visitor from CERN, CH-1211 Geneva, Switzerland.
[g]Visitor from Cornell University, Ithaca, NY 14853, USA.
[h]Visitor from The University of Jordan, Amman 11942, Jordan.
[i]Visitor from University of Cyprus, Nicosia CY-1678, Cyprus.
[j]Visitor from Office of Science, U.S. Department of Energy, Washington, DC 20585, USA.
[k]Visitor from University College Dublin, Dublin 4, Ireland.
[l]Visitor from ETH, 8092 Zürich, Switzerland.
[m]Visitor from University of Fukui, Fukui City, Fukui Prefecture, Japan 910-0017.
[n]Visitor from Universidad Iberoamericana, Lomas de Santa Fe, México, C.P. 01219, Distrito Federal.
[o]Visitor from University of Iowa, Iowa City, IA 52242, USA.
[p]Visitor from Kinki University, Higashi-Osaka City, Japan 577-8502.
[q]Visitor from Kansas State University, Manhattan, KS 66506, USA.
[r]Visitor from Brookhaven National Laboratory, Upton, NY 11973, USA.
[s]Visitor from University of Manchester, Manchester M13 9PL, United Kingdom.
[t]Visitor from Queen Mary, University of London, London, E1 4NS, United Kingdom.
[u]Visitor from University of Melbourne, Victoria 3010, Australia.
[v]Visitor from Muons, Inc., Batavia, IL 60510, USA.
[w]Visitor from Nagasaki Institute of Applied Science, Nagasaki 851-0193, Japan.
[x]Visitor from National Research Nuclear University, Moscow 115409, Russia.
[y]Visitor from Northwestern University, Evanston, IL 60208, USA.
[z]Visitor from University of Notre Dame, Notre Dame, IN 46556, USA.
[aa]Visitor from Universidad de Oviedo, E-33007 Oviedo, Spain.
[bb]Visitor from CNRS-IN2P3, Paris, F-75205 France.
[cc]Visitor from Universidad Tecnica Federico Santa Maria, 110v Valparaiso, Chile.
[dd]Visitor from Universite catholique de Louvain, 1348 Louvain-La-Neuve, Belgium.
[ee]Visitor from University of Zürich, 8006 Zürich, Switzerland.
[ff]Visitor from Massachusetts General Hospital and Harvard Medical School, Boston, MA 02114 USA.
[gg]Visitor from Hampton University, Hampton, VA 23668, USA.
[hh]Visitor from Los Alamos National Laboratory, Los Alamos, NM 87544, USA.

95% confidence level in the mass range between 149 and 172 GeV/c^2, while expecting to exclude, in the absence of signal, the range between 155 and 175 GeV/c^2. We also interpret the search in terms of standard model Higgs boson production in the presence of a fourth generation of fermions and within the context of a fermiophobic Higgs boson model. For the specific case of a standard-model-like Higgs boson in the presence of fourth-generation fermions, we exclude at the 95% confidence level Higgs boson production in the mass range between 124 and 200 GeV/c^2, while expecting to exclude, in the absence of signal, the range between 124 and 221 GeV/c^2.

DOI: 10.1103/PhysRevD.88.052012 PACS numbers: 13.85.Rm, 14.80.Bn, 14.80.Ec

I. INTRODUCTION

In the standard model (SM) of particle physics, the electroweak force is characterized by a gauge theory of the $(SU(2)_L \times U(1)_Y)$ symmetry group [1–3]. This symmetry is broken, which introduces differences in the observed phenomenology of electromagnetic and weak interactions. The mechanism of symmetry breaking in the SM is known as the Higgs mechanism [4–7], which introduces a complex doublet of scalar fields. The self-interaction of these fields introduces a potential term in the electroweak Lagrangian, which has a minimum at a nonzero value of the field. At sufficiently low energies (the Fermi scale and below), the electroweak Lagrangian is approximated by an effective Lagrangian, which is no longer symmetric under the full gauge group but rather retains only $U(1)_{EM}$ symmetry, leading to additional terms. Three of these terms are identified with the masses of the $W^{\pm}$ and Z vector bosons, and the fourth results in an associated scalar boson known as the Higgs boson. The masses of the leptons and quarks also require that electroweak symmetry is broken and are generated in the SM through Yukawa interactions with the scalar Higgs field.

Owing to its central position in the understanding of the phenomenology of the electroweak force, the discovery of the Higgs boson [8,9] was an important milestone for particle physics. Properties of the Higgs boson, including production rates and decay branching ratios, are highly sensitive to physics beyond the SM. Many models, such as supersymmetry, require extended Higgs sectors with additional multiplets of scalar fields, resulting in additional Higgs bosons, some of which interact very differently from the SM-predicted Higgs boson.

The possible mass range for the SM Higgs boson (m_H) is constrained by theoretical and experimental results. The W boson mass M_W, the Z boson mass M_Z, and the top-quark mass m_t are modified by self-energy terms involving the Higgs boson as a virtual particle in processes with amplitudes involving one or more loops, which depend on the mass of the Higgs boson. This, in turn, allows for a prediction of the Higgs boson mass using precision measurements of M_W, M_Z, and m_t. The most recent average of available W boson mass measurements is $M_W = 80.385 \pm 0.015$ GeV/c^2 [10], and the most recent average of top-quark mass measurements is $m_t = 173.2 \pm 0.9$ GeV/c^2 [11]. These mass measurements are combined with other precision electroweak measurements to calculate an allowed range of $m_H = 94^{+29}_{-24}$ GeV/c^2 at the 68% confidence level (C.L.) or less than 152 GeV/c^2 at the 95% C.L. [12]. In addition, direct searches at the LEP collider excluded SM Higgs boson production for masses below 114.4 GeV/c^2 at the 95% C.L. [13]. A combination of the direct LEP searches with indirect constraints indicates that the SM Higgs boson should have a mass below 171 GeV/c^2 at the 95% C.L. [12].

A previously unknown boson with a mass of approximately 125 GeV/c^2, compatible with the SM Higgs boson, has been observed in data collected from $\sqrt{s} = 7$–8 TeV pp collisions at the CERN Large Hadron Collider (LHC) by the ATLAS [8] and CMS [9] Collaborations. The new boson was observed with high significance in the ZZ and $\gamma\gamma$ decay modes and at a somewhat lower level of significance in the WW decay mode. Updated ATLAS [14] and CMS [15] searches focusing on $H \to W^+W^-$ decay and using additional data provide strengthened evidence for this decay mode. Since the phenomenology of the Higgs mechanism is characterized by its interactions with W and Z bosons, observation of the Higgs boson in the WW decay mode and refined measurements of the corresponding branching ratio are of critical importance.

For higher Higgs boson masses, $m_H > 130$ GeV/c^2, where the decay to two W bosons dominates [16], a SM Higgs boson is primarily observable at the Tevatron via gluon-fusion production through a top-quark loop (ggH), with subsequent decay to a pair of W^* bosons [17–20]. This decay mode provides a low-background search topology, when both W bosons decay leptonically. The main backgrounds to $H \to W^+W^- \to \ell^+\nu\ell^-\bar{\nu}$ are Drell-Yan (DY) production of oppositely charged leptons, $p\bar{p} \to W^+W^-$, $W^{\pm}Z$, ZZ, $t\bar{t}$, W + jets, and $W + \gamma$ processes. Events consistent with the $\ell^+\nu\ell^-\bar{\nu}$ final state are selected by requiring two oppositely charged leptons and a significant overall imbalance in measured transverse energies within the event (missing transverse energy or $\not\!\!E_T$). CDF reconstructs electrons and muons with high efficiency and minimal contamination from jets misidentified as leptons (fakes). We treat separately tau leptons decaying hadronically, which are harder to reconstruct and significantly contaminated with fakes. Missing transverse energy associated with the unobserved neutrinos provides discrimination against

backgrounds that do not contain leptonically decaying W bosons, such as DY production.

A potential Higgs boson signal is distinguishable from the other background processes with real $\not\!\!E_T$ generated from neutrinos based on unique kinematic properties associated with the Higgs boson decay. The fact that the Higgs boson is a scalar particle induces a spin correlation between the W bosons, which manifests itself as a preference for the charged leptons in the final state to be emitted in similar directions to one another. The nonresonant $p\bar{p} \to W^+W^-$ background has a very different spin structure [21], resulting in a different distribution of the angle between the two charged leptons.

In addition to the ggH production mechanism, the SM Higgs boson is expected to be produced in association with a W or Z vector boson (WH, ZH, or, collectively, VH production), and in vector boson fusion (VBF), where a virtual pair of W bosons or Z bosons fuse to form a Higgs boson, usually with recoiling jets. Including these additional production mechanisms expands acceptance by approximately 50% for $m_H = 160$ GeV$/c^2$, compared to searching for only the ggH production process [22]. These additional production mechanisms were included in the most recent CDF results [23], which were combined with similar results from the D0 Collaboration [24] to exclude at 95% C.L. a SM Higgs boson in the mass range between 162 and 166 GeV$/c^2$ [25].

For lower Higgs boson masses, $m_H < 130$ GeV$/c^2$, the decay $H \to b\bar{b}$ dominates. A direct search for the SM Higgs boson in the process $gg \to H \to b\bar{b}$ would be overwhelmed by nonresonant, multijet backgrounds. Hence, Tevatron searches in this mass region focus on the $WH \to \ell\nu b\bar{b}$ [26,27], $ZH \to \ell^+\ell^- b\bar{b}$ [28,29], and $ZH \to \nu\bar{\nu}b\bar{b}$ [30,31] processes. The combination of Tevatron searches in these decay modes [32] resulted in first evidence for VH production in association with $H \to b\bar{b}$ decay. Despite the low SM Higgs boson branching ratio to W bosons within this mass range, the WW decay mode still contributes significantly to combined Tevatron search sensitivities because it is accessible within a final state originating from ggH production.

In this paper we present a search for the production of SM Higgs bosons with subsequent decay to two oppositely charged $W^{(*)}$ bosons using a sample of $\sqrt{s} = 1.96$ TeV proton-antiproton ($p\bar{p}$) collision data corresponding to 9.7 fb^{-1} of integrated luminosity collected with the CDF II detector at the Fermilab Tevatron. This result improves on previous CDF results [23,33–35] by including more data, using improved analysis techniques, and incorporating additional search topologies such as dilepton pairs with invariant mass below 16 GeV$/c^2$ and trilepton events from VH production, where the third lepton results from the decay of the associated weak vector boson.

This paper is organized as follows. Section II describes the phenomenology of Higgs boson production and decay, Sec. III describes the analysis strategy, Sec. IV describes the CDF II detector, Sec. V describes the event selection, Sec. VI describes the background modeling, Sec. VII describes the multivariate techniques used to separate the expected signal events from the background events, Sec. VIII describes each analysis sample, Sec. IX summarizes systematic uncertainties on signal and background predictions, and Sec. X describes the procedures used for interpreting the data and the final results.

II. PHENOMENOLOGY OF HIGGS BOSON PRODUCTION AND DECAY

Higgs boson searches in hadron collisions rely both on accurate predictions of Higgs boson production and decay rates and on accurate kinematic modeling of the resulting events. The theoretical community has provided calculations of all relevant signal production cross sections at next-to-next-to-leading order (NNLO) accuracy in the strong-interaction coupling constant α_s, and also differential cross sections for ggH production at the same order. These calculations, in conjunction with Monte Carlo simulation tools for modeling the signal and background processes as well as the response of the CDF II detector to the particles originating from these processes, are critical inputs to this search.

The dominant Higgs boson production mechanism over the mass range of interest in $p\bar{p}$ collisions is ggH. Because of the large Yukawa coupling of the top quark to the Higgs boson, the largest contribution to the cross section comes from the top-quark-loop amplitude. However, loops involving other quark flavors are incorporated within the calculations. Calculations of the inclusive cross section for ggH production in hadron collisions have progressed from leading order (LO) [36], to next-to-leading order (NLO) [37–39], to NNLO [40–42], and finally to the NNLO calculations described in Refs. [43,44], which are used here.

The expected cross section for this process ranges from 1385 fb at $m_H = 110$ GeV$/c^2$ to 189.1 fb at $m_H = 200$ GeV$/c^2$ [43,44], as summarized in Table I. These cross section predictions are obtained from calculations at NNLO in perturbative QCD, incorporating contributions from both top- and bottom-quark loops, effects of finite quark masses, electroweak contributions from two-loop diagrams [45], interference effects from mixing of electroweak and QCD contributions [44], leading logarithmic resummation of soft gluon contributions [43,46], and MSTW2008 NNLO parton distribution functions (PDFs) [47]. Consistent results are obtained from calculations based on substantially different techniques and independent groups.

The NLO prediction for the ggH production cross section at the Tevatron is typically a factor of 2 larger than the LO prediction, and the NNLO prediction is another factor of 1.4 larger. Uncertainties in the NNLO cross section

TABLE I. (N)NLO production cross sections and decay branching ratios to W^+W^- for the SM Higgs boson, ggH production cross sections and decay branching ratios to W^+W^- for the SM-like Higgs boson in SM4, and the decay branching ratios to W^+W^- for the fermiophobic Higgs boson in FHM as functions of Higgs boson mass.

m_H (GeV/c^2)	σ_{ggH} (fb)	σ_{WH} (fb)	σ_{ZH} (fb)	σ_{VBF} (fb)	$\mathcal{B}(H \to W^+W^-)$ (%)	$\sigma_{ggH}^{\mathrm{SM4}}$ (fb)	$\mathcal{B}^{\mathrm{SM4}}(H \to W^+W^-)$ (%)	$\mathcal{B}^{\mathrm{FHM}}(H \to W^+W^-)$ (%)
110	1385	204	120	82.8	4.82	12310	2.83	85.3
115	1216	175	104	76.5	8.67	10730	5.05	86.6
120	1072	150	90.2	70.7	14.3	9384	8.34	86.9
125	949.3	130	78.5	65.3	21.6	8240	12.9	86.8
130	842.9	112	68.5	60.5	30.5	7259	18.8	86.7
135	750.8	97.2	60.0	56.0	40.3	6414	26.0	86.6
140	670.6	84.6	52.7	51.9	50.4	5684	34.6	86.8
145	600.6	73.7	46.3	48.0	60.3	5050	44.3	87.4
150	539.1	64.4	40.8	44.5	69.9	4499	55.3	88.6
155	484.0	56.2	35.9	41.3	79.6	4018	68.1	90.9
160	432.3	48.5	31.4	38.2	90.9	3595	85.0	95.1
165	383.7	43.6	28.4	36.0	96.0	3221	94.2	97.5
170	344.0	38.5	25.3	33.4	96.5	2893	95.2	97.5
175	309.7	34.0	22.5	31.0	95.8	2604	94.8	96.6
180	279.2	30.1	20.0	28.7	93.2	2349	92.5	93.9
185	252.1	26.9	17.9	26.9	84.4	2122	83.1	84.8
190	228.0	24.0	16.1	25.1	78.6	1920	77.1	78.8
195	207.2	21.4	14.4	23.3	75.7	1740	74.5	75.9
200	189.1	19.1	13.0	21.7	74.1	1580	73.0	74.2

calculation are evaluated by studying the effect on the result of factorization and renormalization scale choices. The largest variation is obtained when the two scales are varied together. We take an uncertainty on the production cross section corresponding to the shift observed when these scales are varied upwards and downwards by factors of 2. Calculations that have been performed including the primary amplitudes at next-to-next-to-next-to leading order indicate that no additional large modification of the cross section is expected [48].

The NNLO generator programs FEHIP [49,50] and HNNLO [51,52] and studies based on these programs [53] are used to tune the leading order simulation, which models the kinematic properties of final state particles originating from ggH production, and to assess systematic uncertainties associated with this modeling.

In the search described here, events are separated into samples in which the leptonically decaying W^+W^- system is observed to recoil against zero-, one-, or two-or-more parton jets. Jet reconstruction, discussed in Sec. V, collects the energy depositions associated with particles produced in the hadronization and fragmentation of partons originating from the $p\bar{p}$ interaction. We normalize the yields of simulated ggH events based on the inclusive cross section calculations described above, but assign differential uncertainties incorporating calculations of the exclusive one-or-more parton jet and two-or-more parton jet cross sections from Refs. [53,54], respectively. We follow the prescription of Refs. [55,56], propagating scale uncertainties associated with the inclusive cross section, the one-or-more parton jet cross section, and the two-or-more parton jet cross section through the subtractions needed to obtain the exclusive zero-, one-, and two-or-more parton jet cross sections. We follow the prescription of Refs. [57,58] in evaluating the effects of PDF uncertainties on the production cross sections.

This search includes substantial additional acceptance for the Higgs boson by incorporating potential signal contributions from VH and VBF production. The cross sections for these production processes are roughly $\mathcal{O}(0.1)$ of those for ggH production. In the mass range between 110 to 200 GeV/c^2, the WH, ZH, and VBF production cross sections vary from 204 to 19.1 fb, 120 to 13.0 fb, and 82.8 to 21.7 fb, respectively, as summarized in Table I.

The cross sections for VH and VBF production have been calculated at NNLO in Refs. [59–63] and [61,64,65], respectively. The VBF cross sections are adjusted for electroweak corrections computed at NLO in Refs. [66,67]. All calculations are based on MSTW2008 NNLO parton distribution functions [47]. Uncertainties on VH and VBF production cross sections are typically much lower than those associated with ggH cross section calculations due to the smaller amount of color in the quark initial states, the pure tree-level electroweak nature of the lowest-order amplitudes, as well as their dependence on quark PDFs, which are known more precisely than the gluon PDF at high Bjorken x.

The VH and VBF production mechanisms result in signal events with topologies and kinematic distributions strikingly different than those associated with ggH production. A significant fraction of these events have partons in the final state additional to the Higgs boson decay products. Leptonic decays of the vector boson produced in association with a Higgs boson that decays to W^+W^- leads to events with three or four charged leptons or, in other cases, in which one of the W bosons from the Higgs boson decays hadronically, to dilepton events containing two leptons with the same charge. Although the production rates associated with these types of events are small, the resulting event topologies are minimally contaminated by other SM backgrounds. Overall, the inclusion of the additional Higgs boson production mechanisms increases the sensitivity of the search by roughly 30%.

The decay branching ratios used in this search are listed in Table I [58]. The partial widths for all decay processes are computed with HDECAY [16] with the exception of those that result in four fermion ($4f$) final states, $H \to W^+W^- \to 4f$ and $H \to ZZ \to 4f$, for which the partial widths are computed with PROPHECY4F [68,69]. Branching ratios are computed from the relative fractions of the total partial widths. The SM branching ratio for a Higgs boson decaying to a pair of W bosons, which is 4.82% at $m_H = 110\ \mathrm{GeV}/c^2$, becomes dominant for $m_H > 135\ \mathrm{GeV}/c^2$, increasing to above 90% near the threshold to produce both W bosons on mass shell at $m_H = 160\ \mathrm{GeV}/c^2$ and decreasing to 74% at $m_H = 200\ \mathrm{GeV}/c^2$, where decay to two Z bosons becomes significant.

Extensions to the SM can significantly modify the Higgs boson production cross sections and the $H \to W^+W^-$ branching ratio. If the SM is extended to include a fourth sequential generation of heavy fermions (SM4), ggH production of a SM-like Higgs boson is significantly enhanced and branching ratios are modified [70]. Table I lists ggH production cross sections for the SM4 model assuming masses of $400\ \mathrm{GeV}/c^2$ and $450\,\mathrm{GeV}/c^2 + 10\ln(m_H/115)\,\mathrm{GeV}/c^2$ for fourth-generation down-type and up-type quarks, respectively [71]. Modified branching ratios for $H \to W^+W^-$ within the SM4 model assuming that the fourth-generation charged lepton and neutrino are sufficiently heavy to be inaccessible as Higgs boson decay products are also listed in Table I.

In the case of a fermiophobic (FHM) Higgs boson, the ggH production cross section is highly suppressed, but as shown in Table I, the $H \to W^+W^-$ branching ratio is significantly larger than in the SM, particularly in the mass range $110 < m_H < 150\ \mathrm{GeV}/c^2$ [72]. In the FHM model, the WH, ZH, and VBF production cross sections are assumed to be the same as those in the SM.

III. ANALYSIS STRATEGY

The single most challenging aspect of searching for the Higgs boson in the $H \to W^+W^- \to \ell^+\nu\ell^-\bar{\nu}$ ($\ell = e,\ \mu$) decay channel is the very small production rate of these events. Even when incorporating tau lepton decays to electrons and muons, we expect, based on production cross sections and branching ratios, 170 signal events to be produced in Tevatron collisions corresponding to an integrated luminosity of 10 fb^{-1}, for a SM Higgs boson of mass $m_H = 125\ \mathrm{GeV}/c^2$. The search sensitivity depends on the fraction of these events that can be retained for final analysis. We select events containing two reconstructed charged leptons and an overall imbalance in measured transverse energies originating from the multiple neutrinos. After applying a loose set of kinematic criteria to the most inclusive two-charged-lepton candidate sample, we select about 25% of the available signal.

Since the remaining background contributions are typically $\mathcal{O}(10^2)$ times larger than that of the expected signal, simple event counting is not feasible. We construct detailed models for the kinematic distributions of events originating from each of the various signal and SM background processes. Based on these models, potential signal events within the data sample are identified by exploiting differences between the kinematic properties of signal and background events. To obtain the best possible signal-to-background separation, candidate events are classified into multiple subsamples tailored to isolate contributions from specific signal and background production processes. Potential signal in each sample is then isolated using multivariate techniques, which offer increased search sensitivity relative to conventional approaches based on one-dimensional selection requirements on directly observed quantities. The multivariate techniques allow for simultaneous analysis of multiple kinematic input variables and the correlations between them.

IV. THE CDF II DETECTOR

The Collider Detector at Fermilab (CDF) [73–77] is a general-purpose particle detector with a cylindrical layout and azimuthal and forward-backward symmetry [78].

The silicon tracking system (SVX) [79–82] and open-cell drift chamber (COT) [83] are used to measure the momenta of charged particles and identify secondary vertices from the decays of bottom quarks, which have finite lifetimes. The COT is segmented into eight concentric superlayers of wire planes with alternating axial and $\pm 2°$ stereo angle stringing. The active volume covers the radial range from 40 to 137 cm and is located within a superconducting solenoid with a 1.4 T magnetic field parallel to the beam axis. Tracking efficiency within the COT is nearly 100% in the range $|\eta| \leq 1$; and with the addition of silicon detector information, tracks can be reconstructed within the wider range of $|\eta| < 1.8$. The momentum resolution is $\sigma(p_T)/p_T^2 \approx 0.001\ \mathrm{GeV}^{-1}$ for tracks within $|\eta| \leq 1$ and degrades with increasing $|\eta|$.

Electromagnetic (EM) and hadronic (HAD) calorimeters [84–86], which are lead-scintillator and iron-scintillator

sampling devices, respectively, surround the solenoid and measure the energy flow of interacting particles. They are segmented into projective towers, each one covering a small range in pseudorapidity and azimuth. The calorimeters have complete azimuthal coverage over $|\eta| < 3.6$. The central region $|\eta| < 1.1$ is covered by the central electromagnetic calorimeter (CEM) and the central and end-wall hadronic calorimeters. The forward region $1.1 < |\eta| < 3.6$ is covered by the end-plug electromagnetic calorimeter (PEM) and the end-plug hadronic calorimeter (PHA).

Energy deposition in the electromagnetic calorimeters is used to identify and measure the energy of electrons and photons. The energy resolution for an electron with transverse energy E_T (measured in GeV) is given by $\sigma(E_T)/E_T \approx 13.5\%/\sqrt{E_T} \oplus 1.5\%$ and $\sigma(E_T)/E_T \approx 16.0\%/\sqrt{E_T} \oplus 1\%$ for those identified in the CEM and PEM, respectively. Deposits in the electromagnetic and hadronic calorimeter towers are used to identify and measure the energies of the clustered groups of particles originating from parton showers (jets). The resolution of calorimeter jet energy measurements is approximately $\sigma(E_T) \approx 0.1E_T + 1.0$ GeV [87]. The CEM and PEM calorimeters also contain strip detectors with two-dimensional readout, which are located at the depth corresponding approximately to the maximum shower development for an electron. These detectors aid in the identification of electrons and photons by providing position information that helps to distinguish them from π^0 decay products.

Beyond the calorimeters are muon detectors [88], which provide muon identification in the range $|\eta| < 1.5$. Muons are detected in four separate subdetectors. Central muons with $p_T > 1.4$ GeV/c penetrate on average the five absorption lengths of the calorimeter and are detected in the four layers of planar multiwire drift chambers of the central muon detector (CMU). A second set of drift chambers, the central muon upgrade (CMP), sits behind an additional 60 cm of steel and detects muons with $p_T > 2.2$ GeV/c. The CMU and CMP chambers cover an equivalent range in pseudorapidity, $|\eta| < 0.6$. Central muon extension (CMX) chambers cover the pseudorapidity range from $0.6 < |\eta| < 1.0$ and thus complete muon system coverage over the full fiducial region of the COT. Muons in the pseudorapidity range $1.0 < |\eta| < 1.5$ are detected in the forward barrel muon chambers.

The Tevatron collider luminosity at the CDF interaction point is determined using multicell gas Cherenkov detectors [89] located in the pseudorapidity range $3.7 < |\eta| < 4.7$, which measure the average number of inelastic $p\bar{p}$ collisions per bunch crossing.

The CDF on-line event selection system (trigger) is designed with three sequential decision levels to cope with high event rates. The first level relies on dedicated hardware to reduce high event rates from the effective beam-crossing frequency of 1.7 MHz to roughly 15 kHz. The second level uses a mixture of dedicated hardware and fast software algorithms to analyze more completely the available trigger information. This level reduces the event rate to roughly 1 kHz, the maximum detector-readout rate. The third level is an array of computers that run a fast version of the off-line event reconstruction algorithms on the full detector readout, selecting events for permanent storage at a rate of up to 150 Hz.

V. EVENT SELECTION

The search is based on events containing two or three charged-lepton candidates with $p_T > 10$ GeV/c. Events are recorded on-line if they meet the criteria of either one of two single-electron triggers or one of four single-muon triggers. The central electron trigger requires a CEM energy cluster with $E_T > 18$ GeV matched to a reconstructed COT track with $p_T > 8$ GeV/c. The forward electron trigger requires a PEM energy cluster with $E_T > 20$ GeV and an overall missing transverse energy of at least 15 GeV in the calorimeter. The four muon triggers are based on track segments in one or more muon chambers (CMU + CMP, CMU, CMP, and CMX) matched to reconstructed COT tracks with $p_T > 18$ GeV/c. For each event, the charged lepton consistent with having satisfied the trigger is required to have $p_T > 20$ GeV/c, to ensure uniform trigger efficiency. Trigger efficiencies are measured from observed $W \to \ell\nu$ and $Z \to \ell\ell$ decays [90]. To ensure that the charged-lepton candidates are consistent with having been produced in a single interaction, the z positions of each candidate's reconstructed track at the point of closest approach to the beam line are required to lie within 4 cm of one another. In addition, the few events containing reconstructed leptons with energies in excess of 400 GeV, which are in total less than 0.1% of the sample and consistent with expected rates from track mismeasurements, are removed.

A. Lepton identification

Electron and muon candidates are constructed from combinations of measurements in various subdetectors. Because the coverage of these subdetectors varies over η and ϕ, selection criteria for individual lepton candidates depend on their trajectory within the detector. The general goal is to use all available information to suppress contributions from jets misidentified as leptons, while not rejecting candidates just because they are detected in less instrumented portions of the detector. As a result, we use four categories of electron candidates, eight categories of muon candidates, and two final categories of candidates likely to be either an electron or muon but indistinguishable on the basis of available information.

1. Electron identification

Identification of electron candidates is based on reconstructed showers in the EM calorimeter with a E_T of at

least 10 GeV after correcting for energy leakage into the HAD calorimeter. For the central region ($|\eta| < 1.1$), we employ both a cut-based and a multivariate likelihood-based method, combining information from the calorimeter, tracking, and shower-maximum detectors. The cut-based method requires that the shower energy within the HAD calorimeter (E_{HAD}) must be less than 5% of that in the EM calorimeter (E_{EM}) and that the distribution of shower energies in the calorimeter towers and shower-maximum detector is consistent with those of an electron. The shower orientation must be geometrically matched to a reconstructed track with a measured p_T such that the ratio of the shower E_T to the track p_T lies between 0.5 and 2.0. The track is also required to pass standard quality requirements.

If a central electron candidate fails the above selection, it can still be used as a likelihood-based electron. The likelihood function is constructed based on variables used in the cut-based version such as the ratio of E_{HAD} to E_{EM}, the ratio of E_T to p_T, and the shapes of calorimeter and shower-maximum energy distributions. Signal likelihood templates are constructed from the unbiased electron candidates in $Z \to ee$ events. Background likelihood templates are constructed from loose electron candidates in inclusive dijet events.

A combination of cut-based and likelihood-based selections is used to identify electron candidates in the forward region of the calorimeter, $1.2 < |\eta| < 2.0$. A specialized track-finding algorithm that uses locations of the reconstructed calorimeter shower and primary vertex to define a search road for hits in the SVX is used to increase the selection efficiency. A similar set of kinematic and shower shape variables to those employed in central electron selection are used as the basis for the cut-based selection and as inputs in the formation of a forward-candidate likelihood function.

2. Muon identification

Muon candidates are constructed from reconstructed tracks with $p_T > 10$ GeV/c. Eight separate categories of reconstructed muon candidates are used. In six of these, the track can be matched with hits from one or more of the muon detector systems. The separate categories are for candidates associated with hits in both central muon detectors, in only the inner or outer central muon detectors, where the track trajectory is consistent with having passed through an uninstrumented gap in the other, in one of two portions of the extended muon detector, and in the forward muon detector. This categorization provides a mechanism for matching muon candidates with specific sets of event triggering criteria. Muon candidate tracks are also required to point toward calorimeter energy depositions consistent with those expected from a minimum-ionizing particle. The last two muon categories apply to tracks matched only to energy depositions consistent with having originated from minimum-ionizing particles in either the central ($|\eta| < 1.1$) or forward ($1.2 < |\eta| < 2.0$) calorimeters. The inclusion of these categories ensures high selection efficiencies for muons that pass through regions of missing muon detector coverage.

3. Isolation requirements

To improve the separation of charged leptons produced in the decays of W and Z bosons from those produced in the decays of heavy-flavor hadrons, electron and muon candidates are required to be isolated from other observed particle activity within the event. In particular, we require lepton candidates to satisfy both calorimeter and track isolation requirements. The sums over measured transverse energies in individual calorimeter towers and the transverse momenta of reconstructed particles whose trajectories lie within a cone of $\Delta R \equiv \sqrt{(\Delta\eta)^2 + (\Delta\phi)^2} < 0.4$ around the candidate must be less than 10% of the electron E_T or muon p_T. An exception is the case of the likelihood-based electron selection, for which the isolation variables are included as additional inputs in the construction of the likelihood function.

For the targeted $H \to W^+W^-$ decay process, the spin correlation between the two leptonically decaying W bosons tends to result in leptons with trajectories close to one another. In roughly 10% of cases, the leptons lie within each other's isolation cones, and the energy deposits and tracks associated with one lepton cause the other lepton to fail its isolation requirements. To avoid this issue and recover lost signal acceptance, isolation calculations are modified to exclude from the search cone all calorimeter tower energies and reconstructed tracks associated with other lepton candidates that meet nonisolation-related criteria.

4. Isolated tracks

Two additional lepton categories are defined for tracks that extrapolate geometrically to noninstrumented regions of the calorimeters and have no matches with track segments in the muon detectors. Such tracks, which meet quality and isolation requirements, comprise one further lepton category. Since the candidates in this category are not distinguishable as electrons or muons, either of the possibilities are allowed in each event. Electrons that pass though nonactive regions of the calorimeter may radiate bremsstrahlung photons thus failing isolation requirements because of photon energy deposition in surrounding EM towers. Such electrons are recovered into a second track-based category containing track candidates that fail the standard calorimeter isolation criteria but satisfy a modified criterion, in which EM energy depositions from towers adjacent to the track candidate are subtracted from the total measured energy within the isolation cone.

B. Lepton identification efficiency determination

Selection requirements reduce the probability for electrons and muons to be identified as lepton candidates. In order to account for a potential mismodeling of this efficiency in the simulation, the efficiency is measured from observed $Z \to \ell^+\ell^-$ decays. The events are collected using the single central electron and muon trigger paths. One of the reconstructed lepton candidates (referred to as the tag) must satisfy all cut-based selection criteria and be identified as consistent with the lepton that triggered the on-line selection of the event. The second candidate (known as the probe) is only required to pass minimal requirements, for which the expected efficiency approaches 100% and is therefore assumed to be well modeled in the simulation. The dilepton invariant mass is required to lie within ± 15 GeV$/c^2$ of the Z boson mass to ensure that the event samples contain primarily real dilepton events from $Z \to \ell^+\ell^-$ production.

Based on these samples, the measured efficiency for an additional set of test criteria applied on the probe lepton is simply the fraction of the probes that satisfy the full criteria. A small complication arises when tagged leptons also satisfy probe-lepton criteria due to overlapping selection requirements. For these cases, events in which both candidates are identified as tags need to be counted twice in the efficiency calculation. Events that do not meet the test criteria have non-negligible background contributions from W + jet and multijet production. Measured efficiencies need to be corrected to account for the presence of background within these events. The background contributions are estimated using a linear extrapolation across the Z boson signal mass range based on events counts within sideband regions on both sides of the signal range.

Separate efficiency calculations are made for each of the lepton categories. The measured efficiencies are defined as an average over those for each of the individual probe candidates from the $Z \to \ell^+\ell^-$ sample. Hence, the measured efficiencies are applied as corrections to the detector simulation, relying on its description of p_T, η, and ϕ dependence, but correcting the average efficiency to that measured directly from observed events. Measurements based on observed events deviate from those obtained in simulation by up to 6% with uncertainties of 1%–2%. The efficiencies are measured separately for several data-taking periods. Observed effects of additional $p\bar{p}$ collisions within individual beam crossings (''pileup'') are found to be well modeled in the simulation.

We validate the estimate of trigger and lepton selection efficiencies and their proper inclusion in the simulation by measuring the DY production cross section from independent, inclusive dilepton samples, each corresponding to one possible same-flavor combination of the lepton categories. In the case of $Z \to e^+e^-$, we measure cross sections from 11 independent samples constructed from two triggerable electron categories, two nontriggerable categories, and two isolated track categories. For $Z \to \mu\mu$ events we extract measurements from 35 independent samples based on five triggerable muon categories, three nontriggerable categories, and one isolated track category. The 46 independent measurements are found to agree within $\pm 5\%$, consistent with the $\pm 3\%$ uncertainties assigned to the trigger and lepton selection efficiency measurements. The cross sections measured from samples containing events with one forward electron candidate are observed to be on average about 10% smaller than those of the other samples. This effect is attributed to reduced track reconstruction efficiency in the forward region of the detector ($|\eta| > 1.2$), where COT coverage is reduced. Since track reconstruction, which is used to define probe leptons in this region, is not fully efficient, an additional correction is required. This factor is obtained directly from the extracted DY cross sections as the ratio of averaged measurements from event samples with and without forward electron candidates.

C. Tau lepton identification

Decays of tau leptons to electrons and muons (roughly 35% of total branching ratio) are identified within the lepton categories, and the additional acceptance from leptonic τ decays is included within all background and signal estimates. In the remaining 65% of cases, tau leptons undergo a hadronic decay $\tau \to X_h \nu_\tau$, where X_h can be a charged pion, kaon, or a short-lived intermediate resonance that decays to final states containing neutral or charged pions and kaons. Additional signal acceptance is obtained by identifying tau lepton candidates produced via these decay modes.

The pions and kaons produced in tau lepton decays are expected to deposit significant energy in neighboring calorimeter towers. The reconstruction of hadronically decaying tau lepton candidates is therefore based on a narrow calorimeter cluster with a maximum of three matched tracks. The sum of measured transverse energies from calorimeter towers contained within the cluster is labeled as $E^\tau_{\rm clus}$, and the matching track with the highest p_T is referred to as the tau lepton *seed track*. Signal and isolation cones are defined around the seed track direction where the opening angle of the signal cone depends on the calorimeter cluster energy, $\theta_{\rm sig} = \min(0.17, 5/E^\tau_{\rm clus}[\text{GeV}])$ radians, and the opening angle of the isolation cone is fixed at 0.52 radians. Neutral pions within the signal cone are reconstructed by combining position information from the shower-maximum detector with energy depositions measured in the EM calorimeter. Tracks and reconstructed π^0 candidates matched to the calorimeter cluster are combined to reconstruct the *visible momentum* of the tau lepton candidate. A detailed description of the techniques used for reconstructing hadronically decaying tau leptons is provided in Ref. [91].

Additional requirements are imposed to improve the purity of hadronically decaying tau lepton candidates. Candidates are required to have one track (1-prong) or three tracks (3-prong), where the absolute value of the sum of the charges of the reconstructed particles is one. The visible transverse momentum of the candidate is required to exceed 15 GeV/c or 20 GeV/c for 1-prong and 3-prong tau lepton candidates, respectively. The mass reconstructed from the visible momentum must also be consistent with the tau lepton mass. To reduce background contamination from parton jets, which are expected to produce wider energy clusters than those of hadronically decaying tau leptons, low activity in both the calorimeter and tracking systems is required in the region between the outer edges of the signal and isolation cones. Contamination from electrons is reduced by limiting the relative fractions of EM and HAD energy within the reconstructed calorimeter cluster.

D. Jet identification

Calorimeter jets are reconstructed using a fixed cone algorithm [87] with a radius of $\Delta R = \sqrt{\Delta\phi^2 + \Delta\eta^2} = 0.4$. Corrections are applied to measured jet energies to compensate for nonlinearities and nonuniformities in the response of the calorimeter, excess energy deposited within the jet cone from sources other than the assumed parent parton, and missing energy from the parent parton deposited outside the jet cone [87]. In this search we only consider jets with corrected $E_T > 15$ GeV and within the pseudorapidity region $|\eta| < 2.5$. Jets are also required to be separated ($\Delta R > 0.4$) from identified leptons.

To reduce backgrounds originating from $t\bar{t}$ production, events with exactly two oppositely charged leptons and two or more reconstructed jets are vetoed if any of the jets can be identified as likely to have originated from a bottom quark. This identification is made by reconstructing within a jet secondary track vertices consistent with the decay of longer-lived hadrons produced in the hadronization of heavy quarks [92].

E. Missing transverse energy

Neutrinos escape detection and their energies cannot be directly measured. Their presence is inferred from an imbalance of observed transverse energies within a event, $\not\!\!E_T$, which is defined as the magnitude of $-\Sigma_i E_T^i \hat{n}_i$, where $\hat{n}_i$ is the unit vector pointing from the beam line to the ith calorimeter tower in the plane perpendicular to the direction of the beams. The $\not\!\!E_T$ is corrected by subtracting the energy deposited in the calorimeter by minimum-ionizing muons and adding back their measured p_T. Energy corrections applied to calorimeter jets are also accounted for in the $\not\!\!E_T$ determination through the subtraction of raw jet energies and addition of corrected jet energies.

The primary purpose of incorporating $\not\!\!E_T$ requirements in our event selection is to significantly reduce background contributions from processes leading to final states without neutrinos. The DY process, for example, has a large production cross section and final state topologies similar to those of the Higgs boson signal that contain two charged leptons but no neutrinos. Events that originate from these types of processes and satisfy $\not\!\!E_T$ selection requirements necessarily result from detector energy mismeasurements. For this reason these backgrounds can be reduced even further in many cases via selection requirements based on a *special* missing transverse energy variable ($\not\!\!E_T^{\rm spec}$) defined as

$$\not\!\!E_T^{\rm spec} \equiv \begin{cases} \not\!\!E_T & \text{if } \Delta\phi_{\not\!\!E_T,\text{nearest}} > \frac{\pi}{2} \\ \not\!\!E_T \sin(\Delta\phi_{\not\!\!E_T,\text{nearest}}) & \text{if } \Delta\phi_{\not\!\!E_T,\text{nearest}} < \frac{\pi}{2}, \end{cases} \quad (1)$$

where $\Delta\phi_{\not\!\!E_T,\text{nearest}}$ is the angle between the $\not\!\!E_T$ and the closest lepton or jet transverse momentum vector. An undermeasurement of the lepton or jet momentum leads the $\not\!\!E_T$ to be aligned with the direction of the corresponding candidate, and for these cases the $\sin(\Delta\phi_{\not\!\!E_T,\text{nearest}})$ term significantly reduces the value of $\not\!\!E_T^{\rm spec}$ with respect to the nominal $\not\!\!E_T$.

F. Data sample selections

We define multiple independent data samples based on various kinematic selection requirements such as the number of reconstructed jets and leptons and the measured $\not\!\!E_T$ or $\not\!\!E_T^{\rm spec}$. The construction of multiple samples enhances the ability to separate potential signal and background contributions. Statistical independence of the samples allows convenient combination of results based on distinct subsamples to preserve maximum sensitivity. Additional control samples are constructed to tune or test modeling of specific background processes. Typically, these control samples are based on the kinematic selections used for defining one of the search subsamples, where one or more criteria has been modified to further enhance the dominant background contribution. Tuning parameters used to improve the agreement between data and simulation are obtained from specific control regions and incorporated, where applicable, into background modeling across all data samples used in the search.

Table II summarizes the 13 data samples used in this search as well as the 15 associated control samples. The specific kinematic criteria associated with each grouping of search samples and its associated control sample(s) are described in the following subsections.

1. Opposite-sign base selection (0 or 1 jet)

Events with exactly two opposite-sign (OS) electron or muon candidates and one or zero reconstructed jets are included in the base selection. The main background contributions to this event sample are from the DY process, where the observed $\not\!\!E_T$ originates from mismeasurements of lepton or jet energies; $W\gamma$ and W + jets, where a photon

TABLE II. Summary of names assigned to the Higgs boson search samples and their associated control samples along with the background processes targeted by each control sample.

Search sample(s)	Associated control sample(s)	Background targeted
OS base (0 jet, high s/b leptons)	SS base	W + jets
OS base (0 jet, low s/b leptons)	OS base (intermediate $\not\!\!E_T^{\rm spec}$)	DY
OS base (1 jet, high s/b leptons)		
OS base (1 jet, low s/b leptons)		
OS base (≥ 2 jets)	SS base (≥ 2 jets)	W + jets
	OS base (≥ 2 jets, intermediate $\not\!\!E_T^{\rm spec}$)	DY
	OS base (≥ 2 jets, b-tagged)	$t\bar{t}$
	SS inverse $M_{\ell\ell}$	$W\gamma$
OS inverse $M_{\ell\ell}$	OS inverse $M_{\ell\ell}$ (intermediate $\not\!\!E_T^{\rm spec}$)	DY
	OS hadronic tau ($e + \tau_{\rm had}$, high $\Delta\varphi(\vec{p}_T(\tau), \vec{p}_T(\ell))$)	W + jets
OS hadronic tau ($e + \tau_{\rm had}$)	OS hadronic tau ($e + \tau_{\rm had}$, low $\not\!\!E_T$)	Multijet
OS hadronic tau ($\mu + \tau_{\rm had}$)	OS hadronic tau ($\mu + \tau_{\rm had}$, low $\not\!\!E_T$, low $\Delta\varphi(\vec{p}_T(\ell), \vec{\not\!\!E}_T)$)	$Z/\gamma^* \rightarrow \tau\tau$
SS (≥ 1 jets)	SS (≥ 1 jets, low $\not\!\!E_T$)	DY
	SS (0 jet)	W + jets
Trilepton WH	Trilepton WH (intermediate $\not\!\!E_T$)	$Z\gamma$
Trilepton WH ($\ell + \ell + \tau_{\rm had}$)	Trilepton WH ($\ell + \ell + \tau_{\rm had}$, intermediate $\not\!\!E_T$)	Z + jets
Trilepton ZH (1 jet)	Trilepton ZH (0 jet)	WZ
Trilepton ZH (≥ 2 jets)		

or jet is misidentified as a lepton; and direct $W^+W^-\rightarrow\ell^+\nu\ell^-\bar{\nu}$ production, which has an equivalent final state as the signal. To suppress DY background, we require $\not\!\!E_T^{\rm spec} > 25$ GeV. This criterion is reduced to $\not\!\!E_T^{\rm spec} > 15$ GeV for electron-muon events, for which the DY background contribution is significantly reduced. We also require the candidates to have $M_{\ell\ell} > 16$ GeV$/c^2$ to suppress $W\gamma$ background contributions.

We separate the selected events into four further samples based on whether they contain a reconstructed jet and the qualities of the two lepton candidate types. Events with central lepton candidates are considered as having high signal-to-background (high s/b), while events with one or more forward lepton candidates are considered as having low signal-to-background (low s/b). The additional subdivision of events allows further isolation of specific background contributions. Contributions from $W\gamma$ and W + jets are more significant in the low s/b samples, while the relative mix of WW and DY contributions is significantly different for events with and without a reconstructed jet.

We construct two additional control samples based on the generic selection criteria associated with these search samples. Events containing same-sign (SS) dileptons that otherwise satisfy the signal sample criteria form the SS base control region, which is used to test W + jets background modeling. The OS base (intermediate $\not\!\!E_T^{\rm spec}$) control sample contains events with same-flavor (e^+e^- or $\mu^+\mu^-$) dileptons and $\not\!\!E_T^{\rm spec}$ between 15 and 25 GeV that otherwise satisfy search sample criteria. This control sample is used to tune the DY modeling applied to the associated search samples.

2. Opposite-sign base selection (≥ 2 jets)

Events that satisfy the criteria for the OS base selection but contain two or more reconstructed jets are classified separately. The largest background contribution to this sample is from the $t\bar{t}\rightarrow b\ell^+\nu\bar{b}\ell^-\bar{\nu}$ process. To help reduce this background, events are rejected from the search sample if any of the reconstructed jets are tagged as consistent with having originated from a bottom-quark decay by the SECVTX algorithm [92], which identifies displaced track vertices within jets. Even after application of this veto, $t\bar{t}$ production is still the single largest source of background events to this search sample.

To test background modeling, three additional control samples are defined. Same-sign dilepton events, which otherwise satisfy the signal sample criteria, form the SS base (≥ 2 jets) control sample, which is again used to test W + jets background modeling. Similarly, the DY modeling for this search sample is tested using the OS base (≥ 2 jets, intermediate $\not\!\!E_T^{\rm spec}$) control sample, which contains same-flavor dilepton events with $\not\!\!E_T^{\rm spec}$ between 15 and 25 GeV that satisfy remaining search sample criteria. Events that are rejected from the search sample exclusively due to the identification of one or more jets as being consistent with bottom-quark decays form the OS base (≥ 2 jets, b-tagged) control sample used to test $t\bar{t}$ modeling.

3. Opposite-sign inverse $M_{\ell\ell}$ selection

Events that fail the $M_{\ell\ell} > 16$ GeV$/c^2$ requirement but otherwise satisfy OS base (0 or 1 jet) selection criteria are collected into another independent search sample. The

primary source of background events in this search sample is $W\gamma$ production, where the photon is misidentified as an electron. Dilepton events originating from the decays of heavy-flavor hadrons are mostly removed by tighter $\not\!\!E_T$ requirements on events with reconstructed dilepton mass ($M_{\ell\ell}$) consistent with J/ψ and Υ meson decays. We define $\not\!\!E_T$ significance as the ratio of the measured $\not\!\!E_T$ to the scalar sum of measured transverse energies for all reconstructed jets and leptons. For events with $M_{\ell\ell} < 6$ GeV$/c^2$ and $8.5 < M_{\ell\ell} < 10.5$ GeV$/c^2$, the $\not\!\!E_T$ significance is required to be greater than 4.

Same-sign dilepton events that pass the other selection requirements of this search sample form the SS inverse $M_{\ell\ell}$ control sample, which is used to tune the $W\gamma$ background modeling. Validation of the DY modeling used in association with this search sample is based on the OS inverse $M_{\ell\ell}$ (intermediate $\not\!\!E_T^{\text{spec}}$) control sample made up of same-flavor events with $\not\!\!E_T^{\text{spec}}$ between 15 and 25 GeV that otherwise satisfy sample selection criteria.

4. Opposite-sign hadronic tau selection

While tau lepton decays to electrons and muons are incorporated within the search samples, signal acceptance is enhanced by including events containing one electron or muon candidate and one hadronically decaying tau lepton candidate in separate search samples. Because events in these samples are collected by the same trigger selections, the single electron or muon is necessarily responsible for having triggered the event and is therefore required to have $p_T > 20$ GeV$/c$.

Additional selection criteria are applied to reduce background contributions, which are significantly larger in this sample. To minimize contributions from processes with final states without neutrinos such as DY $Z/\gamma^* \to \ell\ell$ ($\ell = e$ or μ), multijet, and γ + jet production, the observed $\not\!\!E_T$ is required to exceed 20 GeV. Dilepton invariant mass, $M(\tau\ell)$, is also required to be above 20 GeV$/c^2$ to reduce backgrounds from the decays of heavy-flavor hadrons. The DY $Z/\gamma^* \to \tau\tau$ background contribution is removed by requiring a minimum angle of 1.5 radians between the dilepton transverse momentum and the missing transverse energy, $\Delta\varphi(\vec{p}_T(\ell) + \vec{p}_T(\tau), \vec{\not\!\!E}_T)$. Similarly, the dominant W + jets background contribution is suppressed by requiring a maximum angle of 1.5 radians between the transverse momenta of the two leptons, $\Delta\varphi(\vec{p}_T(\tau), \vec{p}_T(\ell))$. To take advantage of differing background compositions, events are separated into two search samples based on the presence of an electron or muon candidate.

Background modeling for these search samples is validated using three control samples. The W + jets-dominated OS hadronic tau ($e + \tau_{\text{had}}$, high $\Delta\varphi(\vec{p}_T(\tau), \vec{p}_T(\ell))$) sample is constructed by selecting events with $\Delta\varphi(\vec{p}_T(\tau), \vec{p}_T(\ell)) > 2.0$ radians that otherwise satisfy search sample criteria. The multijet-dominated OS hadronic tau ($e + \tau_{\text{had}}$, low $\not\!\!E_T$) sample is composed of events containing electron candidates, which fail the search sample criteria solely on the basis of an observed $\not\!\!E_T <$ 20 GeV. The OS hadronic tau ($\mu + \tau_{\text{had}}$, low $\not\!\!E_T$, low $\Delta\varphi(\vec{p}_T(\ell), \vec{\not\!\!E}_T)$) sample contains events with muon candidates, for which the observed $\not\!\!E_T < 20$ GeV and $\Delta\varphi(\vec{p}_T(\ell), \vec{\not\!\!E}_T) < 0.5$ radians. This control sample is used to validate DY $Z/\gamma^* \to \tau\tau$ background modeling and hadronically decaying tau lepton reconstruction efficiencies.

5. Same-sign dilepton selection

Events with exactly two same-sign electron or muon candidates form an additional search sample. Higgs boson production in association with a W or Z boson can result in a final state containing same-sign leptons when, for example, two W^+ bosons (one from the original associated production and the other from a subsequent $H \to W^+W^-$ decay) decay leptonically. The remaining W boson from the Higgs boson decay most often decays hadronically, leading to the production of jets within the event. Hence, events in this search sample are required to have at least one reconstructed jet.

An important background contribution to the same-sign event sample is DY $Z \to \ell^+\ell^-$ production, where one of the lepton charges is misreconstructed, or a bremsstrahlung photon converts into a e^+e^- pair within the detector, creating the potential for the original lepton to be reconstructed with an incorrect charge. Lepton candidates of this type are referred to as *tridents*. To help reduce DY background contamination, events containing forward electron candidates, which are affected by significant charge mismeasurement rates, are rejected. In addition, since looser likelihood criteria tend to select trident candidates, central electrons in these events are required to pass tight cut-based selection. Backgrounds from DY processes are further reduced by requiring events to have $\not\!\!E_T > 10$ GeV. The other significant sources of background events for this sample are W + jets and $W\gamma$ production, where a jet or photon is misidentified as a lepton. To reduce backgrounds from these sources, events are required to have $M_{\ell\ell} > 16$ GeV$/c^2$ and the minimum p_T criterion on the nontriggered lepton in these events is increased from 10 to 20 GeV$/c$.

Two associated control samples are formed to validate background modeling for this search sample. Events that satisfy the search sample criteria apart from containing no reconstructed jets form the SS (0 jet) sample, which is dominated by background contributions from W + jets production. The SS (≥ 1 jets, low $\not\!\!E_T$) control sample is composed of events with $\not\!\!E_T < 10$ GeV that otherwise satisfy the search sample criteria. This sample is used to test DY background modeling and the modeling for trident events.

6. Trilepton WH selection

We also incorporate separate search samples for events containing exactly three charged-lepton candidates. Such

final states are contributed by Higgs boson production in association with a $W(\rightarrow \ell\nu)$ boson and decaying as $H \rightarrow W(\rightarrow \ell\nu)W(\rightarrow \ell\nu)$. Events containing three leptons of the same charge are not consistent with the corresponding final state and are rejected. To increase signal acceptance, events with a single tau lepton candidate serving as one of the three lepton candidates are included in this search sample.

Because of differing background contributions, events are classified into two separate search samples based on whether they contain a tau lepton candidate. In addition, events containing a same-flavor, opposite-sign pair of lepton candidates with an invariant mass within ± 15 GeV$/c^2$ of the Z boson mass are removed and assigned to Trilepton ZH search samples described in the following section. The dominant backgrounds to the Trilepton WH search samples are $Z\gamma$ and Z + jets production, where the Z is produced off shell and a jet or photon is misidentified as a lepton. Because these processes lead to final states without neutrinos, we require events in these samples to have $\not\!\!E_T >$ 20 GeV.

To validate modeling of the primary backgrounds, we construct two associated control samples from events with $\not\!\!E_T$ between 10 and 20 GeV that otherwise satisfy the search sample criteria. The Trilepton WH (intermediate $\not\!\!E_T$) control sample contains events with no tau lepton candidates and is used to validate $Z\gamma$ background modeling. Events containing a tau lepton candidate form the Trilepton WH ($\ell + \ell + \tau_{\rm had}$, intermediate $\not\!\!E_T$) control sample used for testing Z + jets background modeling.

7. Trilepton ZH selection

A similar production mode for signal events with exactly three leptons is associated Higgs boson production with a Z boson and subsequent $H \rightarrow W^+W^-$ decay. A same-flavor, opposite-sign lepton pair is produced in a leptonic decay of the Z boson. A third lepton can originate from the leptonic decay of either W boson produced in the Higgs boson decay. Events containing three leptons with the same charge are inconsistent with the signal final state and rejected from the search sample. The remaining W boson from the Higgs boson decay must decay hadronically, leading to the production of jets. Hence, events in this search sample are required to have at least one reconstructed jet.

Events with exactly one and two or more jets are separated into two search samples. Determination of a transverse Higgs boson mass is possible in events containing at least two jets due to the availability of all decay products in the assumed final state (the transverse energy of the single neutrino is inferred from the $\not\!\!E_T$). The statistical independence of these search samples with respect to the Trilepton WH samples is maintained by selecting only the events that contain a same-flavor, opposite-sign lepton pair within ± 15 GeV$/c^2$ of the Z boson mass. Because of large background contributions from on-shell Z + jets production, events containing tau lepton candidates are not included within the Trilepton ZH search samples. Events in these samples are also required to have observed $\not\!\!E_T > 10$ GeV to further reduce $Z\gamma$ and Z + jets background contributions.

A single associated control sample is formed to test the background modeling used for these search samples. The Trilepton ZH (0 jet) control sample consists of events with no reconstructed jets that otherwise satisfy search sample criteria. Contributions from WZ production are the single largest source of events to this control sample.

VI. BACKGROUND MODELING

We exploit differences between the kinematic features of signal and background events to enhance search sensitivity. Hence, accurate modeling of all contributing processes is essential. We model contributions from all signal and most background processes using Monte Carlo event generators interfaced to a GEANT-based simulation of the CDF II detector [93]. Events that contain a falsely identified (*fake*) lepton candidate produced within the shower of a parton jet are more difficult to model using simulation. Therefore, data-driven methods are generally employed for modeling these backgrounds.

Many of the relevant signal and background processes are modeled with PYTHIA [94], which is a leading order (LO) event generator that incorporates higher-order corrections through parton-shower algorithms. Events are generated with PYTHIA version 6.216 using the CTEQ5L [95,96] PDFs and the set of input parameters that best match underlying event distributions in CDF data [97]. For background processes more sensitive to higher-order contributions, NLO generators are used and interfaced with PYTHIA to model the showering and fragmentation of generated initial and final state particles. We incorporate simulated event samples generated with both MC@NLO [98] and MADGRAPH [99]. Because NLO event generators include first-order radiative effects, the scale of radiative corrections applied in subsequent PYTHIA shower modeling is cut off at the lower bound of that applied within the original event generation. In other cases, contributions from orders above NLO play an important role and ALPGEN [100] interfaced with PYTHIA is used for generating samples. Here, independent samples for the LO process plus $n = 0$, 1, 2, and 3 or more additional partons are generated, and a matching algorithm is used to remove overlapping contributions. These contributions originate from, for example, an ALPGEN LO plus 0 parton event which gains an additional hard radiation through the PYTHIA showering and becomes a LO plus 1 parton event. Modeling of the $W\gamma$ and $Z\gamma$ production processes is generally achieved with a dedicated LO generator [101] interfaced with PYTHIA to incorporate initial state radiative effects. Normalizations of predicted event rates are based

on theoretical cross section calculations performed at the highest available order.

Nonresonant WW production in conjunction with subsequent leptonic decays of both W bosons results in a final state similar to that of the primary signal. Because of the relevance of WW backgrounds, NLO generators are generally used to model them. In particular, MC@NLO is used to simulate events originating from WW production in the OS base (0 jet and 1 jet), OS inverse $M_{\ell\ell}$, and SS (≥ 1 jets) search samples. The MC@NLO generator does not simulate the small but potentially signal-like contributions to WW production originating from gluon fusion [102]. To account for this contribution, events are reweighted as a function of the angular separation in the transverse plane between the two generator-level leptons, $\Delta\phi_{\ell\ell}$, to incorporate the extra contribution predicted in Ref. [102]. Uncertainties on the correction are obtained from alternate reweightings that correspond to halving or doubling the predicted contribution of the unmodeled production modes. In the OS base (≥ 2 jets) search sample, the presence of multiple reconstructed jets requires inclusion of NNLO contributions in the WW background model. Therefore, events generated with ALPGEN are used for modeling the WW contribution. For the OS hadronic tau ($e + \tau_{\text{had}}$ and $\mu + \tau_{\text{had}}$) search samples, WW background contributions have a reduced significance with respect to those from other sources and are therefore modeled using PYTHIA. Because events originating from direct WW production share the same final states with potential signal events, it is not possible to define independent WW background-rich data control regions for testing the modeling. Instead, the primary validation of this modeling comes from using it to extract a measurement of the WW production cross section directly from the search samples (see Sec. X).

Backgrounds from WZ and ZZ production in the dilepton sample are significantly smaller than those from WW production. In addition, when two leptons are produced in the decay of one Z boson, the most probable hadronic decay of the extra Z or W boson leads to events containing multiple jets at LO. We therefore mostly rely on events generated with PYTHIA to model event contributions from these processes. The PYTHIA WZ and ZZ event samples include γ^* contributions based on lower m_{Z/γ^*} thresholds of 2 and 15 GeV/c^2, respectively. Event contributions from WZ and ZZ production to the trilepton search samples are more significant and higher-order contributions are more relevant in the modeling of events containing multiple jets. Hence, independent ALPGEN WZ and ZZ event samples are used for modeling event contributions from these processes in the Trilepton ZH (≥ 2 jets) search sample. The PYTHIA WZ background model is tested in the Trilepton ZH (0 jet) control sample. An example of the agreement between observed and predicted kinematic distributions for this control sample is shown in Fig. 1(a). The background model is further validated by determining the WZ production cross section directly from the Trilepton WH search sample (see Sec. X). The modeling of ZZ background contributions is similarly tested by measuring the ZZ cross section in $ZZ \to \ell\ell\nu\nu$ within the OS base search samples (see Sec. X).

Samples produced using the Baur LO event generator [101] are used in most cases for modeling $W\gamma$ and $Z\gamma$ contributions to the search samples. Generated events are required to have a minimum angular separation of 0.2 radians between the photon and charged lepton(s) produced in the boson decay. The photon is also required to have a minimum p_T of at least 4 GeV/c. Modeling of the $W\gamma$ background is tested using the SS inverse $M_{\ell\ell}$ control sample, for which the $W\gamma$ event contribution is expected to be greater than 75%. In this sample we observe a deficit of data events relative to the model prediction and therefore assign a scale factor of 0.71 to the overall normalization of the $W\gamma$ model. The main driver of this scale factor is uncertainties associated with the detector material model in the simulation since the production of a dilepton final state via the $W\gamma$ process requires a photon conversion into a pair of electrons within the detector material. An example of the agreement between observed and predicted kinematic distributions in this sample (for the Baur model after scaling) is shown in Fig. 1(b). The $W\gamma$ background contributions are of particular importance in the OS inverse $M_{\ell\ell}$ search sample. For this sample only, MADGRAPH is used to model $W\gamma$ background contributions. The minimum threshold on the angular separation between the photon and charged lepton(s) is reduced to 0.1 radians, which expands the search reach in the low $M_{\ell\ell}$ region. The MADGRAPH model is also validated with the SS inverse $M_{\ell\ell}$ control sample. In this case, the normalization of the model agrees with data, and no scaling is needed. An example of the agreement between observed and predicted kinematic distributions for this control sample (for the MADGRAPH model) is shown in Fig. 1(c). Validation of the Baur modeling of the $Z\gamma$ process is obtained from the Trilepton WH (intermediate $\not\!\!E_T$) control sample, and an example of the agreement between observed and predicted kinematic distributions for this control sample is shown in Fig. 1(d).

Dilepton events originate from the process $t\bar{t} \to W^+bW^-\bar{b} \to \ell^+\nu b\ell^-\bar{\nu}\,\bar{b}$. The presence of two bottom quarks in the final state implies LO contributions to all search samples including those that contain events with multiple reconstructed jets. Event samples obtained from PYTHIA are therefore used for modeling $t\bar{t}$ background contributions across all search samples. Events containing jets tagged as b-quark candidates are removed from the OS base (≥ 2 jets) search sample. For the special case of modeling the $t\bar{t}$ background contribution within this sample, a standard CDF scale factor [76] (1.04 ± 0.05) that corrects Monte Carlo b-tagging inefficiency to match that observed in data is applied. A second scale factor (1.02 ± 0.02) is used to account for the small fraction of events in

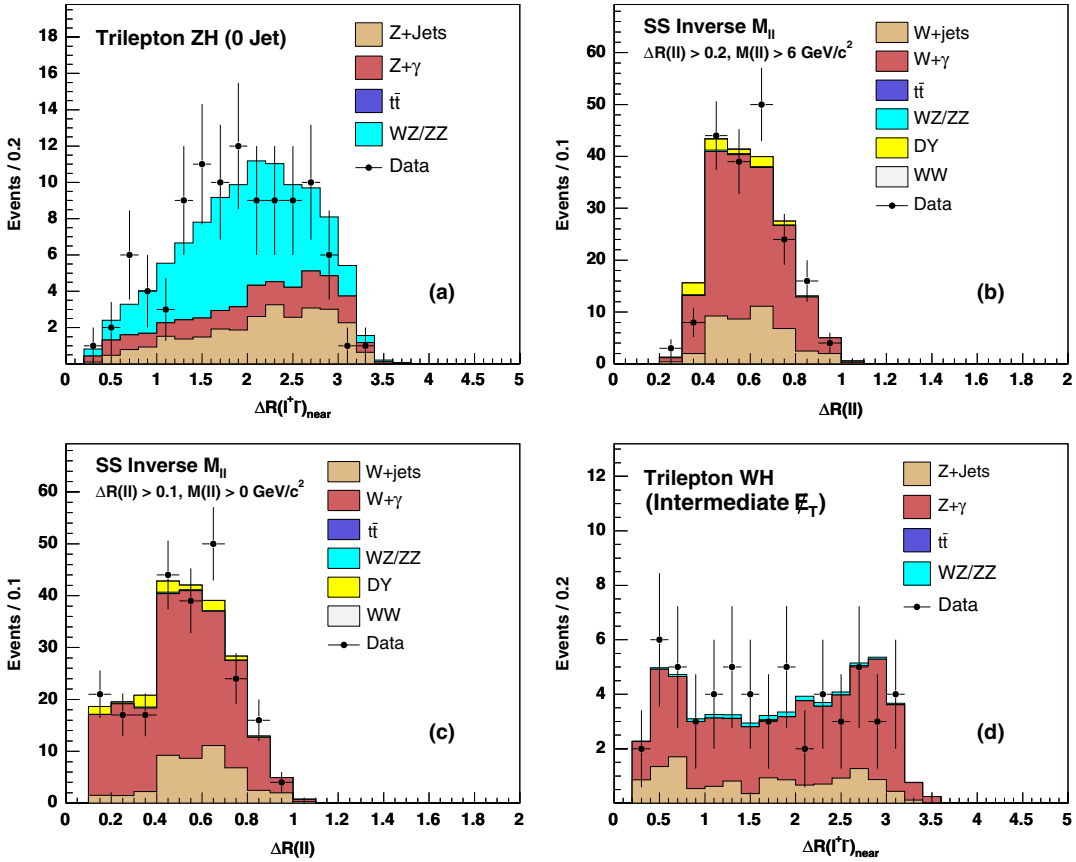

FIG. 1 (color online). Comparisons of observed and predicted kinematic distributions from independent data control samples used for validating the modeling of individual background processes contributing to search samples. (a) Dilepton angular separation, $\Delta R(\ell^+\ell^-)_{\text{near}}$, from Trilepton ZH (0 jet) control sample testing PYTHIA WZ event model. (b) $\Delta R(\ell\ell)$ from SS inverse $M_{\ell\ell}$ control sample testing the Baur $W\gamma$ event model. (c) $\Delta R(\ell\ell)$ from SS inverse $M_{\ell\ell}$ control sample testing MADGRAPH $W\gamma$ event model. (d) $\Delta R(\ell^+\ell^-)_{\text{near}}$ from Trilepton WH (intermediate $M_{\ell\ell}$) control sample testing the Baur $Z\gamma$ event model. The procedures used to determine the overall normalizations of modeled background event yields for each of the contributing processes are described in Sec. VI.

data in which silicon-tracker information required for tagging b-quark jets is missing. The OS base (≥ 2 jets, b-tagged) control sample, which is expected to have a $t\bar{t}$ contribution greater than 95%, is used to validate the modeling. Since events in this control sample are required to have at least one b-tagged jet, a reciprocal set of scale factors are applied to the modeled $t\bar{t}$ contribution. An example of the agreement between observed and predicted kinematic distributions for this control sample is shown in Fig. 2(a).

Modeling of background contributions in the search samples associated with DY (Z/γ^*) production is particularly complicated. Inclusive production is generally very well modeled with PYTHIA. However, because of minimum missing transverse energy requirements, the search samples contain DY background contributions originating from only a small subset of this inclusive production. In particular, since dilepton events originating from DY production do not involve neutrinos, missing transverse energy is necessarily generated from the mismeasurement of lepton and jet energies. For the OS base (0 jet and 1 jet) search samples, DY modeling is based on PYTHIA-generated event samples. The OS base (intermediate $\not\!\!E_T^{\text{spec}}$) control sample is used to validate and tune these samples. Initially, we observe poor modeling of the observed maximum measured missing transverse energies associated with specific values of Z/γ^* transverse momenta. In addition to mismeasurements of particles that recoil against the Z/γ^* in the hard interaction, soft scattering processes that are not necessarily well modeled in the simulation can be mismeasured, thus producing events with larger missing transverse energies than expected from simulation.

To mimic these unmodeled effects, a constant offset is added to the missing transverse energy within each simulated event. The value of this offset is such that the best match is achieved in the relevant kinematic distributions between data and simulation within the OS base (intermediate $\not\!\!E_T^{\text{spec}}$) control sample. The resulting offset is $+4 \pm 2$ GeV. The tuned simulated events are reweighted to reproduce observed event counts correctly in the OS base (intermediate $\not\!\!E_T^{\text{spec}}$) control sample. Independent reweightings are obtained for simulated events within the

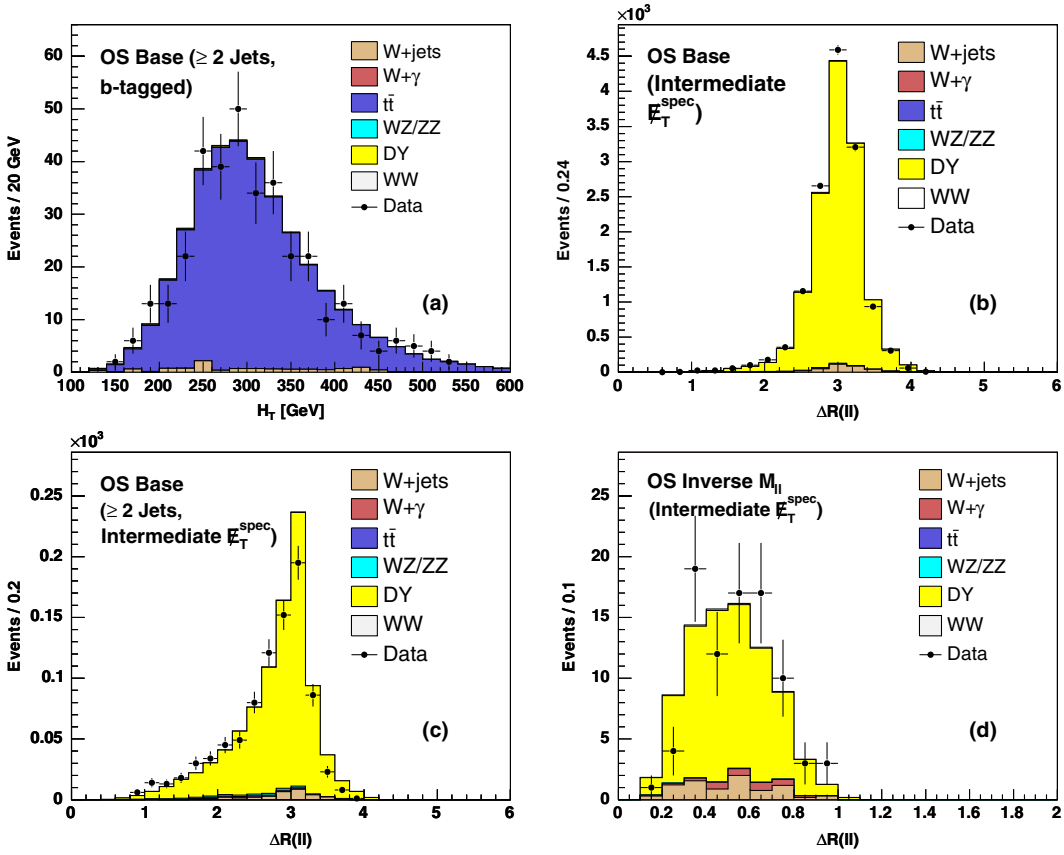

FIG. 2 (color online). Comparisons of observed and predicted kinematic distributions from independent data control samples used for validating the modeling of individual background processes contributing to search samples. (a) Sum of measured lepton and jet transverse energies and missing transverse energy, H_T, from OS base (≥ 2 jets, b-tagged) control sample testing PYTHIA $t\bar{t}$ event model. (b) $\Delta R(\ell\ell)$ from OS base (intermediate $\not\!\!E_T^{\rm spec}$) control sample testing tuned PYTHIA DY event model. (c) $\Delta R(\ell\ell)$ from OS base (≥ 2 jets, intermediate $\not\!\!E_T^{\rm spec}$) control sample testing ALPGEN DY event model. (d) $\Delta R(\ell\ell)$ from OS inverse $M_{\ell\ell}$ (intermediate $\not\!\!E_T^{\rm spec}$) control sample testing MADGRAPH DY event model. The procedures used to determine the overall normalizations of modeled background event yields for each of the contributing processes are described in Sec. VI.

dilepton invariant mass ranges of 16–36, 36–56, 56–76, 76–106, and greater than 106 GeV$/c^2$. An example of the agreement between observed and predicted kinematic distributions for the control sample after applying this tuning procedure is shown in Fig. 2(b).

In the OS base (≥ 2 jets) search sample, DY contributions from NNLO are significant and ALPGEN-generated events are used for modeling the background. A similarly defined OS base (≥ 2 jets, intermediate $\not\!\!E_T^{\rm spec}$) data control region is used to validate the ALPGEN event modeling. Owing to the presence of two high-E_T jets within each event, effects from unmodeled energies associated with soft scattering processes are reduced, and the untuned event model is found to be sufficient. An example of the agreement between observed and predicted kinematic distributions for this control sample is shown in Fig. 2(c).

A unique set of production processes is associated with DY contributions to the OS inverse $M_{\ell\ell}$ search sample. In this sample, events originate primarily from simple $2 \rightarrow 2$ scattering processes, in which the Z/γ^* is radiated from a final state quark. This mechanism allows for the production of events with low mass Z/γ^* bosons of sufficient p_T such that significant missing transverse energy can result from the mismeasurement of associated recoil particle energies. Since this process is not modeled by PYTHIA, MADGRAPH is used to model DY contributions in this sample. This modeling is validated using the OS inverse $M_{\ell\ell}$ (intermediate $\not\!\!E_T^{\rm spec}$) control sample. The lack of e-μ dilepton events within this sample indicates that cascade decays of bottom quarks are not an appreciable background. Dileptons from charmonium and bottomonium decays can be observed within this control sample but are vetoed as described in Sec. V. An example of the agreement between observed and predicted kinematic distributions for this control sample is shown in Fig. 2(d).

Finally, DY background contributions to the SS (≥ 1 jets) search sample come primarily from $Z \rightarrow e^+e^-$ production, in which a photon radiated from one of the electrons subsequently converts into an additional e^+e^- pair within the detector material. Resulting trident electron candidates with two neighboring charged particles often have misreconstructed charges due to issues associated with the

sharing of hits between tracks. Since background contributions from tridents can be significant in this search sample, electron candidates in these events are required to satisfy tight selection criteria. With this requirement, trident event contributions are substantially reduced and PYTHIA-generated samples are found to provide a good model for the remaining background. The model is validated with the SS (≥ 1 jets, low $\not\!\!E_T$) control sample, and an example of the agreement between observed and predicted kinematic distributions for this sample is shown in Fig. 3(a).

Background contributions from DY $Z/\gamma^* \rightarrow \tau^+\tau^-$ decays represent another special case. This process results in non-negligible event contributions to both OS hadronic tau search samples and the e-μ components of other dilepton search samples. The neutrinos produced in subsequent decays of the τ leptons into electrons and muons introduce missing transverse energy in these events, increasing their probability to be accepted in the search samples even without significant energy mismeasurements. We use PYTHIA interfaced with TAUOLA [103] to model this process and validate the modeling using the OS hadronic tau ($\mu + \tau_{\rm had}$, low $\not\!\!E_T$, low $\Delta\phi(\vec{p}_T(\ell), \vec{\not\!\!E}_T)$) control sample. Figure 3(b) shows an example of the agreement between observed and predicted kinematic distributions for this sample. The overall agreement within this control region is also used for assigning uncertainties on the efficiency for reconstructing and identifying hadronically decaying tau lepton candidates, which is obtained directly from simulation.

Dilepton background contributions from events containing one real lepton and a jet misidentified as a lepton originate from a high-production cross section process, W bosons produced in association with additional partons, in combination with low-probability and hard-to-simulate detector-level effects that allow a jet to be reconstructed as a lepton. Similarly, trilepton background contributions from events with two real leptons and a third jet misidentified as a lepton originate from Z boson production in association with jets. Because of the difficulties associated with simulating these processes, we rely

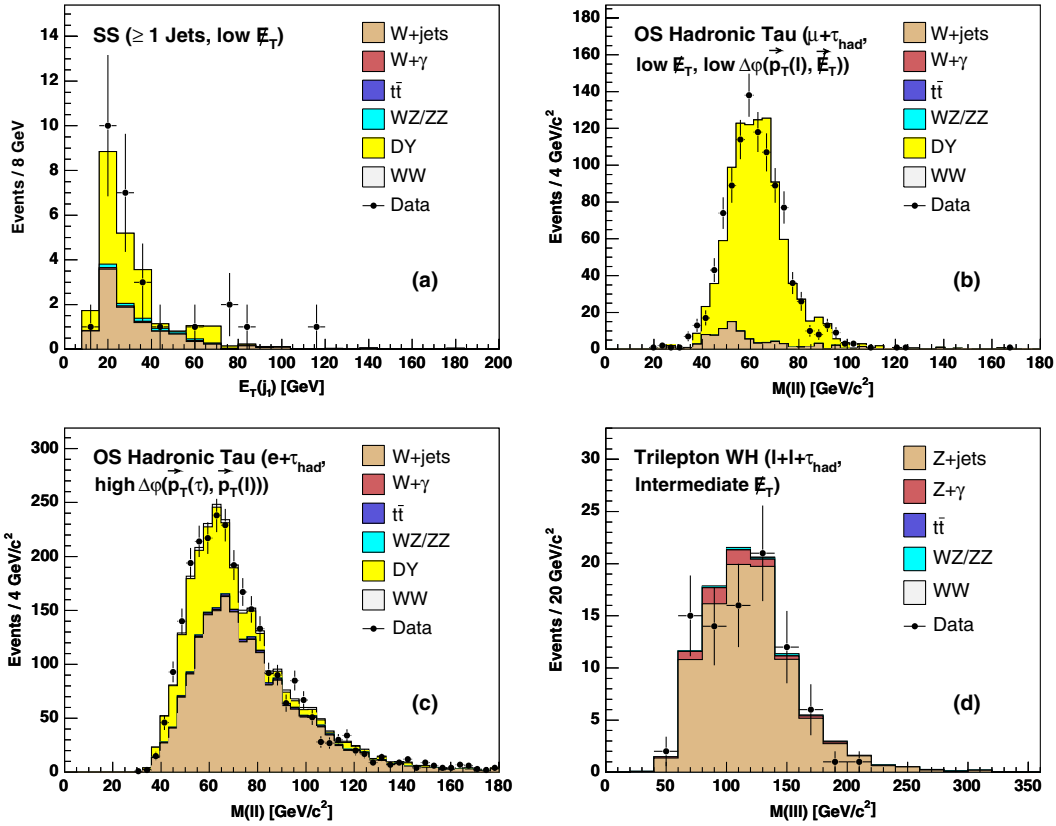

FIG. 3 (color online). Comparisons of observed and predicted kinematic distributions from independent data control samples used for validating the modeling of individual background production processes contributing to the search samples. (a) Transverse energy of leading jet, $E_T(j_1)$, from SS (≥ 1 jets, low $\not\!\!E_T$) control sample testing PYTHIA DY event model for tridents. (b) Invariant mass of muon and tau lepton pair, $M_{\mu,\tau}$ from OS hadronic tau ($\mu + \tau_{\rm had}$, low $\not\!\!E_T$, low $\Delta\phi(\vec{p}_T(\ell), \vec{\not\!\!E}_T)$) control sample testing PYTHIA DY $Z/\gamma^* \rightarrow \tau^+\tau^-$ event model. (c) Invariant mass of electron and tau lepton pair, $M_{e,\tau}$ from OS hadronic tau ($e + \tau_{\rm had}$, high $\Delta\phi(\vec{p}_T(e), \vec{p}_T(\tau))$) control sample testing ALPGEN $W +$ jets event model. (d) Trilepton invariant mass, $M_{\ell\ell\tau_{\rm had}}$, from Trilepton WH ($\ell + \ell + \tau_{\rm had}$, intermediate $\not\!\!E_T$) control sample testing ALPGEN $Z +$ jets event model. The procedures used to determine the overall normalizations of modeled background event yields for each of the contributing processes are described in Sec. VI.

mostly on data-driven background modeling. However, the probability for a jet to mimic the signature of a hadronically decaying tau lepton candidate is significantly larger than that of an electron or muon candidate. We therefore rely on ALPGEN-generated events for modeling W + jets contributions in the OS hadronic tau search samples and the Z + jets contribution in the Trilepton WH ($\ell + \ell + \tau_{\rm had}$) sample. We rely on the OS hadronic tau ($e + \tau_{\rm had}$, high $\Delta\phi(\vec{p}_T(\tau), \vec{p}_T(\ell))$) and Trilepton WH ($\ell + \ell + \tau_{\rm had}$, intermediate $\not\!\!E_T$) control samples, respectively, for validating the two ALPGEN background models. Examples of the agreement between observed and predicted kinematic distributions for the two samples are shown in Figs. 3(c) and 3(d).

For the remaining search samples, in which a parton jet is misidentified as an electron or muon candidate, a data-driven technique is used for modeling contributions from W + jets and Z + jets production. The technique relies on parametrization of the probability for a jet to be misidentified as a lepton. This parametrization is obtained from data using events collected by single-jet triggers with varying energy thresholds. For each electron and muon category used in the searches, an associated *fakeable*-lepton candidate is defined based on relaxed identification requirements. To avoid trigger biases, we ignore the highest E_T jet reconstructed within each single-jet triggered event. The total number of remaining jets that satisfy the fakeable-lepton selection criteria forms the denominator of the jet *fake rate* for the associated lepton type. The number of these jets that additionally satisfy the full charged-lepton identification selection forms the fake rate numerator, which is corrected for the expected contribution of real high-p_T leptons in these samples from simulated W and Z boson events. Fake rates are parametrized as a function of lepton p_T and are typically of the order of a few percent. Modeling of dilepton W + jets background contributions is obtained by applying the measured fake rates as weights to events collected using standard high-p_T single-lepton

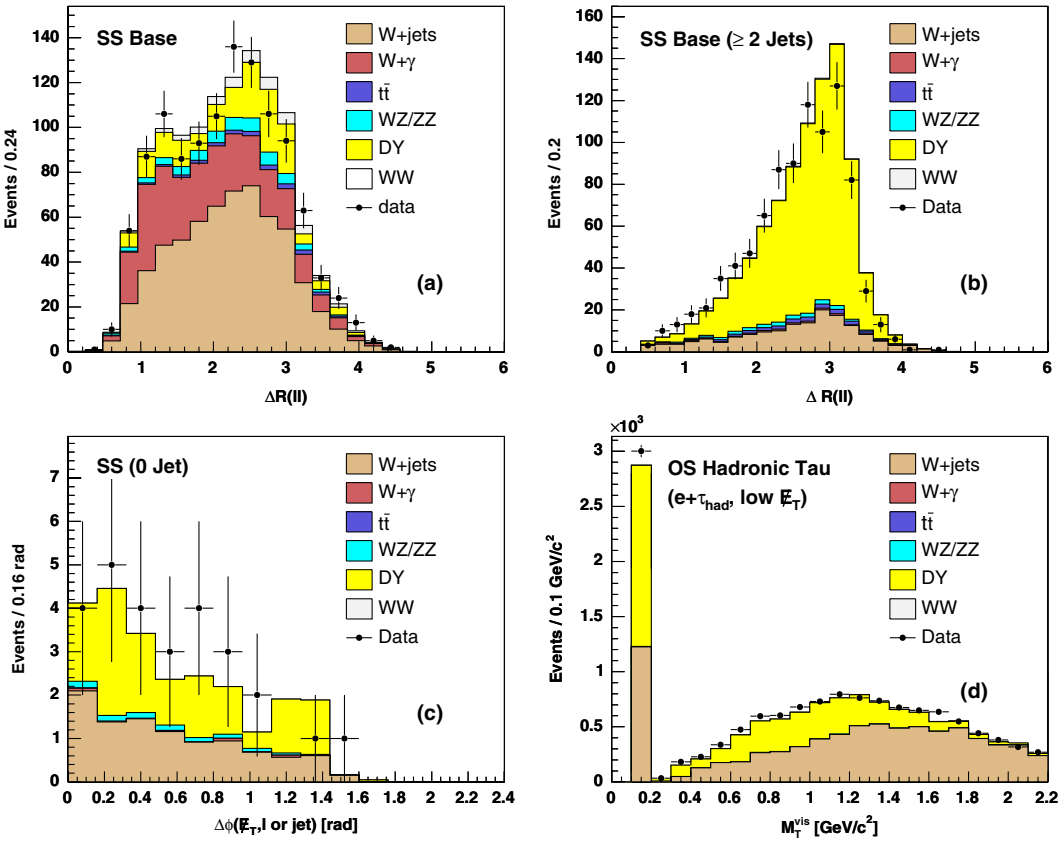

FIG. 4 (color online). Comparisons of observed and predicted kinematic distributions from independent data control samples used for validating the modeling of individual background production processes contributing to the search samples. (a) $\Delta R(\ell\ell)$ from SS base control sample testing data-driven W + jets event model. (b) $\Delta R(\ell\ell)$ from SS base (≥ 2 jets) control sample testing data-driven W + jets event model. (c) Azimuthal opening angle between missing transverse energy and nearest lepton or jet, $\Delta\phi$ ($\not\!\!E_T$, ℓ or jet), from SS (0 jet) control sample testing data-driven W + jets event model. (d) Visible transverse mass of hadronically decaying tau lepton candidate, $M_T^{\rm vis}$, from OS hadronic tau ($e + \tau_{\rm had}$, low $\not\!\!E_T$) control sample testing data-driven multijet event model. The procedures used to determine the overall normalizations of modeled background event yields for each of the contributing processes are described in Sec. VI.

triggers that are found to contain exactly one fully selected lepton candidate and one or more fakeable-lepton candidates. Similarly, modeling of trilepton Z + jets background contributions is obtained from a sample of events with exactly two fully selected lepton candidates and one or more fakeable candidates. A correction is applied to the weights of individual events for which the fakeable candidate is associated with a lepton category that cannot be responsible for triggering collection of the event. This correction accounts for the missing contribution of events containing leptons from the same categories, in which the triggered lepton is the fake lepton.

Several control samples are used to validate the data-driven background modeling for W + jets production. We use the SS base and SS base (≥ 2 jets) control samples to validate W + jets modeling in the OS base search samples. Examples of the agreement between observed and predicted kinematic distributions for the two samples are shown in Figs. 4(a) and 4(b). Although we use the same data-driven technique to model W + jets backgrounds in the SS (≥ 1 jets) search sample, several of the looser lepton categories, which are a dominant source of fake backgrounds in the OS base search samples, are not used for selecting events. Therefore, we independently validate W + jets modeling for this sample using the SS (0 jet) control sample. An example of the agreement between observed and predicted kinematic distributions for this sample is shown in Fig. 4(c).

Finally, background contributions from dijet and photon-jet production to the OS hadronic tau search samples are also modeled directly from data. Events containing an electron or muon candidate and a hadronically decaying tau lepton candidate with the same charge that otherwise satisfy search sample criteria are used to model these background sources, which contribute events containing two fake leptons. Electroweak contributions to the same-sign sample are subtracted based on estimates obtained from simulated event samples. This background model is tested using the OS hadronic tau ($e + \tau_{\rm had}$, low $\not\!\!E_T$) control sample. An example of the agreement between observed and predicted kinematic distributions for this sample is shown in Fig. 4(d).

VII. MULTIVARIATE TECHNIQUES

Three multivariate techniques are used to obtain the best possible separation of event contributions from a potential signal from those originating from background processes. These are the matrix-element method, artificial neural networks, and boosted decision trees. One or a combination of these techniques is applied to the analysis of each search sample.

A. Matrix-element method

The matrix-element (ME) method uses an event-by-event calculation of the probability density for each contributing process to produce the observed event. This method is based on simulation of the relevant processes and has been applied to a number of other measurements [104–114]. If all details of the collision properties and the detector response are modeled in the ME calculation, this method provides the optimal sensitivity to the signal. However, there are several approximations used in the calculations: theoretical differential cross sections are implemented only at leading order, a simple parametrization of the detector response is used, and for some small (WZ and $t\bar{t}$) or difficult-to-model (DY) backgrounds, a probability density is not calculated.

The event probability density for a given process is calculated as

$$P(\vec{x}_{\rm obs}) = \frac{1}{\langle\sigma\rangle}\int \frac{d\sigma_{\rm LO}(\vec{y})}{d\vec{y}}\,\epsilon(\vec{y})G(\vec{x}_{\rm obs},\vec{y})d\vec{y}, \qquad (2)$$

where the elements of $\vec{y}$ ($\vec{x}_{\rm obs}$) are the true (observed) values of the lepton momenta and $\not\!\!E_T$, $d\sigma_{\rm LO}/d\vec{y}$ is the parton-level differential cross section from MCFM V3.4.5 [115], $\epsilon(\vec{y})$ is a parametrization of the detector acceptance and selection efficiencies, and $G(\vec{x}_{\rm obs},\vec{y})$ is the transfer function representing the detector resolution and a PYTHIA-based estimate of transverse momentum of the $\ell\ell\not\!\!E_T$ system due to the initial state radiation. The constant $\langle\sigma\rangle$ normalizes the total event probability to unity. This calculation integrates the theoretical differential cross section over the missing information due to two unobserved neutrinos in the final state. We form a likelihood ratio (LR) discriminant, which is the signal probability density divided by the sum of signal and background probability densities,

$$LR_{ggH}(\vec{x}_{\rm obs}) \equiv \frac{P_H(\vec{x}_{\rm obs})}{P_H(\vec{x}_{\rm obs}) + \sum_i k_i P_i(\vec{x}_{\rm obs})}, \qquad (3)$$

where k_i are the expected fractions of WW, ZZ, $W\gamma$, and W + jets background events. An analogous likelihood ratio, LR_{WW}, is similarly formed by treating direct WW production as the signal. The ME method is used in conjunction with an artificial neural network and only in the OS base (0 jet) search samples as defined in Sec. V.

B. Neural networks

Artificial neural networks [116] are used to discriminate potential signal events from background events. A three-layer feed-forward network is constructed with N_I input nodes in the first layer, $N_I + 1$ nodes in the second layer, and one output node in the third and final layer for each search sample relying on this approach. The single output parameter of the network, referred to as the discriminant, is used to enhance the separation between signal and background. The number of variables being considered, N_I, varies depending on the search sample. Events in the simulated or data-driven background samples are weighted such that the sum of the weights is equal to the number of generated and simulated signal events. Only input

variables with accurately modeled distributions are used. A separate neural network is trained for each Higgs boson mass considered. Variables, which when included as inputs have a negligible impact on overall search sensitivity, are determined for each value of m_H and removed, resulting in differing sets of network inputs for each value of m_H. The selection of kinematic input variables for the neural network is based on kinematic properties of the production and decay of the Higgs boson. Correlated variables are discarded, resulting in the minimal set of discriminant variables. For the OS base (0 jet) search samples, matrix-element likelihood ratios were included as inputs to the neural network and resulted in only 5% improvements in overall search sensitivity, demonstrating that the neural network is able to determine the input variables needed to describe the full kinematic properties of the events and efficiently separate signal and background. Comparable results are obtained using an alternative neural network algorithm [117].

C. Boosted decision trees

To discriminate signal from backgrounds in the OS hadronic tau and Trilepton WH ($\ell + \ell + \tau_{\mathrm{had}}$) search samples, a boosted decision tree (BDT) algorithm [117,118] is used. The use of BDTs for these samples provides a simple mechanism for incorporating hadronically decaying tau lepton identification variables, which have a significant role in separating potential signal from dominant W + jets background contributions. A set of criteria is applied sequentially to the variables provided as input to the tree. A boosting procedure is applied to enhance the separation performance and make the decision robust against statistical fluctuations in the training samples. New trees are derived from the same training sample by reweighting the events that are misclassified. In this way, each tree is extended to a forest of trees and the final decision is based on a weighted majority vote of all trees within the forest [119].

VIII. ANALYSIS OUTCOMES

Higgs boson search results from the 13 search samples defined in Sec. V using the multivariate techniques described in Sec. VII are presented here. Kinematic event variables used as inputs to the multivariate algorithms are chosen to achieve the best possible separation of potential signal within each search sample from background contributions. Relative contributions of different signal and background production processes vary significantly across samples. Therefore, the multivariate outputs used to classify events within each search sample are based on unique sets of input variables, designed to take advantage of the distinct kinematic properties of potential signal and background events within each sample. Each multivariate output is trained to distinguish

TABLE III. Summary of predicted and observed event yields for seven dilepton search samples formed from electron and muon candidates. Expected signal yields are shown for potential SM Higgs boson masses of 125 and 165 GeV/c^2. The procedures used to determine the overall normalizations of modeled background event yields for each of the contributing processes are described in Sec. VI.

Process	OS base (0 jet, high s/b leptons)	OS base (0 jet, low s/b leptons)	OS base (1 jet, high s/b leptons)	OS base (1 jet, low s/b leptons)	OS base (≥ 2 jets)	OS inverse $M_{\ell\ell}$	SS (≥ 1 jets)
$t\bar{t}$	2.93 ± 0.93	0.99 ± 0.26	75 ± 15	24.5 ± 4.6	287 ± 42	1.82 ± 0.35	0.58 ± 0.08
DY	230 ± 63	230 ± 63	239 ± 55	176 ± 41	155 ± 66	23.9 ± 4.9	16.4 ± 4.6
WW	661 ± 66	308 ± 31	183 ± 22	78.0 ± 9.6	53 ± 12	37.5 ± 3.6	0.07 ± 0.02
WZ	29.1 ± 4.4	15.5 ± 2.4	26.4 ± 3.6	16.1 ± 2.2	11.7 ± 2.2	0.96 ± 0.13	14.6 ± 2.0
ZZ	42.1 ± 6.0	21.4 ± 3.0	11.5 ± 1.7	5.71 ± 0.82	5.3 ± 1.0	0.29 ± 0.04	2.43 ± 0.33
W + jets	137 ± 33	443 ± 67	54 ± 15	163 ± 26	80 ± 15	56.3 ± 7.8	45 ± 17
$W\gamma$	68.3 ± 8.6	181 ± 23	9.9 ± 1.5	31.6 ± 4.9	7.7 ± 1.9	171 ± 14	5.59 ± 0.85
Total background	1170 ± 120	1200 ± 110	599 ± 78	495 ± 56	600 ± 98	291 ± 19	85 ± 18
			$M_H = 125$ GeV/c^2				
ggH	6.9 ± 2.1	2.4 ± 0.7	2.8 ± 1.2	0.91 ± 0.39	1.07 ± 0.53	1.81 ± 0.30	-
WH	0.41 ± 0.07	0.16 ± 0.03	0.87 ± 0.14	0.30 ± 0.05	1.59 ± 0.22	0.10 ± 0.02	1.25 ± 0.17
ZH	0.25 ± 0.04	0.08 ± 0.01	0.27 ± 0.04	0.10 ± 0.02	0.76 ± 0.10	0.06 ± 0.01	0.18 ± 0.02
VBF	0.04 ± 0.01	0.013 ± 0.003	0.23 ± 0.04	0.07 ± 0.01	0.55 ± 0.09	0.05 ± 0.01	-
Total signal	7.6 ± 2.1	2.6 ± 0.7	4.2 ± 1.2	1.4 ± 0.4	3.98 ± 0.71	2.02 ± 0.30	1.43 ± 0.17
			$M_H = 165$ GeV/c^2				
ggH	21.6 ± 6.4	7.3 ± 2.2	10.9 ± 4.6	3.5 ± 1.5	5.0 ± 2.5	4.02 ± 0.66	-
WH	0.53 ± 0.09	0.19 ± 0.03	1.47 ± 0.23	0.47 ± 0.08	4.35 ± 0.61	0.14 ± 0.02	2.69 ± 0.36
ZH	0.55 ± 0.08	0.15 ± 0.02	0.57 ± 0.09	0.18 ± 0.03	2.16 ± 0.29	0.11 ± 0.02	0.39 ± 0.05
VBF	0.19 ± 0.04	0.06 ± 0.01	1.05 ± 0.18	0.30 ± 0.05	2.51 ± 0.41	0.15 ± 0.03	-
Total signal	22.9 ± 6.5	7.7 ± 2.2	14.0 ± 4.7	4.4 ± 1.5	14.0 ± 2.9	4.41 ± 0.68	3.08 ± 0.41
Data	1136	1402	545	488	596	319	87

potential signal from backgrounds based on the modeling described in Sec. VI.

A. Dilepton search samples

The numbers of expected events from each contributing signal and background process are compared in Table III with the total number of observed events in each of the seven dilepton search samples formed from electron and muon candidates. Background and signal predictions, which are shown for potential Higgs boson masses of 125 and 165 GeV$/c^2$, are taken from the models described in Sec. VI.

A summary of the kinematic variables used as inputs to the multivariate algorithms for separating potential signal from background contributions in these seven search samples is shown in Table IV. Important input variables for the diboson search samples include the charged-lepton transverse momenta, the angular separation of the lepton

TABLE IV. Summary of kinematic variables used as inputs to the multivariate algorithms for separating signal and background contributions in the dilepton search samples.

Variable	Definition	OS base (0 jet)	OS base (1 jet)	OS base (≥ 2 jets)	OS inverse $M_{\ell\ell}$	SS (≥ 1 jets)	OS hadronic tau
$E(\ell_1)$	Energy of the leading lepton		√		√		
$E(\ell_2)$	Energy of the subleading lepton				√		
$p_T(\ell_1)$	Transverse momentum of the leading lepton	√	√	√	√	√	√
$p_T(\ell_2)$	Transverse momentum of the subleading lepton	√	√	√	√	√	√
$\Delta\phi(\ell\ell)$	Azimuthal angle between the leptons	√		√	√		√
$\Delta\eta(\ell\ell)$	Difference in pseudorapidities of the leptons						√
$\Delta R(\ell\ell)$	$((\Delta\eta(\ell\ell))^2 + (\Delta\phi(\ell\ell))^2)^{1/2}$	√	√	√	√		√
$M(\ell\ell)$	Invariant mass of dilepton pair	√	√	√			√
$E_T(j_1)$	Transverse energy of the leading jet			√		√	
$E_T(j_2)$	Transverse energy of the subleading jet			√			
$\eta(j_1)$	Pseudorapidity of the leading jet			√			
$\eta(j_2)$	Pseudorapidity of the subleading jet			√			
$\Delta\phi(jj)$	Azimuthal angle between two leading jets			√			
$\Delta\eta(jj)$	Difference in pseudorapidities of two leading jets			√			
$\Delta R(jj)$	$((\Delta\eta(jj))^2 + (\Delta\phi(jj))^2)^{1/2}$			√			
$M(jj)$	Invariant mass of two leading jets			√			
N_{jets}	Number of jets in event					√	
ΣE_T(jets)	Scalar sum of transverse jet energies			√		√	
$\Sigma E_T(\ell, \text{jets})$	Scalar sum of lepton p_T and jet (if any) E_T			√	√		
$\lvert\Sigma\vec{E}_T\rvert$	Magnitude of vector sum of lepton p_T and jet (if any) E_T				√		
$\not\!\!E_T$	Missing transverse energy					√	√
$\Sigma E_T(\ell, \not\!\!E_T)$	Scalar sum of transverse lepton momenta and the $\not\!\!E_T$			√	√		
$\Delta\phi(\not\!\!E_T, \ell)$	Azimuthal angle between e or μ candidate and $\not\!\!E_T$						√
$\Delta\phi(\not\!\!E_T, \tau)$	Azimuthal angle between τ candidate and $\not\!\!E_T$						√
$\Delta\phi(\ell\ell, \not\!\!E_T)$	Azimuthal angle between $\vec{p}_T(\ell_1) + \vec{p}_T(\ell_2)$ and the $\not\!\!E_T$		√	√			
$\Delta\phi(\not\!\!E_T, \ell$ or jet)	Azimuthal angle between the $\not\!\!E_T$ and nearest lepton or jet		√		√	√	
$\not\!\!E_T^{\text{spec}}$	Projection of $\not\!\!E_T$ on nearest lepton or jet or $\not\!\!E_T$ if $\Delta\phi(\not\!\!E_T, \ell$ or jet$) > \pi/2$	√	√	√	√	√	
$\not\!\!E_T^{\text{sig}}$	$\not\!\!E_T/(\Sigma E_T(\ell, \text{jets}))^{1/2}$		√	√	√	√	√
$M_T(\ell, \not\!\!E_T)$	Transverse mass of e or μ candidate and $\not\!\!E_T$						√
$M_T(\tau, \not\!\!E_T)$	Transverse mass of τ candidate and $\not\!\!E_T$						√
$M_T(\ell, \ell, \not\!\!E_T)$	Transverse mass of the two leptons and the $\not\!\!E_T$	√	√	√			
$M_T(\ell, \ell, \not\!\!E_T, \text{jets})$	Transverse mass of the two leptons, all jets, and the $\not\!\!E_T$			√			
H_T	Scalar sum of lepton p_T, jet E_T, and the $\not\!\!E_T$	√		√	√		
C	Centrality based on leptons, jets and the $\not\!\!E_T$		√				
A	Aplanarity based on leptons, jets and the $\not\!\!E_T$			√			
$LR(HWW)$	ME-based likelihood for ggH Higgs boson production	√					
$LR(WW)$	ME-based likelihood for nonresonant W^+W^- production	√					
$\cos(\Delta\phi(\ell\ell))^{\text{CM}}$	Cosine of the azimuthal angle between the leptons in the Higgs boson rest frame		√	√			
$\cos(\psi(\ell_2))^{\text{CM}}$	Cosine of angle between subleading lepton and Higgs boson in Higgs boson rest frame			√			

trajectories, and angles between the lepton and jet momenta in the events. The scalar sums of transverse momenta, including or excluding $\not\!\!E_T$, are also considered.

The OS base (0 jet) search samples have the best individual sensitivity to a potential Higgs boson signal. The dominant Higgs boson production process contributing to these samples is ggH, but small ($\approx 5\%$) contributions from other production mechanisms are considered. The primary background contribution (over 40%) to these samples is from direct W^+W^- production and neural networks are trained specifically to distinguish this background from potential ggH-produced Higgs boson events. In this case, the neural network input variables include matrix-element likelihood ratios, $LR(HWW)$ and $LR(WW)$, along with the following eight kinematic event variables: $\Delta\phi(\ell\ell)$, $\Delta R(\ell\ell)$, $M(\ell\ell)$, $p_T(\ell_1)$, $p_T(\ell_2)$, H_T, $M_T(\ell,\ell,\not\!\!E_T)$, and $\not\!\!E_T^{\rm spec}$. Distributions of the most discriminating among these variables, $\Delta\phi(\ell\ell)$ and $LR(HWW)$, are shown in Figs. 5(a) and 5(b) for the high s/b leptons sample and in Figs. 5(c) and 5(d) for the low s/b leptons sample. These variables are sensitive to the spin correlations between the two W bosons produced in the decay of the spin-0 Higgs boson, which tend to result in events with collinear leptons. Separate neural networks are trained for each tested Higgs boson mass using combined samples of modeled signal and background events containing both high and low s/b lepton candidates. These networks are then applied independently to both the high and low s/b leptons search samples. Examples of neural network output distributions for Higgs boson masses of 125 and 165 GeV/c^2 are shown in Figs. 6(a) and 6(b) for the high s/b leptons sample and in Figs. 6(c) and 6(d) for the low s/b leptons sample. These distributions illustrate the ability of the neural network to efficiently separate potential signal events from background contributions with the exception of direct W^+W^- production, which is indistinguishable from signal in a portion of phase space.

For the OS base (1 jet) search samples, the VH and VBF Higgs boson production mechanisms contribute more significantly, accounting for $\approx 25\%$ of the potential signal. Background contributions from DY events, which contain significant missing energy due to jet energy mismeasurements, are also relevant. Neural networks for these search samples are based on the following 12 kinematic input variables: $\Delta R(\ell\ell)$, $M(\ell\ell)$, $p_T(\ell_1)$, $p_T(\ell_2)$, $M_T(\ell,\ell,\not\!\!E_T)$, $\not\!\!E_T^{\rm spec}$, $E(\ell_1)$, $\Delta\phi(\not\!\!E_T, \ell$ or jet), $\Delta\phi(\ell\ell,\not\!\!E_T)$,

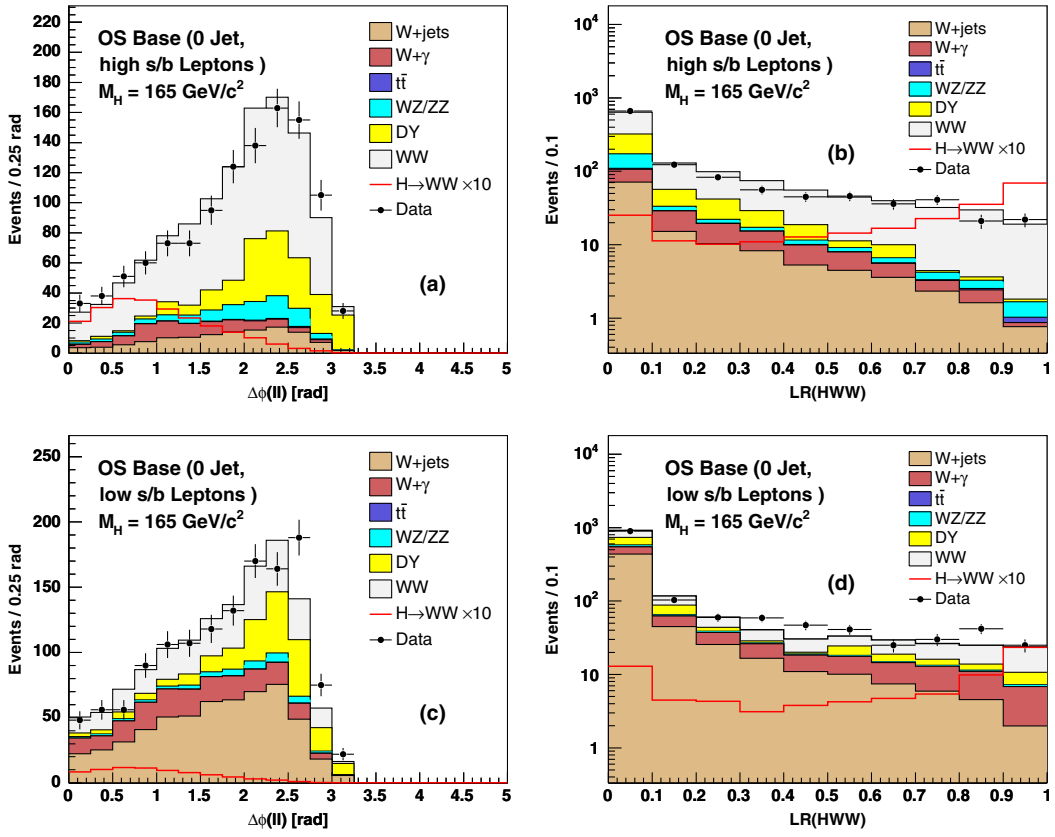

FIG. 5 (color online). Predicted and observed distributions of kinematic input variables providing the largest separation between potential signal and background contributions in the (a),(b) OS base (0 jet, high s/b leptons) and (c),(d) OS base (0 jet, low s/b leptons) search samples. The overlaid signal predictions correspond to the sum of four production modes (ggH, WH, ZH, and VBF) for a Higgs boson with mass of 165 GeV/c^2 and are multiplied by a factor of 10 for visibility. Normalizations for background event yields are those obtained from the final fit used to extract search limits.

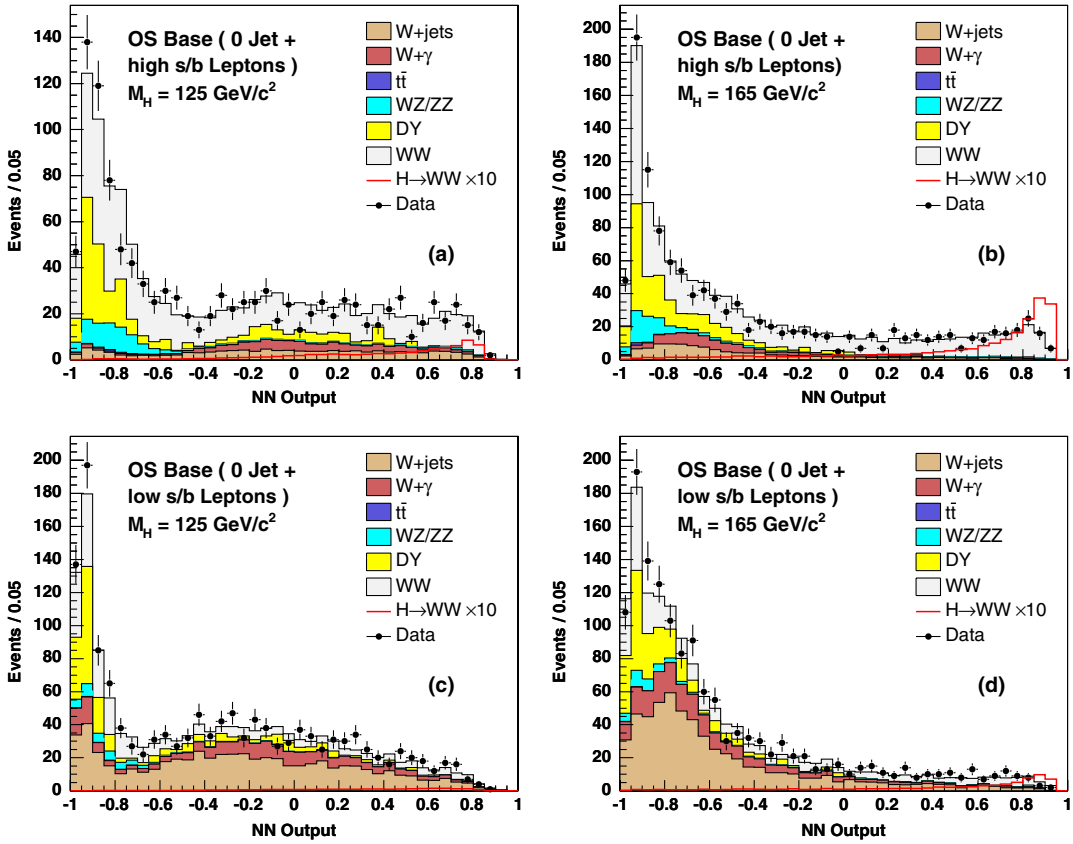

FIG. 6 (color online). Predicted and observed distributions of neural network output variables for networks trained to separate potential Higgs boson events from background contributions in the (a),(b) OS base (0 jet, high s/b leptons) and (c),(d) OS base (0 jet, low s/b leptons) search samples for Higgs boson mass hypotheses of 125 and 165 GeV/c^2. The overlaid signal predictions correspond to the sum of four production modes (ggH, WH, ZH, and VBF) and are multiplied by a factor of 10 for visibility. Normalizations for background event yields are those obtained from the final fit used to extract search limits.

$\cos(\Delta\phi(\ell\ell))_{\rm CM}$, $\not\!\!E_T^{\rm sig}$, and C. Distributions of the most discriminating among these variables, $\Delta R(\ell\ell)$ and $\not\!\!E_T^{\rm spec}$, are shown in Figs. 7(a) and 7(b) for the high s/b leptons sample and in Figs. 7(c) and 7(d) for the low s/b leptons sample. The $\Delta R(\ell\ell)$ variable provides good discrimination against significant W^+W^- contributions, while the $\not\!\!E_T^{\rm spec}$ variable is useful for separating the signal from larger DY contributions. Training of the neural networks is based on combined samples containing events with both high and low s/b lepton candidates. The resulting networks are then applied separately to the two search samples containing the events with high and low s/b leptons. Examples of neural network output distributions for Higgs boson masses of 125 and 165 GeV/c^2 are shown in Figs. 8(a) and 8(b) for the high s/b leptons sample and in Figs. 8(c) and 8(d) for the low s/b leptons sample.

In the OS base (≥ 2 jets) search sample the VH and VBF Higgs boson production mechanisms account for $\approx$ 65% of the total expected signal. Even after rejecting events with a jet tagged as likely to have originated from a bottom quark, roughly 50% of background events are estimated to originate from $t\bar{t}$ production. Two neural networks are trained to distinguish signal from background. One network distinguishes ggH production from background contributions without using jet kinematic information. The second network incorporates jet-related variables as inputs and is trained to separate VH and VBF production, which result in events with multiple jets at LO, from background contributions. A single, final discriminant is obtained by taking the higher of the two discriminant values obtained from the individual neural networks. We follow this approach to avoid dependence on the PYTHIA modeling of the higher-order processes within ggH production, which yield the small fraction of ggH events containing multiple jets. Higgs boson events from ggH production are dominantly selected by the first network minimizing any potential mismodeling effects. The 17 kinematic input variables used for both networks are $\Delta\phi(\ell\ell)$, $\Delta R(\ell\ell)$, $M(\ell\ell)$, $p_T(\ell_1)$, $p_T(\ell_2)$, H_T, $M_T(\ell,\ell,\not\!\!E_T)$, $M_T(\ell,\ell,\not\!\!E_T,\text{jets})$, $\not\!\!E_T^{\rm spec}$, $\Sigma E_T(\ell,\not\!\!E_T)$, $\Delta\phi(\ell\ell,\not\!\!E_T)$, $\Sigma E_T(\ell,\text{jets})$, $\cos(\Delta\phi(\ell\ell))_{\rm CM}$, $\cos(\psi(\ell_2))_{\rm CM}$, $\not\!\!E_T^{\rm sig}$, A, and $\Sigma E_T(\text{jets})$. The additional 8 jet-related variables used as inputs to the network trained for separating VH and VBF production are $M(jj)$, $\Delta\phi(jj)$, $\Delta\eta(jj)$, $\Delta R(jj)$, $E_T(j_1)$, $E_T(j_2)$, $\eta(j_1)$, and $\eta(j_2)$. In the case of this second network, the 4 combinations of the total 23

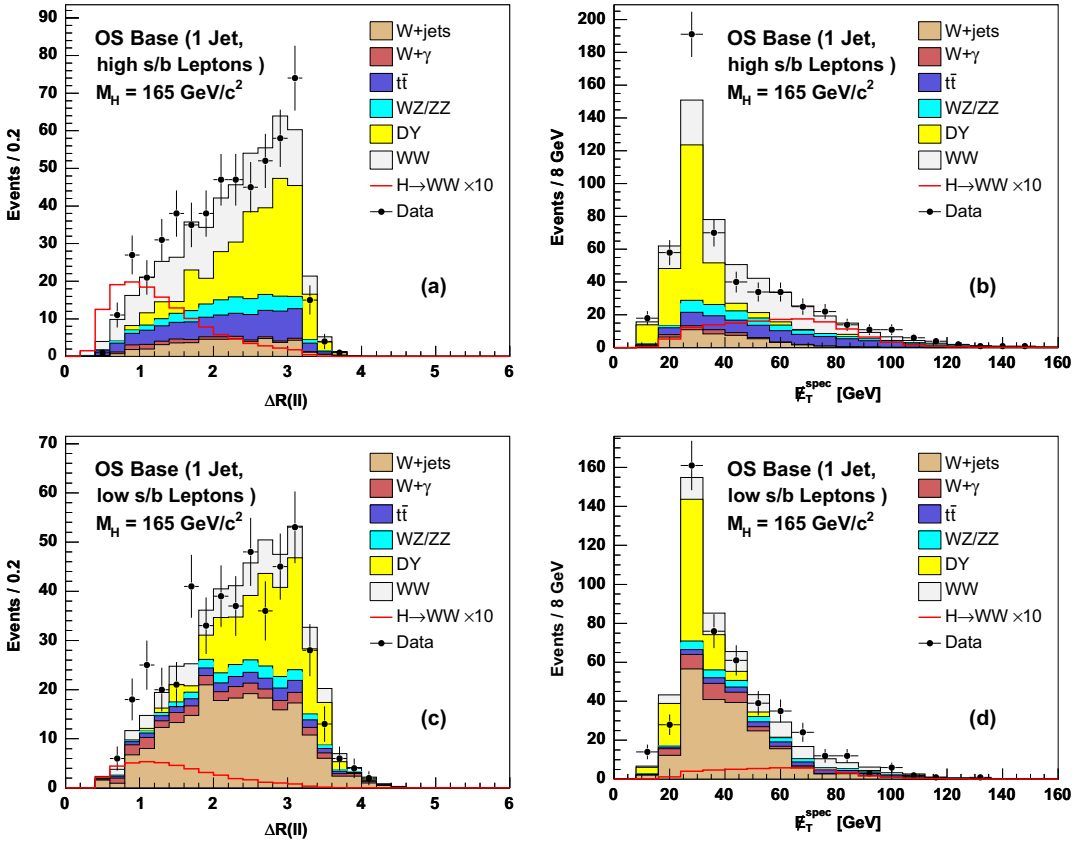

FIG. 7 (color online). Predicted and observed distributions of kinematic input variables providing the largest separation between potential signal and background contributions in the (a),(b) OS base (1 jet, high s/b leptons) and (c),(d) OS base (1 jet, low s/b leptons) search samples. The overlaid signal predictions correspond to the sum of four production modes (ggH, WH, ZH, and VBF) for a Higgs boson with mass of 165 GeV$/c^2$ and are multiplied by a factor of 10 for visibility. Normalizations for background event yields are those obtained from the final fit used to extract search limits.

variables most discriminating for Higgs boson mass of 125, 140, 160, and 185 GeV$/c^2$, are reused as inputs to networks trained for neighboring mass values. Distributions of the variables found to contain the largest discriminating power, $M(\ell\ell)$ and $\Delta\phi(\ell\ell, \not\!\!E_T)$, are shown in Figs. 9(a) and 9(b). Using a large number of network input variables makes it possible to separate the large number of signal and background processes that contribute to this sample. Specific variables are targeted, for example, at identifying the W boson spin correlation associated with the decay of the spin-0 Higgs boson, the hadronic decay of a third vector boson associated with VH production, the large rapidity gap present between the additional jets originating from VBF production, the high overall energy in events from top-quark pair production, and the Z boson associated with either DY or direct WZ and ZZ production. Examples of neural network output distributions for this search sample are shown in Figs. 10(a) and 10(b) for Higgs boson masses of 125 and 165 GeV$/c^2$, respectively.

Including the OS inverse $M_{\ell\ell}$ search sample leads to an overall gain in signal acceptance of approximately 35%, with respect to that of the combined OS base search samples, for a Higgs boson with $m_H = 125$ GeV$/c^2$. In this sample the dominant signal contribution is from ggH production, although smaller contributions from VH and VBF production are considered. The largest background contribution is associated with $W\gamma$ production. The 13 kinematic variables used as inputs to the neural network trained for separating signal and background are $\Delta\phi(\ell\ell)$, $\Delta R(\ell\ell)$, $p_T(\ell_1)$, $p_T(\ell_2)$, H_T, $\not\!\!E_T^{\rm spec}$, $E(\ell_1)$, $E(\ell_2)$, ΣE_T, $|\Sigma \vec{E}_T|$, $\not\!\!E_T^{\rm sig}$, $\Delta\phi(\not\!\!E_T, \ell\,{\rm or\,jet})$, and $\Sigma E_T(\ell, {\rm jets})$. Distributions of the most discriminating among these variables, $\Sigma E_T(\ell, {\rm jets})$ and $\not\!\!E_T^{\rm sig}$, are shown in Figs. 9(c) and 9(d). The two variables exploit the higher total event energy expected from a high-mass Higgs boson decay and the absence of neutrinos in events originating from $W\gamma$ production. Examples of neural network output distributions for this search sample are shown in Figs. 10(c) and 10(d) for Higgs boson masses of 125 and 165 GeV$/c^2$, respectively.

The SS (≥ 1 jets) search sample focuses solely on signal contributions from VH production, in which like-sign charged leptons result from the decays of the associated vector boson and one of two W bosons produced in the

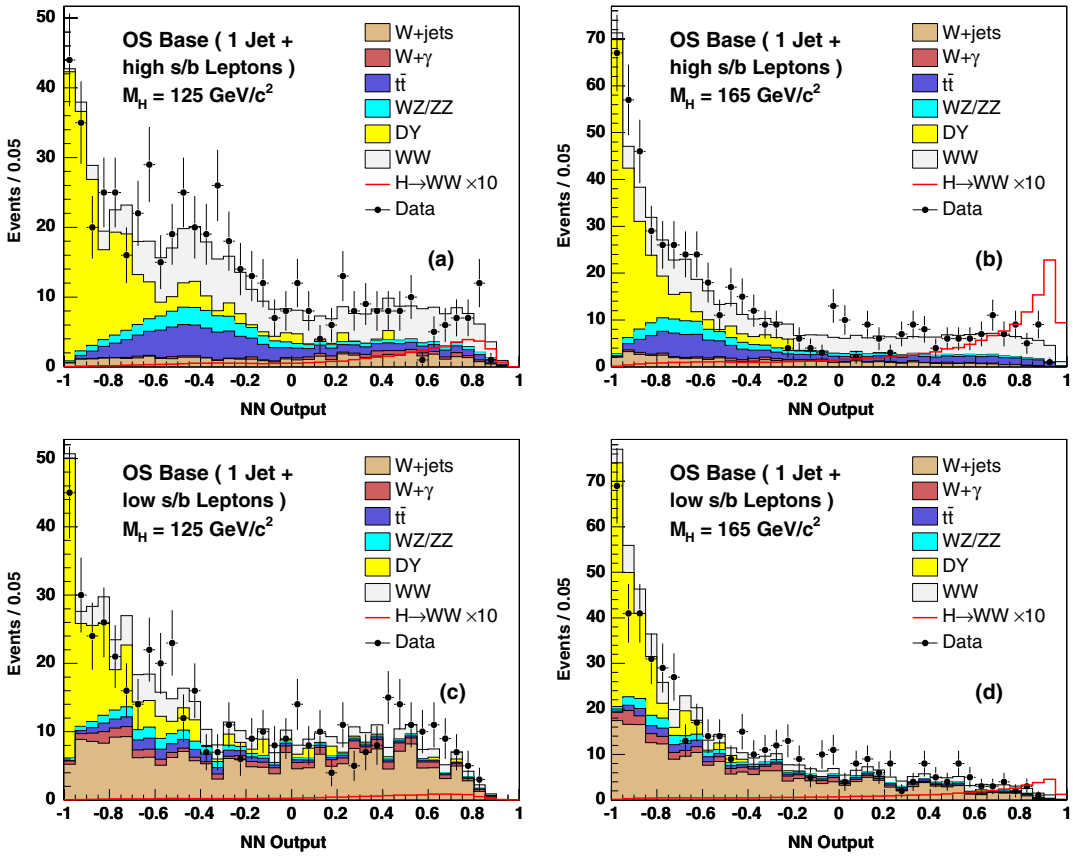

FIG. 8 (color online). Predicted and observed distributions of neural network output variables for networks trained to separate potential Higgs boson events from background contributions in the (a),(b) OS base (1 jet, high s/b leptons) and (c),(d) OS base (1 jet, low s/b leptons) search samples for Higgs boson mass hypotheses of 125 and 165 GeV$/c^2$. The overlaid signal predictions correspond to the sum of four production modes (ggH, WH, ZH, and VBF) and are multiplied by a factor of 10 for visibility. Normalizations for background event yields are those obtained from the final fit used to extract search limits.

Higgs boson decay. Over 50% of background events in the sample are predicted to originate from W + jets production, where the lepton candidate, misidentified from the decay products of the jet, is assigned the same charge as the lepton produced in the W boson decay. The 9 kinematic variables used to train the neural network used for separating signal and backgrounds are $p_T(\ell_1)$, $p_T(\ell_2)$, $\not\!\!E_T$, $\not\!\!E_T^{\text{spec}}$, $\Delta\phi(\not\!\!E_T, \ell \text{ or jet})$, $\not\!\!E_T^{\text{sig}}$, $\Sigma E_T(\text{jets})$, $E_T(j_1)$, and N_{jets}. Distributions of the most discriminating among these variables, $\not\!\!E_T^{\text{sig}}$ and N_{jets}, are shown in Figs. 11(a) and 11(b). These variables are sensitive to the presence of neutrinos and jets associated with leptonic and hadronic decays of the multiple vector bosons originating from the VH production process. Examples of neural network output distributions for this search sample are shown in Figs. 12(a) and 12(b) for Higgs boson masses of 125 and 165 GeV$/c^2$, respectively.

B. Dilepton search samples with hadronically decaying tau leptons

The numbers of expected events from each contributing signal and background process are compared in Table V with the total number of observed events in each of the two dilepton search samples formed from one electron or muon candidate and one hadronically decaying tau lepton candidate. Background and signal predictions, referring to potential Higgs boson masses of 125 and 165 GeV$/c^2$, are taken from the models described in Sec. VI.

Signal and background kinematic properties of events in these samples are similar to those in the other dilepton search samples and the multivariate techniques applied to these samples for separating signal and background contributions use a subset of the kinematic variables in Table IV as inputs. In addition, identification variables associated with the hadronically decaying tau lepton candidate are strongly discriminating against dominant W + jets background contributions, in which a particle jet is misidentified as a hadronically decaying tau lepton candidate. The additional tau lepton identification variables used as inputs to the BDT algorithms applied to these samples are listed in Table VI.

The dominant signal contributions to the OS hadronic tau search samples originate from ggH production, although contributions from the VH and VBF production mechanisms are also considered. Over 80% of events in

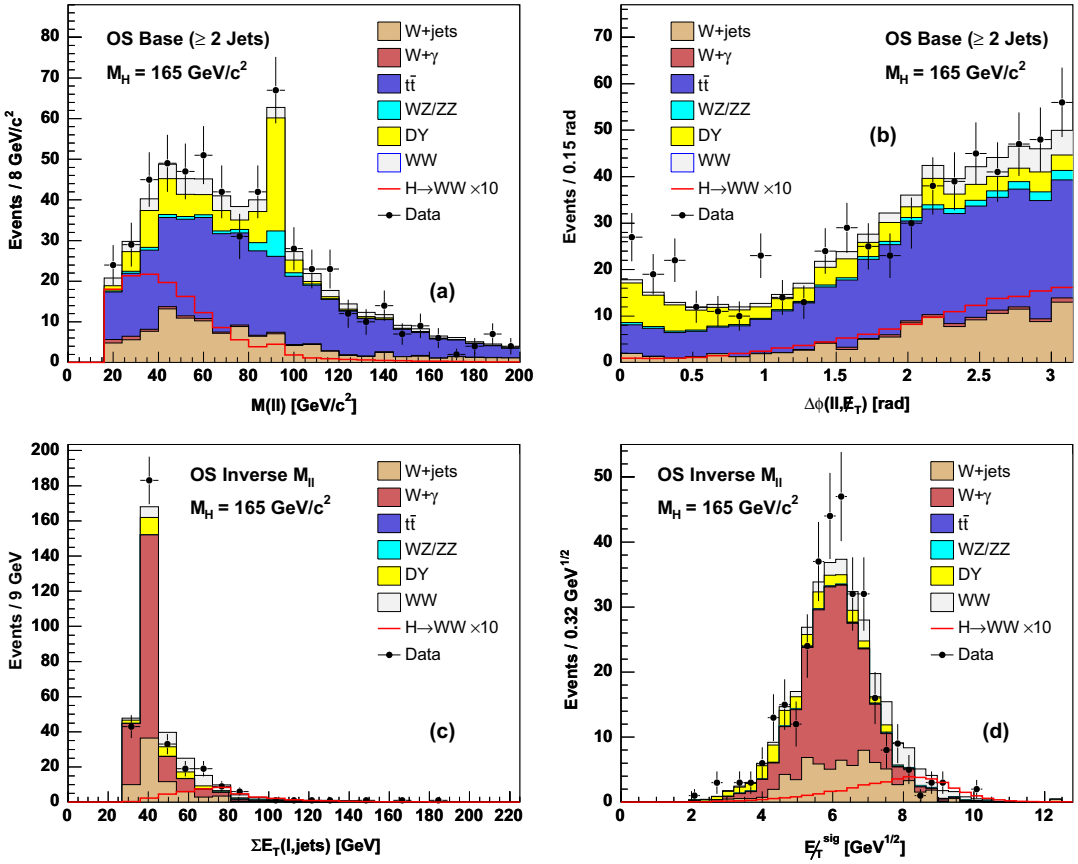

FIG. 9 (color online). Predicted and observed distributions of kinematic input variables providing the largest separation between potential signal and background contributions in the (a),(b) OS base (≥ 2 jets) and (c),(d) OS inverse $M_{\ell\ell}$ search samples. The overlaid signal predictions correspond to the sum of four production modes (ggH, WH, ZH, and VBF) for a Higgs boson with mass of 165 GeV$/c^2$ and are multiplied by a factor of 10 for visibility. Normalizations for background event yields are those obtained from the final fit used to extract search limits.

these samples are predicted to originate from W + jet production. A BDT algorithm, with a combined set of dilepton kinematic and tau lepton identification variables as inputs, is used to provide a single output variable for distinguishing potential signal events from the large background contributions. The best separation is obtained when the BDT algorithm is trained solely to distinguish ggH signal from W + jet background contributions. Although the same set of input variables are used, independent BDT algorithms are trained for the $e + \tau_{\rm had}$ and $\mu + \tau_{\rm had}$ search samples to exploit differences in the distributions of reconstructed electron and muon candidates.

The 12 kinematic variables used as inputs to the BDT algorithms are $\Delta\phi(\ell\ell)$, $\Delta\eta(\ell\ell)$, $\Delta R(\ell\ell)$, $M(\ell\ell)$, $p_T(\ell_1)$, $\not\!\!E_T$, $\not\!\!E_T^{\rm sig}$, $\Sigma E_T(\ell, \text{jets})$, $\Delta\phi(\not\!\!E_T, \ell)$, $\Delta\phi(\not\!\!E_T, \tau)$, $M_T(\ell, \not\!\!E_T)$, and $M_T(\tau, \not\!\!E_T)$. All 11 tau lepton identification variables listed in Table VI are also used. Distributions of the most discriminating variables, $\Sigma P_T(\text{iso cone})$ and $\theta_{\rm track}^{\rm closest}$, are shown in Figs. 13(a) and 13(b) for the $e + \tau_{\rm had}$ sample and in Figs. 13(c) and 13(d) for the $\mu + \tau_{\rm had}$ sample. These variables primarily separate events containing real and misidentified hadronically decaying tau lepton candidates. Examples of BDT output distributions for Higgs boson masses of 125 and 165 GeV$/c^2$ are shown in Figs. 14(a) and 14(b) for the $e + \tau_{\rm had}$ sample and in Figs. 14(c) and 14(d) for the $\mu + \tau_{\rm had}$ sample.

C. Trilepton search samples

The numbers of expected events from each contributing signal and background process are compared in Table VII with the total number of observed events in each of the four trilepton search samples. Background and signal predictions, referring to potential Higgs boson masses of 125 and 165 GeV$/c^2$, are taken from the models described in Sec. VI.

A summary of the kinematic variables used as inputs to the multivariate algorithms in these four search samples is shown in Table VIII. For the Trilepton $WH(\ell + \ell + \tau_{\rm had})$ sample, identification variables associated with the hadronically decaying tau lepton candidate are also important for suppressing the dominant Z + jets background contribution and are included as inputs to the multivariate algorithm. These variables are listed in Table VI.

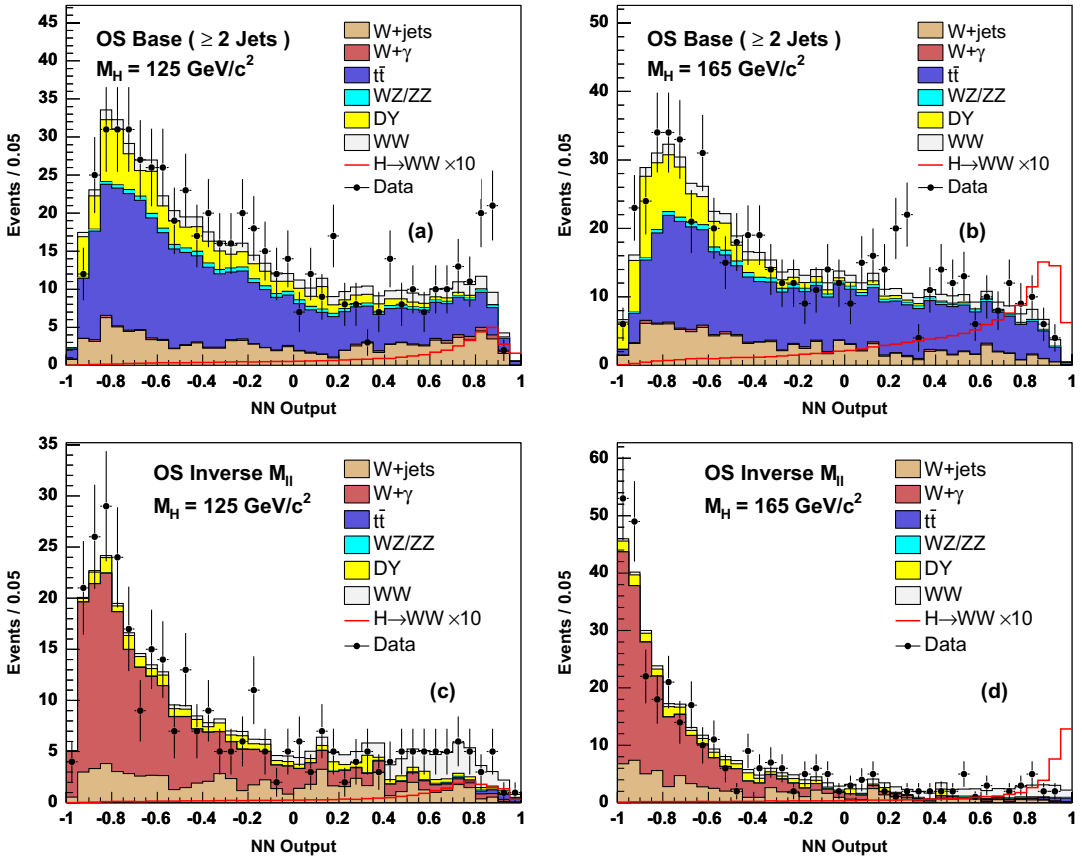

FIG. 10 (color online). Predicted and observed distributions of neural network output variables for networks trained to separate potential Higgs boson events from background contributions in the (a),(b) OS base (≥ 2 jets) and (c),(d) OS inverse $M_{\ell\ell}$ search samples for Higgs boson mass hypotheses of 125 and 165 GeV/c^2. The overlaid signal predictions correspond to the sum of four production modes (ggH, WH, ZH, and VBF) and are multiplied by a factor of 10 for visibility. Normalizations for background event yields are those obtained from the final fit used to extract search limits.

In all trilepton search samples, signal contributions from ggH and VBF production are negligible, and we consider potential event yields from VH production only. For the Trilepton WH search sample, approximately 50% of background events originate from direct WZ production. The neural network trained for this sample uses the following 14 kinematic variables as inputs: $p_T(\ell_2)$, $\Delta R(\ell^+\ell^-)_{\text{near}}$, $\Delta R(\ell^+\ell^-)_{\text{far}}$, $M_T(\ell,\ell,\ell)$, N_{jets}, $\not\!\!E_T$,

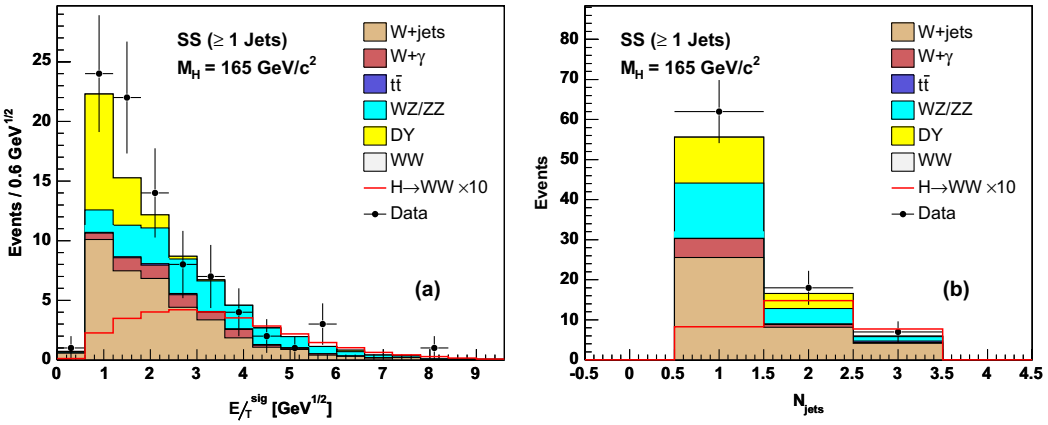

FIG. 11 (color online). Predicted and observed distributions of kinematic input variables providing the largest separation between potential signal and background contributions in the SS (≥ 1 jets) search sample. The overlaid signal predictions correspond to the sum of two production modes (WH and ZH) for a Higgs boson with mass of 165 GeV/c^2 and are multiplied by a factor of 10 for visibility. Normalizations for background event yields are those obtained from the final fit used to extract search limits.

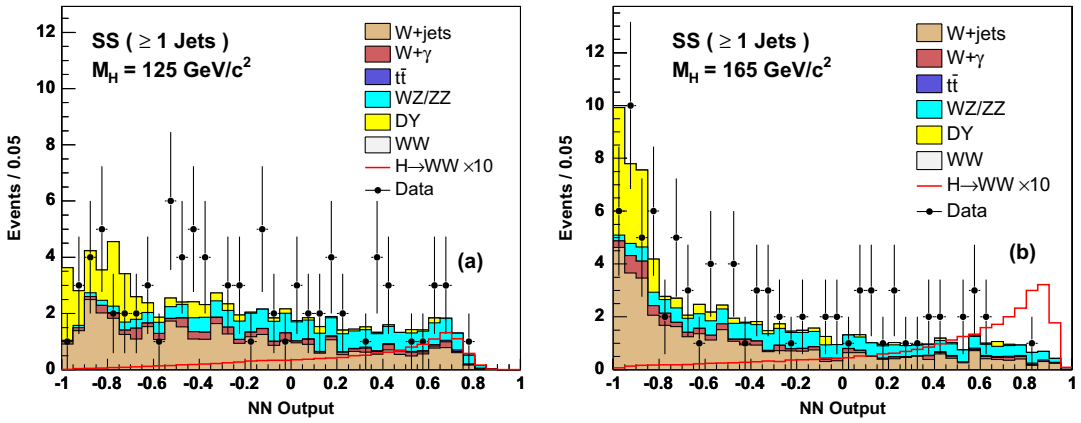

FIG. 12 (color online). Predicted and observed distributions of neural network output variables for networks trained to separate potential Higgs boson events from background contributions in the SS (≥ 1 jets) search sample for Higgs boson mass hypotheses of 125 and 165 GeV/c^2. The overlaid signal predictions correspond to the sum of two production modes (WH and ZH) and are multiplied by a factor of 10 for visibility. Normalizations for background event yields are those obtained from the final fit used to extract search limits.

$\Delta\phi(\ell_2, \not\!\!E_T)$, $M_T(\ell_3, \not\!\!E_T)$, $M_T(\ell, \ell, \ell, \not\!\!E_T, \text{jets})$, $M(\ell_3, \not\!\!E_T, \text{jets})$, $M(\ell_1, \ell_2, \not\!\!E_T)$, $M(\ell^+\ell^-)_{\text{near}}$, H_T, and $F(\ell\ell\ell)$. Distributions of the most discriminating among these variables, $\Delta R(\ell^+\ell^-)_{\text{near}}$ and $\not\!\!E_T$, are shown in Figs. 15(a) and 15(b).

TABLE V. Summary of predicted and observed event yields for two dilepton search samples formed from one electron or muon candidate and one hadronically decaying tau lepton candidate. Expected signal yields are shown for potential SM Higgs boson masses of 125 and 165 GeV/c^2. The procedures used to determine the overall normalizations of modeled background event yields for each of the contributing processes are described in Sec. VI.

Process	OS hadronic tau ($e + \tau_{\text{had}}$)	OS hadronic tau ($\mu + \tau_{\text{had}}$)
$t\bar{t}$	15.6 ± 2.3	11.3 ± 1.7
WW, WZ, and ZZ	25.1 ± 3.7	19.5 ± 2.9
Multijet and γ + jet	0^{+34}_{-0}	0^{+29}_{-0}
DY ($Z \to \tau\tau$)	0.5 ± 0.2	1.2 ± 0.8
DY ($Z \to ee$, $\mu\mu$)	14.4 ± 3.6	78 ± 12
W + jets	745 ± 123	514 ± 85
$W\gamma$	2.5 ± 0.4	2.3 ± 0.3
Total background	803 ± 126	626 ± 89
	$M_H = 125$ GeV/c^2	
ggH	0.12 ± 0.02	0.09 ± 0.02
WH	0.07 ± 0.01	0.05 ± 0.01
ZH	0.04 ± 0.01	0.03 ± 0.01
VBF	0.01 ± 0.00	0.01 ± 0.00
Total signal	0.24 ± 0.03	0.18 ± 0.02
	$M_H = 165$ GeV/c^2	
ggH	1.07 ± 0.18	0.80 ± 0.13
WH	0.25 ± 0.03	0.17 ± 0.02
ZH	0.15 ± 0.02	0.11 ± 0.02
VBF	0.10 ± 0.02	0.08 ± 0.01
Total signal	1.56 ± 0.21	1.16 ± 0.15
Data	792	598

The purpose of these variables is to isolate the collinear leptons originating from the spin correlations between the two W bosons produced in the decay of the spin-0 Higgs boson and the large missing transverse energy associated with the neutrinos produced in the leptonic decays of three W bosons. Examples of neural network output distributions for this search sample are shown in Figs. 16(a) and 16(b) for Higgs boson masses of 125 and 165 GeV/c^2, respectively.

For the Trilepton WH ($\ell + \ell + \tau_{\text{had}}$) search sample, $\approx$ 80% of background events originate from Z + jets production. A BDT is used to combine both kinematic and tau lepton identification variables as inputs to the multivariate algorithm. The 16 kinematic variables used as inputs to the BDT algorithm are $p_T(\ell_1)$, $p_T(\ell_2)$, $p_T(\ell_3)$, $\Delta R(\ell^+\ell^-)_{\text{near}}$, $\Delta R(\ell^+\ell^-)_{\text{far}}$, $M_T(\ell, \ell, \ell)$, $M(\ell\ell\ell)$, $\not\!\!E_T$, $\Delta\phi(\ell_2, \not\!\!E_T)$, $\not\!\!E_T^{\text{sig}}$, $M_T(\ell_3, \not\!\!E_T)$, $M_T(\ell, \ell, \ell, \not\!\!E_T, \text{jets})$, $M(\ell_3, \not\!\!E_T, \text{jets})$, $M(\ell_1, \ell_2, \not\!\!E_T)$, $M(\ell^+\ell^-)_{\text{near}}$, and H_T. The 11 tau lepton identification variables listed in Table VI are also used. Distributions of the most discriminating among these variables, $\Delta R(\ell^+\ell^-)_{\text{far}}$ and $\not\!\!E_T$, are shown in Figs. 15(c) and 15(d). Examples of BDT output distributions are shown in Figs. 16(c) and 16(d) for Higgs boson masses of 125 and 165 GeV/c^2, respectively.

For the Trilepton ZH search samples, the presence of an opposite-sign dilepton pair with a mass consistent with the Z boson mass ensures that potential signal contributions originate almost exclusively from ZH production. Likewise, most background event contributions originate from processes containing a real Z boson ($\approx$ 50% from direct WZ and ZZ production). Neural networks are trained to separate these background contributions from signal. Typically, one of the W bosons decays hadronically, yielding potentially multiple reconstructed jets within each event. Hence, potential signal contributions in the (1 jet) search sample are smaller

TABLE VI. Summary of identification variables associated with a hadronically decaying tau lepton candidate used as inputs to the multivariate algorithms for separating signal and background contributions.

Variable	Definition	OS hadronic tau	Trilepton WH ($\ell + \ell + \tau_{\rm had}$)
$p_T^{\rm seed}$	Transverse momentum of tau candidate seed track	√	√
$d_0^{\rm seed}$	Impact parameter of tau candidate seed track with respect to primary vertex	√	√
$E_T^{\rm vis}$	Tau candidate visible transverse energy	√	√
$M_T^{\rm vis}$	Tau candidate visible mass	√	√
$I_{\rm track}$	Tau candidate track isolation	√	√
ΣP_T(iso cone)	Scalar sum of track p_T for all tracks within isolation cone not used in reconstruction of tau candidate	√	√
ΣE_T(iso cone)	Scalar sum of π^0 candidate E_T for all candidates within isolation cone not used in reconstruction of tau candidate	√	√
$p_T^{\rm closest}$	p_T of track closest to direction of tau candidate visible momentum	√	√
$E_T^{\rm closest}$	E_T of π^0 candidate closest to direction of tau candidate visible momentum	√	√
$\theta_{\rm track}^{\rm closest}$	Angle between tau candidate and the closest track	√	√
$\theta_{\pi^0}^{\rm closest}$	Angle between tau candidate and the closest π^0 candidate	√	√

than those in the (≥ 2 jets) sample. In addition, the possibility of reconstructing all Higgs boson decay products in the (≥ 2 jets) sample events allows for the full reconstruction of a Higgs boson mass, which provides an additional highly discriminating variable to enhance signal-to-background separation.

For the Trilepton ZH (1 jet) sample, a large number of kinematic variables are used as inputs to the neural

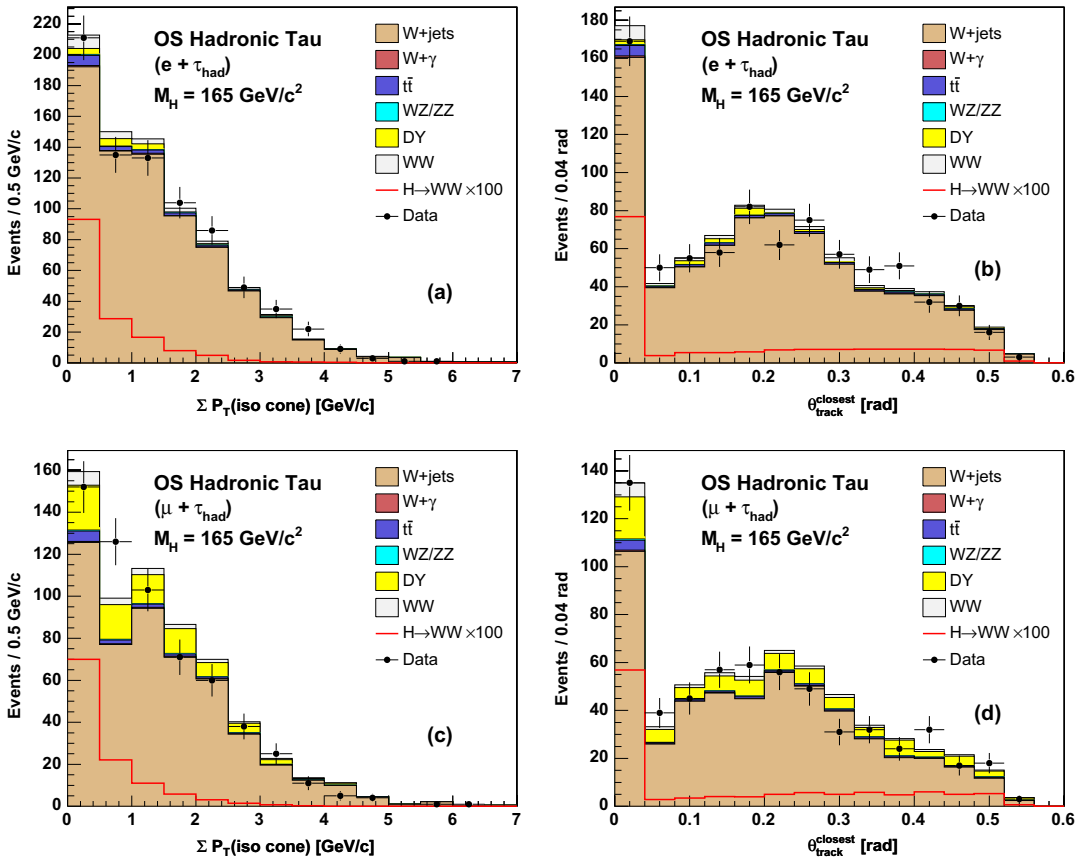

FIG. 13 (color online). Predicted and observed distributions of kinematic input variables providing the largest separation between potential signal and background contributions in the (a),(b) OS hadronic tau ($e + \tau_{\rm had}$) and (c),(d) OS hadronic tau ($\mu + \tau_{\rm had}$) search samples. The overlaid signal predictions correspond to the sum of four production modes (ggH, WH, ZH, and VBF) for a Higgs boson with mass of 165 GeV/c^2 and are multiplied by a factor of 100 for visibility. Normalizations for background event yields are those obtained from the final fit used to extract search limits.

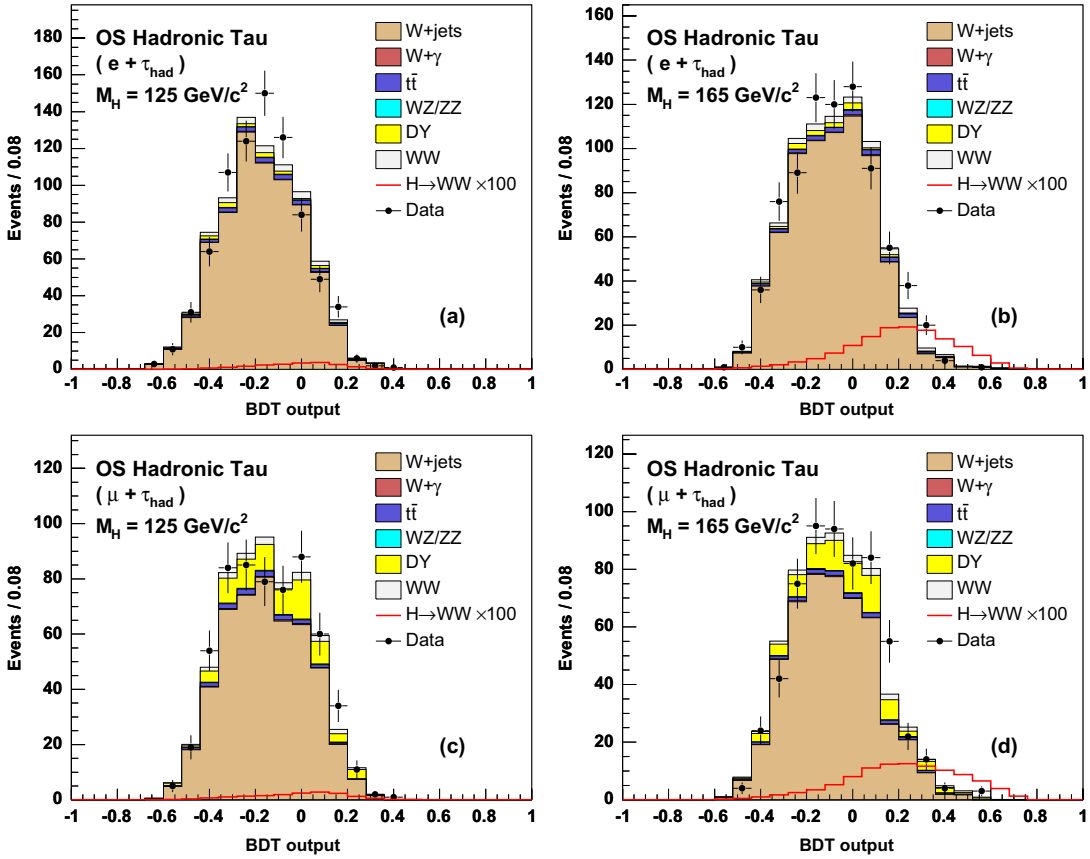

FIG. 14 (color online). Predicted and observed distributions of BDT output variables for trees trained to separate potential Higgs boson events from background contributions in the (a),(b) OS hadronic tau ($e + \tau_{\rm had}$) and (c),(d) OS hadronic tau ($\mu + \tau_{\rm had}$) search samples for Higgs boson mass hypotheses of 125 and 165 GeV/c^2. The overlaid signal predictions correspond to the sum of four production modes (ggH, WH, ZH, and VBF) and are multiplied by a factor of 100 for visibility. Normalizations for background event yields are those obtained from the final fit used to extract search limits.

network to maximally constrain the missing kinematic information associated to the unreconstructed jet. The 16 kinematic input variables to the neural network are $\Delta R(\ell^+\ell^-)_{\rm near}$, $\Delta R(\ell^+\ell^-)_{\rm far}$, $M(\ell\ell\ell)$, $E_T(j_1)$, $\not\!\!E_T$, $\Delta\phi(\ell_1 + \ell_2 + \ell_3, \not\!\!E_T)$, $\Delta\phi(\ell_2, \not\!\!E_T)$, $M_T(\ell, \ell, \ell, \not\!\!E_T, \text{jets})$, $M(\ell_3, \not\!\!E_T, \text{jets})$, H_T, $F(\ell\ell\ell)$, $\Delta\phi(\ell_{\rm noZ}, \not\!\!E_T)$, $\Delta R(\ell_{\rm noZ}, j_1)$, $M_T(\ell_{\rm noZ}, \not\!\!E_T)$, $M_T(\ell_{\rm noZ}, \not\!\!E_T, \text{jets})$, and $M(\ell_{\rm noZ}, \not\!\!E_T)$. Distributions of the most discriminating among these

TABLE VII. Summary of predicted and observed event yields for four trilepton search samples. Expected signal yields are shown for potential SM Higgs boson masses of 125 and 165 GeV/c^2. The procedures used to determine the overall normalizations of modeled background event yields for each of the contributing processes are described in Sec. VI.

Process	Trilepton WH	Trilepton WH ($\ell + \ell + \tau_{\rm had}$)	Trilepton ZH (1 jet)	Trilepton ZH (≥ 2 jets)
$t\bar{t}$	0.75 ± 0.23	2.1 ± 0.4	0.12 ± 0.05	0.2 ± 0.04
WZ and ZZ	10.1 ± 1.2	3.7 ± 0.7	19.9 ± 2.4	10.0 ± 1.6
Z + jets	4.9 ± 1.1	31.6 ± 6.1	9.9 ± 2.3	7.8 ± 1.4
$Z\gamma$	4.87 ± 0.97	2.6 ± 0.4	7.8 ± 1.6	3.0 ± 0.8
Total background	20.6 ± 2.2	40.0 ± 6.5	37.7 ± 4.6	20.9 ± 3.1
		$M_H = 125$ GeV/c^2		
WH	0.49 ± 0.07	0.11 ± 0.02	0.02 ± 0.01	0.01 ± 0.01
ZH	0.11 ± 0.02	0.05 ± 0.01	0.24 ± 0.04	0.30 ± 0.04
Total signal	0.60 ± 0.08	0.16 ± 0.02	0.26 ± 0.04	0.30 ± 0.04
		$M_H = 165$ GeV/c^2		
WH	1.03 ± 0.14	0.30 ± 0.04	0.04 ± 0.01	0.02 ± 0.01
ZH	0.24 ± 0.03	0.11 ± 0.02	0.31 ± 0.05	0.8 ± 0.1
Total signal	1.27 ± 0.17	0.41 ± 0.06	0.35 ± 0.05	0.8 ± 0.1
Data	20	28	38	26

TABLE VIII. Summary of kinematic variables used as inputs to the multivariate algorithms for separating signal and background contributions in the trilepton search samples.

Variable	Definition	Trilepton WH	Trilepton WH ($\ell+\ell+\tau_{\rm had}$)	Trilepton ZH (1 jet)	Trilepton ZH (≥ 2 jets)
$p_T(\ell_1)$	Transverse momentum of leading lepton		√		
$p_T(\ell_2)$	Transverse momentum of subleading lepton	√	√		
$p_T(\ell_3)$	Transverse momentum of subsubleading lepton		√		
$\Delta R(\ell^+\ell^-)_{\rm near}$	Minimum $\Delta R(\ell\ell)$ among opposite-sign lepton pairs	√	√	√	
$\Delta R(\ell^+\ell^-)_{\rm far}$	Maximum $\Delta R(\ell\ell)$ among opposite-sign lepton pairs	√	√	√	
$M_T(\ell,\ell,\ell)$	Transverse mass of the three leptons	√	√		
$M(\ell\ell\ell)$	Invariant mass of the three leptons		√	√	
$E_T(j_1)$	Transverse energy of the leading jet			√	√
$E_T(j_2)$	Transverse energy of the subleading jet				√
$M(jj)$	Invariant mass of the two leading jets				√
$N_{\rm jets}$	Number of jets in event	√			
$\not\!\!E_T$	Missing transverse energy	√	√	√	√
$\Delta\phi(\ell_2,\not\!\!E_T)$	Azimuthal angle between the subleading lepton and the $\not\!\!E_T$	√	√	√	
$\Delta\phi(\ell_1+\ell_2+\ell_3,\not\!\!E_T)$	Azimuthal angle between $\vec{p}_T(\ell_1)+\vec{p}_T(\ell_2)+\vec{p}_T(\ell_3)$ and the $\not\!\!E_T$			√	
$\not\!\!E_T^{\rm sig}$	$\not\!\!E_T/(\Sigma E_T(\ell,{\rm jets}))^{1/2}$		√		
$M_T(\ell_3,\not\!\!E_T)$	Transverse mass of the subsubleading lepton and the $\not\!\!E_T$	√	√		
$M_T(\ell,\ell,\ell,\not\!\!E_T,{\rm jets})$	Transverse mass of the three leptons, all jets and the $\not\!\!E_T$	√	√	√	
$M(\ell_3,\not\!\!E_T,{\rm jets})$	Invariant mass of the subsubleading lepton, all jets and the $\not\!\!E_T$	√	√	√	
$M(\ell_1,\ell_2,\not\!\!E_T)$	Invariant mass of the leading and subleading leptons and the $\not\!\!E_T$	√	√		
$M(\ell^+\ell^-)_{\rm near}$	Invariant mass of opposite-sign lepton pair closest in $\Delta\phi$	√	√		
H_T	Scalar sum of lepton p_T, jet E_T, and the $\not\!\!E_T$	√	√	√	
$F(\ell\ell\ell)$	Trilepton flavor combination ($3\times e$, μ, or unspecified track)	√		√	√
$\Delta\phi(\ell_{\rm noZ},\not\!\!E_T)$	Azimuthal angle between the lepton not associated with the Z and the $\not\!\!E_T$			√	
$\Delta R(\ell_{\rm noZ},j_1)$	ΔR between lepton not associated with Z and leading jet			√	
$\Delta R(\ell_{\rm noZ},{\rm jet})_{\rm near}$	ΔR between lepton not associated with Z and closest jet				√
$M_T(\ell_{\rm noZ},\not\!\!E_T)$	Transverse mass of lepton not associated with Z and the and the $\not\!\!E_T$			√	√
$M_T(\ell_{\rm noZ},\not\!\!E_T,{\rm jets})$	Transverse mass of lepton not associated with Z, all jets and the and the $\not\!\!E_T$			√	√
$M(\ell_{\rm noZ},\not\!\!E_T)$	Invariant mass of lepton not associated with Z and the $\not\!\!E_T$			√	√
$\Delta R(WW)$	ΔR between hadronically and leptonically decaying W bosons				√

variables, $\Delta R(\ell_{\rm noZ}, j_1)$ and $\not\!\!E_T$, are shown in Figs. 17(a) and 17(b). Examples of neural network output distributions for this search sample are shown in Figs. 18(a) and 18(b) for Higgs boson masses of 125 and 165 GeV/c^2, respectively.

Fewer kinematic input variables are required for the neural network used in the Trilepton ZH (≥ 2 jets) sample due to the additional discrimination contributed by variables related to the reconstructed Higgs boson mass. The following 10 kinematic variables are used as input to the network: $E_T(j_1)$, $E_T(j_2)$, $M(jj)$, $\not\!\!E_T$, $F(\ell\ell\ell)$, $\Delta R(\ell_{\rm noZ},{\rm jet})_{\rm near}$, $M_T(\ell_{\rm noZ},\not\!\!E_T)$, $M_T(\ell_{\rm noZ},\not\!\!E_T,{\rm jets})$, $M(\ell_{\rm noZ},\not\!\!E_T)$, and $\Delta R(WW)$. Distributions of the most discriminating among these variables, $\Delta R(\ell_{\rm noZ},{\rm jet})_{\rm near}$ and

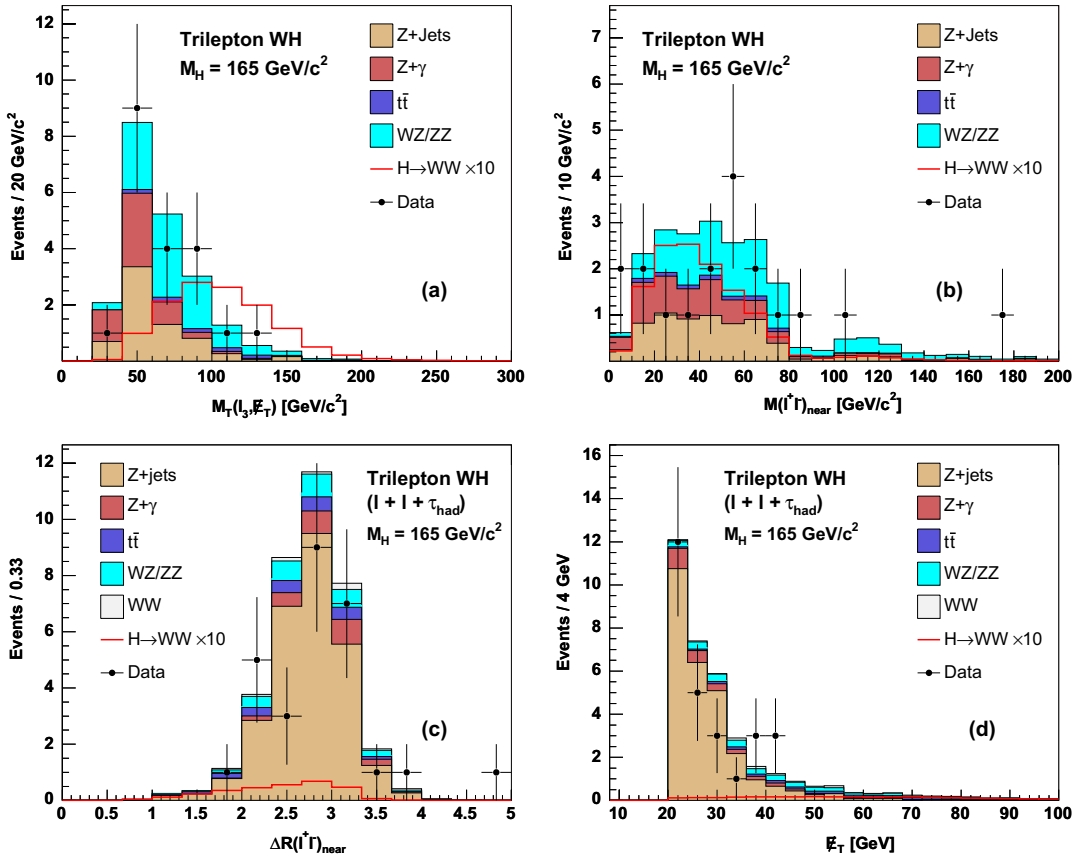

FIG. 15 (color online). Predicted and observed distributions of kinematic input variables providing the largest separation between potential signal and background contributions in the (a),(b) Trilepton WH and (c),(d) Trilepton WH ($\ell + \ell + \tau_{\rm had}$) search samples. The overlaid signal predictions correspond to the sum of two production modes (WH and ZH) for a Higgs boson with mass of 165 GeV/c^2 and are multiplied by a factor of 10 for visibility. Normalizations for background event yields are those obtained from the final fit used to extract search limits.

$\not\!\!E_T$, are shown in Figs. 17(c) and 17(d). Examples of neural network output distributions for this search sample are shown in Figs. 18(c) and 18(d) for Higgs boson masses of 125 and 165 GeV/c^2, respectively.

IX. SYSTEMATIC UNCERTAINTIES

The discriminant output distributions in each of the 13 search samples are combined in a single simultaneous fit to determine the Higgs boson signal rate. Inputs to the fit include both *rate* uncertainties on expected event yields from each specific background and signal process and also *shape* uncertainties on the expected distribution of events within the discriminant outputs for each process. The treatment of these systematic uncertainties in the fit is described in Sec. X. The fit procedure does account for correlations between uncertainties across the different search samples and the different background and signal processes. Rate and shape uncertainties associated with a common source are also treated as correlated.

Rate uncertainties on the contributing background processes are summarized in Table IX for the seven dilepton search samples formed from electron and muon candidates, Table X for the additional two dilepton search samples formed from one electron or muon candidate and one hadronically decaying tau lepton candidate, and Table XI for the four trilepton search samples. Ranges are used to indicate cases where the effect of a specific uncertainty source on the estimated event yield for a contributing background process varies across the different search samples grouped within the individual tables.

All estimated event yields obtained directly from the Monte Carlo simulation are assigned uncertainties from the theoretical cross section calculation, the data luminosity measurement, and the lepton identification and trigger efficiency measurements used to normalize the simulated event samples. In the case of other simulated background samples, whose normalization is obtained from data control samples, these uncertainties are not applicable.

Theoretical diboson production cross sections are taken from MCFM [115] with a renormalization scale of $\mu_0 = M_V^2 + p_T^2(V)$, where M_V is the boson mass, and the MSTW2008 [47] PDF set. Calculations of WZ and ZZ production rates necessarily include contributions from $\gamma^* \to \ell^+\ell^-$ processes, where the invariant dilepton mass

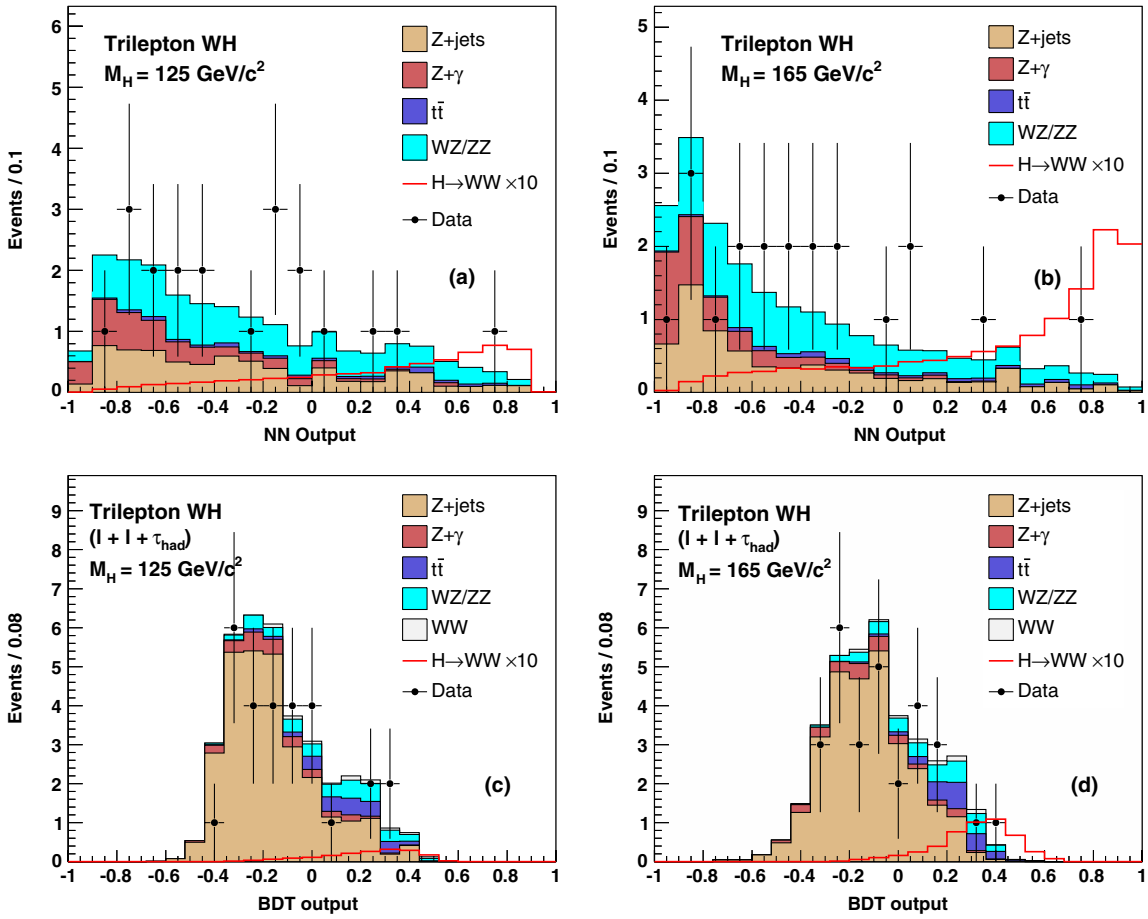

FIG. 16 (color online). Predicted and observed distributions of output variables from multivariate algorithms trained to separate potential Higgs boson events from background contributions in the (a),(b) Trilepton WH and (c),(d) Trilepton WH ($\ell + \ell + \tau_{\rm had}$) search samples for Higgs boson mass hypotheses of 125 and 165 GeV/c^2. The overlaid signal predictions correspond to the sum of two production modes (WH and ZH) and are multiplied by a factor of 10 for visibility. Normalizations for background event yields are those obtained from the final fit used to extract search limits.

from the neutral current exchange is restricted to the range $75 < m_{\ell^+\ell^-} < 105$ GeV/c^2. The calculated cross sections are 11.34 pb for WW production, 3.22 pb for WZ production, and 1.20 pb for ZZ production. We assign a 6% uncertainty based on the effects of different scale choices and the application of MSTW2008 PDF uncertainties on the calculations. For $t\bar{t}$ production we assign a cross section of 7.04 pb [121], based on a top-quark mass of 173.1 $\pm$ 1.2 GeV/c^2 and the MSTW2008NNLO PDF set, yielding an uncertainty of 7%. Similarly, for DY production we rely on a NLO cross section calculation [122], yielding a central value of 251.3 pb with 5% uncertainty. In the case of $Z\gamma$ production, simulated samples are generated using specific requirements on the minimum p_T of the photon and the minimum separation between the photon and the leptons originating from the decay of the Z boson. Because the production cross section depends significantly on these requirements, we use the cross section determined by the LO generator to normalize the event sample and assign a larger 10% uncertainty.

The uncertainty in the measured luminosity is $\pm$5.9%, of which 4.4% comes from detector acceptance and operation of the luminosity monitor and 4.0% comes from uncertainty on the inelastic $p\bar{p}$ cross section [123]. Electron and muon identification efficiencies are measured from trigger-unbiased final state leptons reconstructed in $Z \to \ell^+\ell^-$ decays collected with single-lepton triggers, and associated uncertainties originate from the limited statistical power of these samples. The lepton identification uncertainty applied to specific search samples depends on the required number of reconstructed leptons in each event. Tau lepton identification efficiencies are measured from the OS hadronic tau ($\mu + \tau_{\rm had}$, low$\not\!\!E_T$, low$\Delta\phi(\vec{p}_T(\ell), \vec{\not\!\!E}_T)$) control sample with associated uncertainty due to the limited sample size and subtraction of non-DY background contributions. Single-lepton trigger efficiencies are also measured from the trigger-unbiased final state lepton in $Z \to \ell^+\ell^-$ decays collected with single-lepton triggers, and uncertainties originate from the limited sample size.

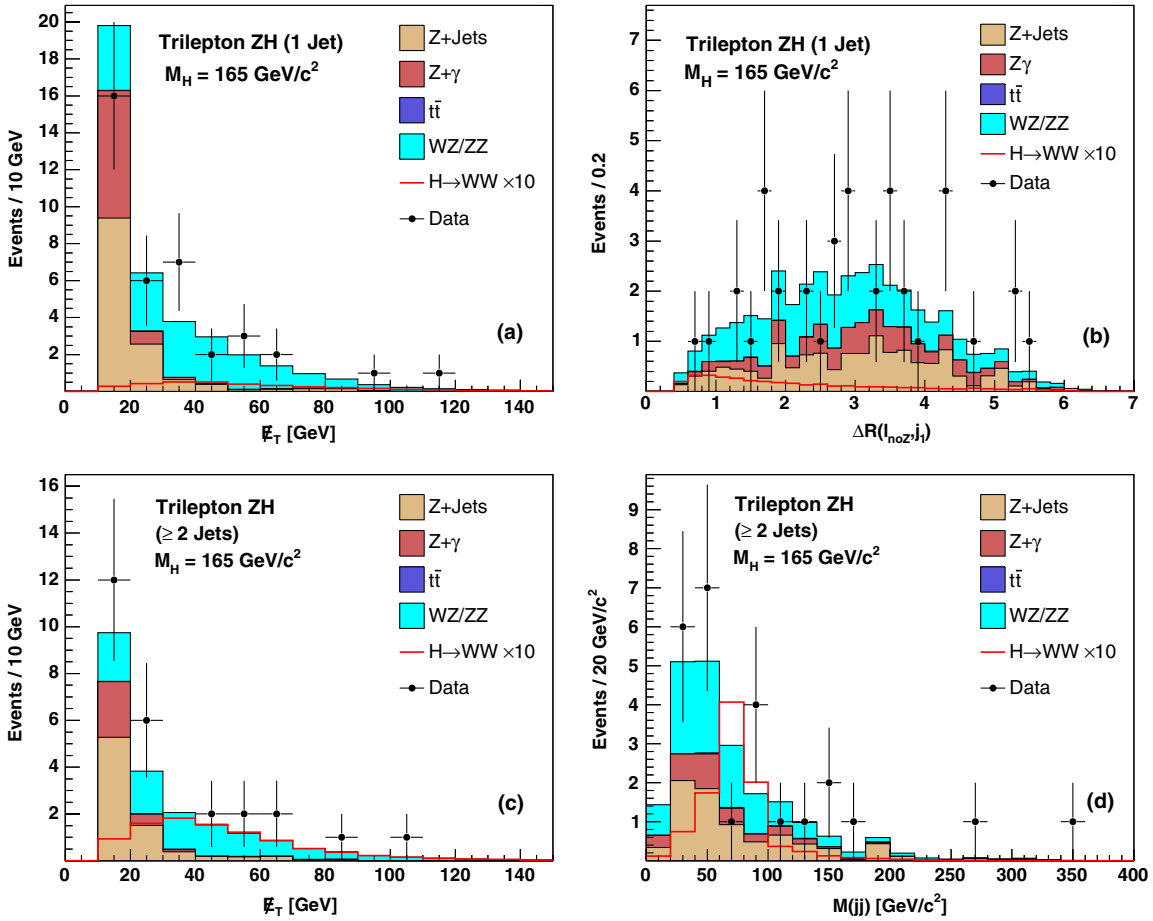

FIG. 17 (color online). Predicted and observed distributions of kinematic input variables providing the largest separation between potential signal and background contributions in the (a),(b) Trilepton ZH (1 jet) and (c),(d) Trilepton ZH (≥ 2 jets) search samples. The overlaid signal predictions correspond to the sum of two production modes (WH and ZH) for a Higgs boson with mass of 165 GeV$/c^2$ and are multiplied by a factor of 10 for visibility. Normalizations for background event yields are those obtained from the final fit used to extract search limits.

Acceptance uncertainties originate from approximations employed within the signal and background process generators and mismodeling in the detector simulation. To account for the potential acceptance effects of higher-order amplitudes not incorporated in event generators, additional rate uncertainties are included on the predicted event yields. For samples generated with PYTHIA, we assign an uncertainty of 10%, which is the observed acceptance difference obtained from WW event samples generated at LO with PYTHIA and at NLO using the MC@NLO [98] program. In the specific case of WW production, we use PYTHIA to model observed differences in the WW p_T spectrum, when applying harder and softer fragmentation scales in the parton-shower algorithms used for modeling higher-order effects. Events from the simulated MC@NLO WW event sample are reweighted as a function of WW p_T to match the changes in the spectra obtained from increasing or decreasing the size of the fragmentation scales, and uncertainties are assigned based on changes in acceptance resulting from these reweightings. Normalization of the simulated $W\gamma$ event samples is obtained from a control sample containing SS dileptons with invariant mass $M_{\ell\ell} < 16$ GeV$/c^2$. Because modeling of higher-order amplitudes can affect the extrapolation of this normalization to predicted $W\gamma$ event yields for the search samples containing dileptons with $M_{\ell\ell} > 16$ GeV$/c^2$, the 10% rate uncertainty is retained for these cases. Because the simulated $Z\gamma$ event sample is generated with an incomplete luminosity profile, we assign a slightly higher 15% uncertainty.

Event yields obtained from simulated event samples also have uncertainties associated with mismodelings in the detector simulation. We vary the energy scale of reconstructed jets in simulated events within an uncertainty range determined from p_T balancing studies performed on γ^*/Z plus one-jet events in data and simulation. The resulting differences in predicted event yields are taken as additional rate uncertainties. Since search samples are typically defined by the number of reconstructed jets within each event, changes to the jet energy scale can result in simulated events moving from one search sample to another. Hence, correlations and anticorrelations are included in the jet energy scale uncertainties applied across

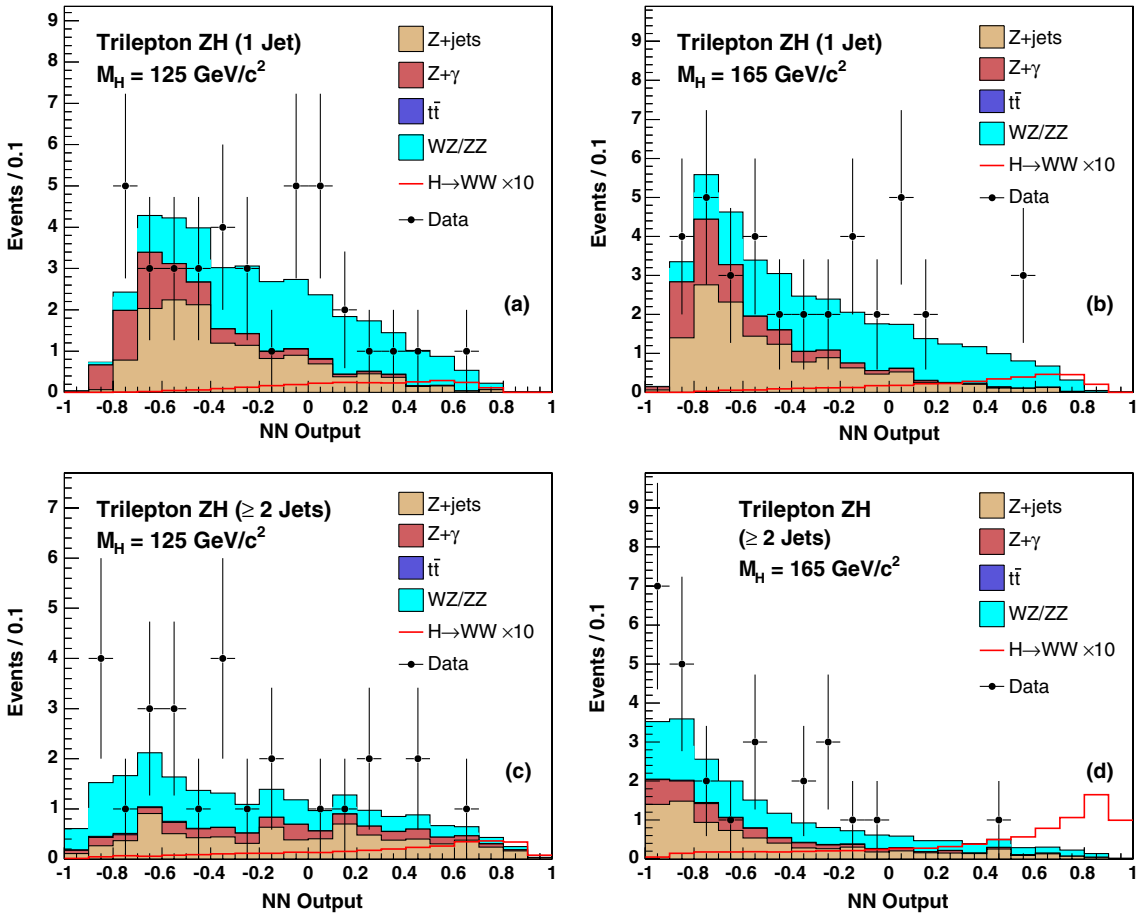

FIG. 18 (color online). Predicted and observed distributions of neural network output variables for networks trained to separate potential Higgs boson events from background contributions in the (a),(b) Trilepton ZH (1 jet) and (c),(d) Trilepton ZH (≥ 2 jets) search samples for Higgs boson mass hypotheses of 125 and 165 GeV/c^2. The overlaid signal predictions correspond to the sum of two production modes (WH and ZH) and are multiplied by a factor of 10 for visibility. Normalizations for background event yields are those obtained from the final fit used to extract search limits.

the different search samples. Modeling of lepton charge mismeasurement rates has a significant impact on predicted background event yields only in the SS (≥ 1 jets) search sample. Uncertainties are obtained from a comparison of the predicted and observed numbers of SS candidate events contained in an inclusive DY control sample.

Other uncertainties related to the detector simulation include modeling of the b-quark jet tagging algorithm used for vetoing events in the OS base (≥ 2 jets) search sample and modeling of isolated lepton candidates from b-quark decays in the trilepton search samples. These rate uncertainties apply only to background predictions for $t\bar{t}$ production, for which resulting events necessarily contain two b-quark jets. As discussed in Sec. VI, scale factors are applied to simulated events with jets identified as originating from bottom quarks to account for differences in tagging algorithm performance between data and Monte Carlo and the small subset of data events, for which silicon tracking detector information is not available. Uncertainties associated with these scale factors come primarily from the limited size of the data samples used to estimate them.

For simulated samples normalized to the observed event rate in a specific data control sample, we assign rate uncertainties based on the limited control-sample size and subtraction of residual background contributions. The scale factors applied to $W\gamma$ simulated event samples to account for uncertainties in photon-conversion modeling are obtained from the SS inverse $M_{\ell\ell}$ control sample. The normalization applied to simulated W + jet and Z + jet event samples, which are used for modeling contributions of these processes to the OS hadronic tau and Trilepton WH ($\ell + \ell + \tau_{\mathrm{had}}$) search samples, is obtained from the OS hadronic tau ($e + \tau_{\mathrm{had}}$, high $\Delta\phi(\vec{p}_T(\tau), \vec{p}_T(\ell))$) control sample. The construction of the PYTHIA sample tuned to model DY contributions in the OS base (0 jet) and OS base (1 jet) search samples is described in Sec. VI. The $\not\!\!E_T$ in each simulated event is shifted to account for effects of multiple interactions and the resulting sample is normalized to event counts in data obtained from the OS base (intermediate $\not\!\!E_T^{\mathrm{spec}}$) control sample. Uncertainties from $\not\!\!E_T$ modeling applied to the corresponding event yield predictions are obtained through additional ± 2 GeV shifts with

TABLE IX. Uncertainties on background process event yields for seven dilepton search samples formed from electron and muon candidates. The DY[1] column corresponds to uncertainties on the untuned Monte Carlo models of DY background contributions to the OS inverse $M_{\ell\ell}$, SS (≥ 1 jets), and OS base (≥ 2 jets) search samples. The DY[2] column corresponds to uncertainties on the tuned Monte Carlo model of DY background contributions to the OS base (0 jet) and OS base (1 jet) search samples.

Uncertainty source	WW	WZ	ZZ	$t\bar{t}$	DY[1]	DY[2]	$W\gamma$	W + jets
Theoretical cross section	6%	6%	6%	7%	5%			
Luminosity	5.9%	5.9%	5.9%	5.9%	5.9%			
Lepton (e or μ) identification efficiency	3.8%	3.8%	3.8%	3.8%	3.8%			
Trigger efficiency	2.0%	2.0%	2.0%	2.0%	2.0%			
Higher-order amplitudes	2.3%–17%	10%	10%	10%	10%		0–10%	
Jet energy scale	1.2%–21%	1.1%–13%	2.0%–13%	0.3%–28%	4.9%–33%	6.5%–18%	1.2–22%	
Lepton charge mismeasurement[a]	25%				25%			
b-quark jet veto modeling[b]				3.6%				
$\not{E}_T$ modeling						19%–21%		
Photon-conversion modeling							6.8%–8.4%	
Jet-to-lepton (e or μ) misreconstruction rate								14%–38%

[a]Uncertainty sources applied only in the SS (≥ 1 jets) search sample.
[b]Uncertainty sources applied only in the OS base (≥ 2 jets) search sample.

respect to the nominal $\not{E}_T$ correction and renormalization of the retuned event samples.

The data-driven procedure for modeling W + jet and Z + jet contributions to search samples that do not incorporate hadronically decaying tau lepton candidates is also described in Sec. VI. Jet-to-lepton misidentification rates are measured in inclusive jet samples collected using single-jet triggers and applied as weights to events containing both reconstructed leptons and jets. Differences in the measured jet misidentification rate from event samples collected with varied E_T thresholds are observed due to changes in the relative contributions of quark and gluon jets in these samples. Rate uncertainties on the predicted event yields are obtained by propagating these differences through the modeling procedure. For the search samples that incorporate hadronically decaying tau lepton candidates, lepton-to-tau and jet-to-tau misidentification rates are modeled within the event simulation and validated using data control samples. Assigned uncertainties are based on differences between predicted and observed event yields for these control samples.

In the context of a combined search, assumptions are needed on the relative sizes of the expected contributions originating from each production process. We incorporate full rate uncertainties on estimated event yields within the final fit. Rate uncertainties applied to estimated signal contributions from each production mode are summarized in Table XII. Here, uncertainty ranges cover variations across all 13 search samples, which depend on the same set of simulated samples for modeling potential signal. Contributions from ggH and VBF production are not considered in the SS (≥ 1 jets) and trilepton search samples.

Theoretical cross section calculations used to normalize simulated signal event samples and associated uncertainties are described in Sec. II. Uncertainties on ggH production are much larger for higher jet multiplicity search samples, and an algorithm is used to assign correlated rate uncertainties to each search sample. The inputs to this algorithm are the theoretical uncertainties associated with calculations of the inclusive, exclusive one-or-more parton, and exclusive two-or-more parton ggH production

TABLE X. Uncertainties on background process event yields for two dilepton search samples formed from one electron or muon candidate and one hadronically decaying tau lepton candidate.

Uncertainty source	WW	WZ	ZZ	$t\bar{t}$	DY	$W\gamma$	W + jets
Theoretical cross section	6%	6%	6%	7%	5%		
Luminosity	5.9%	5.9%	5.9%	5.9%	5.9%		
Lepton (e or μ) identification efficiency	2.8%	2.8%	2.8%	2.8%	2.8%		
Lepton (τ) identification efficiency	1.3%	1.3%	1.3%	2.0%	3.3%–3.5%		
Trigger efficiency	2.0%	2.0%	2.0%	2.0%	2.0%		
Higher-order amplitudes	10%	10%	10%	10%	10%	10%	
Lepton (e or μ) to lepton (τ) misreconstruction rate	0.1%–0.2%	0.1%–0.2%	0.1%–0.2%	0.1%–0.2%	2.1%–2.3%	1.2%–2.1%	
Photon-conversion modeling						6.8%	
V + jets control region normalization							12.1%
Jet-to-lepton (τ) misreconstruction rate	5.8%	5.8%	5.8%	4.4%–5.1%	0.1%–0.2%		8.8%

TABLE XI. Uncertainties on background process event yields for four trilepton search samples. The Z + jets[c] column corresponds to uncertainties on the tuned Monte Carlo model of Z + jets background contributions to the Trilepton WH ($\ell + \ell + \tau_{\text{had}}$) search sample. The Z + jets[d] column corresponds to uncertainties on the data-driven model of Z + jets background contributions to the remaining three trilepton search samples.

Uncertainty source	WZ	ZZ	$t\bar{t}$	$Z\gamma$	Z + jets[c]	Z + jets[d]
Theoretical cross section	6%	6%	7%	10%		
Luminosity	5.9%	5.9%	5.9%	5.9%		
Lepton (e or μ) identification efficiency	3.8%–5.0%	3.8%–5.0%	3.8%–5.0%	3.8%–5.0%		
Lepton (τ) identification efficiency[a]	2.1%	2.1%	1.1%	1.4%		
Trigger efficiency	2.0%	2.0%	2.0%	2.0%		
Higher-order amplitudes	10%	10%	10%	15%	10%	
Jet energy scale	0–18%	0–15%	0–2.3%	2.7%–17%		
Modeling of leptons from b-quark jets			22%–42%			
Lepton (e or μ) to lepton (τ) misreconstruction rate[a]	0.5%	0.5%	0.2%	0.7%	0.3%	
V + jets control region normalization					12.1%	
Jet-to-lepton (e or μ) misreconstruction rate						18%–24%
Jet-to-lepton (τ) misreconstruction rate[a]	4.5%	4.5%	5.1%	0.1%	6.5%	

[a]Uncertainty sources applied only in the Trilepton WH ($\ell + \ell + \tau_{\text{had}}$) search sample.

cross sections. The ggH theoretical cross section uncertainty range reported in Table XII is obtained from the quadrature sum of all contributions as applied within each of the 13 search samples. The other rate uncertainties applied to estimated signal event yields correspond directly to those applied to background predictions and are obtained following the same methodology.

Each source contributing to the rate uncertainties assigned to background and signal predictions can also affect the shapes of discriminant outputs associated with the corresponding processes. The effects of all uncertainty sources on discriminant distributions are studied and found to be mostly negligible. In the remaining cases shape uncertainties, which correspond to correlated but nonuniform bin-by-bin rate uncertainties applied across a single discriminant distribution, are incorporated. In particular, we account for the uncertainty originating from missing higher-order amplitudes to the modeled Higgs boson p_T spectrum on the shapes of the ggH discriminant outputs for each of the six OS dilepton search samples. Similarly, the effects of uncertainties from missing higher-order amplitudes to the modeled WW p_T spectrum on the shapes of WW discriminant outputs are also included. Figures 19(a) and 19(b) show resulting examples of the bin-by-bin scalings applied in individual search samples to generate alternative ggH and WW discriminant shapes.

The shapes of DY discriminant outputs are also found to be significantly altered by uncertainties associated with $\not\!\!E_T$ modeling in the four OS base (0 or 1 jet) search samples and by uncertainties associated with jet energy scale modeling in the OS base (≥ 2 jets) search sample. Figures 19(c) and 19(d) show examples of the bin-by-bin scalings applied in these search samples to generate the alternative DY discriminant shapes. For the SS (≥ 1 jets) search sample, uncertainties associated with jet energy scale modeling are determined to significantly affect the shapes of discriminant outputs associated with both signal (WH and ZH) and background (WW, WZ, and DY) contributions. Figures 19(e) and 19(f) show resulting examples of the bin-by-bin scalings used to generate alternative signal and background discriminant shapes.

TABLE XII. Uncertainties on signal process event yields for all search samples.

Uncertainty source	ggH	WH	ZH	VBF
Theoretical cross section	14%–44%	5%	5%	10%
Luminosity	5.9%	5.9%	5.9%	5.9%
Lepton (e or μ) identification efficiency	2.8%–3.8%	2.8%–5.0%	2.8%–5.0%	2.8%–3.8%
Lepton (τ) identification efficiency[a]	4.1%	1.4%–2.1%	1.6%–2.2%	4.0%
Trigger efficiency	2.0%	2.0%	2.0%	2.0%
Higher-order amplitudes	2.3%–13%	10%	10%	10%
Jet energy scale	0–15%	0–20%	0–7.8%	0–13%
Lepton (e or μ) to lepton (τ) misreconstruction rate[a]	0.1%	0.1%	0.1%	0.1%
Jet-to-lepton (τ) misreconstruction rate[a]		3.5–4.5%	2.9%–4.2%	0–0.4%

[a]Uncertainty sources applied only in the two OS hadronic tau and Trilepton WH ($\ell + \ell + \tau_{\text{had}}$) search samples.

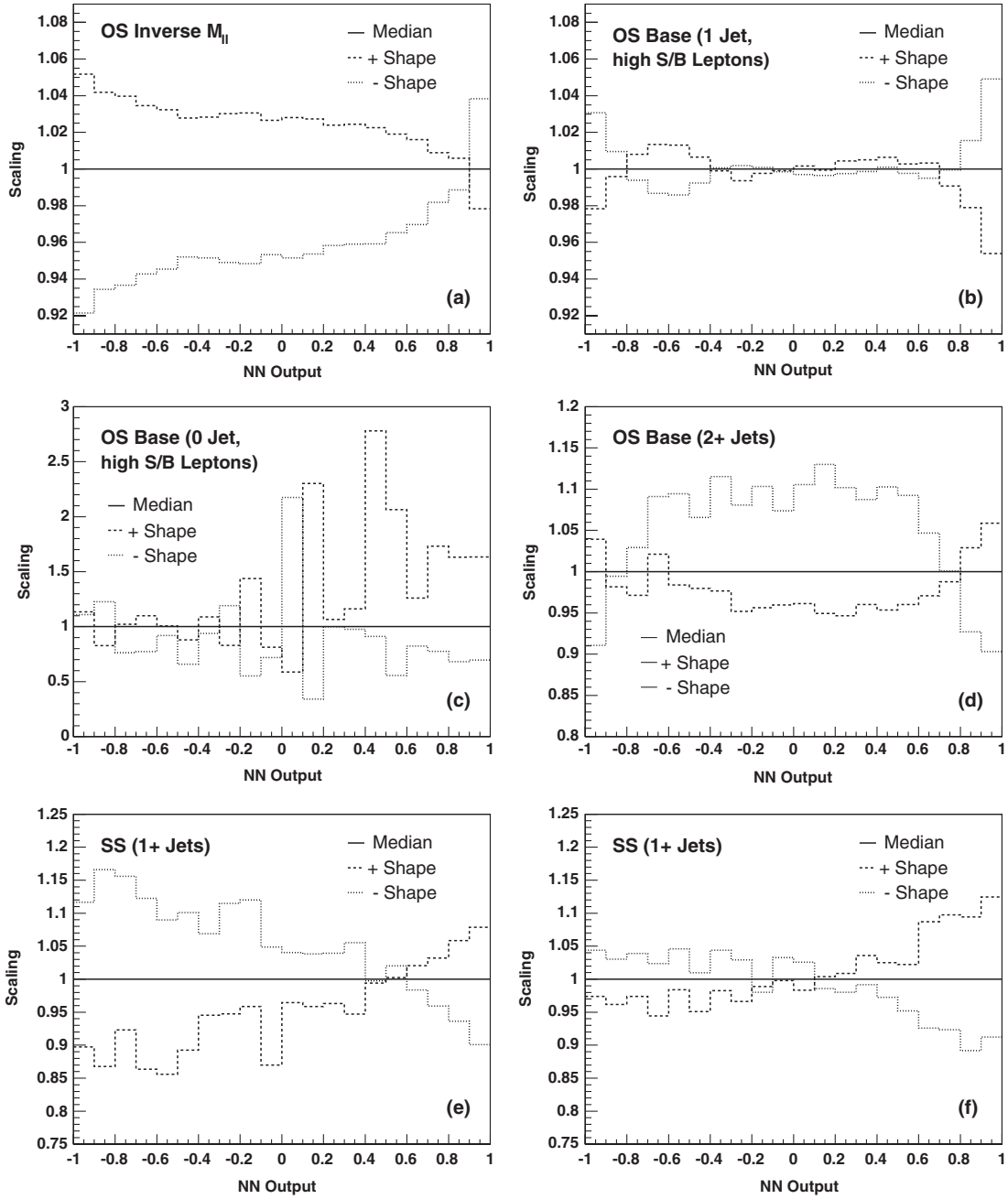

FIG. 19. Example bin-by-bin scalings used to obtain alternative neural network discriminant outputs associated with (a) higher-order diagrams uncertainty on the ggH contribution in the OS inverse $M_{\ell\ell}$ search sample, (b) higher-order diagrams uncertainty on the WW background contribution in the OS base (1 jet, high s/b leptons) search sample, (c) $\not\!\!E_T$ modeling uncertainty on the DY background contribution in the OS base (0 jet, high s/b leptons) search sample, (d) jet energy scale uncertainty on the DY contribution in the OS base (≥ 2 jets) search sample, (e) jet energy scale uncertainty on the WH contribution in the SS (≥ 1 jets) search sample, and (f) jet energy scale uncertainty on the WZ contribution in the SS (≥ 1 jets) search sample.

X. RESULTS

The primary goal is to test for the presence of signal events originating from Higgs boson production and decay. We adopt a Bayesian approach to estimate or bound the signal strength most consistent with the observed data. If the SM prediction of the signal strength for a specific value of m_H is larger than the observed 95% C.L. upper limit, that mass value is excluded at the 95% C.L. We quantify the search sensitivity using the median of the expected upper limit distribution as obtained in an ensemble of experiments simulated without signal.

The extraction of results is complicated by the presence of multiple signal production processes, each potentially contributing signal events with differing kinematic signatures. Combination of results from multiple search samples

is pursued to optimize the search sensitivity. The results are binned in their respective discriminant variables, and the data are assumed to be Poisson distributed in each bin. Predictions of expected signal and background rates within each bin of the discriminant distributions associated with the different search samples are affected by systematic uncertainties. Many of these systematic uncertainties are correlated across discriminant bins, between signal and background components, and between search samples. Uncertainty sources that result in events migrating between search samples need to be treated as anticorrelated with respect to those samples. To address these issues, we use the methodology described in Ref. [110] as summarized below.

The contents of low signal-to-background (s/b) bins serve to constrain the values of nuisance parameters, corresponding to each of the individual sources of systematic uncertainty on signal and background modeling. The same sources of systematic uncertainty affect predictions for signal and background yields in the high-s/b bins, which are more sensitive to the presence of a Higgs boson signal and its production rate.

We group the systematic uncertainties in three classes, according to their impact on the interpretation of results. The first class includes systematic effects affecting the event rates, which uniformly scale the predicted yields in each bin of the modeled discriminants. A second category corresponds to uncertainties affecting the shapes of the discriminants' distributions, which are also parametrized using common nuisance parameters and therefore applied as correlated across all bins within a modeled discriminant. In this case, bin-to-bin scalings are not required to be uniform, allowing for distortions in the shape of the distribution of the discriminant. A final category is for bin-by-bin independent uncertainties, which arise from the limited size of simulated and experimental data samples. Uncertainties associated with the last two categories reduce the constraining power of low-s/b bins on nuisance parameters.

The likelihood function, $L(\text{data}|s, b, \vec{\nu})$, is the same as that used in Ref. [110], with $\vec{\nu}$ representing the nuisance parameters. Shape uncertainties are applied first in an additive fashion, interpolating and extrapolating the contents in each bin according to the value of the nuisance parameter governing the shape distortion and the difference between the central and alternative shapes of the modeled discriminant. The prior probability densities assumed for the systematic uncertainties are Gaussian, and bin contents are constrained to be positive in this procedure. Bin-by-bin uncertainties are then applied to the signal and background predictions as Gaussians that are again truncated to prevent negative values of predictions. Finally, rate uncertainties are applied multiplicatively, scaling all discriminant bins by the same factor. Gaussian prior densities are also used for rate uncertainties with constraints to avoid negative scale factors. Asymmetric rate and shape uncertainties are parametrized as in Ref. [110]. Correlations in the predictions for different signal and background processes are accounted for by applying effects of shared uncertainty sources consistently across the modeled discriminants for each search sample. Because of the requirement for combining the results from several different search samples, a single parameter R is used to scale all signal contributions.

We integrate the likelihood function multiplied by the product of the prior densities for the nuisance parameters, over the nuisance parameters

$$L'(\text{data}|Rs, b) = \int L(\text{data}|Rs, b, \vec{\nu})\pi(\vec{\nu})d\vec{\nu}, \qquad (4)$$

where $\pi(\vec{\nu})d\vec{\nu}$ is the joint prior probability density for all of the nuisance parameters as described in Ref. [124]. In this case the joint prior density is the product of individual prior densities as systematic uncertainty sources are treated as uncorrelated.

As described in Ref. [124], a limit on R is obtained from

$$0.95 = \frac{\int_0^{R_{\text{limit}}} L'(\text{data}|Rs, b)\pi(R)}{\int_0^{\infty} L'(\text{data}|Rs, b)\pi(R)}, \qquad (5)$$

where $\pi(R)$ is a uniform prior density over all positive values of R. The value of R that maximizes $L'(\text{data}|Rs, b)$ is defined as the best-fit value. The interval for quoting 1 standard deviation uncertainties is given by the shortest interval $[R_{\text{low}}, R_{\text{high}}]$ satisfying

$$0.68 = \frac{\int_{R_{\text{low}}}^{R_{\text{high}}} L'(\text{data}|Rs, b)\pi(R)}{\int_0^{\infty} L'(\text{data}|Rs, b)\pi(R)}. \qquad (6)$$

Search sensitivity is estimated by generating multiple simulated test experiments according to background-only predictions and determining the observed limits for each trial. Values of nuisance parameters are separately varied according to their prior densities for each simulated experiment. The median observed limit, $R_{\text{limit}}^{\text{med}}$, is used as a gauge of analysis sensitivity. The distribution of possible limits expected in the absence of a signal is quantified by the $\pm 1\sigma$ and $\pm 2\sigma$ ranges centered on the median. Specifically, values of R, for which 2.3%, 16%, 50%, 84%, and 97.7% of background-only pseudoexperiments result in observed limits below that value, are reported.

A. Diboson cross section measurements

Measurements of diboson production cross sections using the same tools and techniques applied within the Higgs boson search provide an important validation of the analysis framework. A measurement of the $p\bar{p} \to W^+W^-$ cross section based on the $\ell^+\bar{\nu}\ell^-\nu$ decay mode was obtained from the OS base (0 jet, high s/b leptons) search sample using 3.6 fb^{-1} of integrated luminosity [125]. A value of $\sigma(p\bar{p} \to W^+W^- + X) = 12.1 \pm 1.8$ pb, which is in good

TABLE XIII. Median expected 95% C.L. upper limits assuming the background-only hypothesis, and corresponding observed limits on Higgs boson production relative to SM expectations for the $m_H = 125$ and 165 GeV/c^2 mass hypotheses obtained from combinations of search samples with analogous final states and the combination of all search samples.

	$m_H = 125$ GeV/c^2		$m_H = 165$ GeV/c^2	
Search sample(s)	Obs/$\sigma_{\rm SM}$	Exp/$\sigma_{\rm SM}$	Obs/$\sigma_{\rm SM}$	Exp/$\sigma_{\rm SM}$
OS base (0 jet)	4.76	7.30	1.36	1.41
OS base (1 jet)	9.86	9.76	1.45	1.85
OS base (≥ 2 jets)	18.1	7.34	2.83	1.95
OS inverse $M_{\ell\ell}$	11.9	11.0	1.71	2.76
SS (≥ 1 jets)	13.9	11.7	4.20	3.95
Trilepton WH	12.1	12.2	4.79	4.36
Trilepton ZH	19.9	23.2	4.94	6.59
OS hadronic tau			15.7	11.7
All samples	3.26	3.25	0.493	0.701

agreement with the NLO prediction, was obtained using the same matrix-element based discriminants employed within the Higgs boson search. Similarly, a measurement of the $p\bar{p} \to ZZ$ cross section based on the $\ell^+\ell^-\nu\bar{\nu}$ decay mode was obtained from the OS base (0 and 1 jet) search samples using 6.0 fb^{-1} of integrated luminosity [126]. Neural network based discriminants were used to extract a value of $\sigma(p\bar{p} \to ZZ + X) = 1.34 \pm 0.56$ pb, which is in good agreement with the NLO zero-width calculation, to which the result was normalized. Finally, a measurement of the $p\bar{p} \to W^{\pm}Z$ cross section based on the $\ell^{\pm}\nu\ell^+\ell^-$ decay mode was obtained from the Trilepton WH search sample using 7.1 fb^{-1} of integrated luminosity [127]. Neural network discriminants were again used to extract a value of $\sigma(p\bar{p} \to W^{\pm}Z + X) = 3.93 \pm 0.84$ pb, in good agreement with the NLO prediction.

B. SM Higgs boson interpretation

We determine limits on SM Higgs boson production for the combination of all search samples and for groups of samples with analogous final states. The limit calculations are performed separately for each of the 19 Higgs boson mass hypotheses considered. Because we account for potential contributions from all four Higgs boson production modes, the resulting limits are determined as ratios with respect to SM expectations. Based on the (N)NLO Higgs boson production cross sections and decay branching ratios for $H \to W^+W^-$ presented in Sec. II, the largest potential signal contributions would originate from a Higgs boson with a mass of 165 GeV/c^2, and the best combined search sensitivity is indeed obtained for this mass hypothesis. The actual sensitivity of an individual search sample under a specific mass hypothesis depends both on the signal-to-background ratio of events in the sample and the ability of the neural network to separate background contributions from the potential signal contributions associated with the hypothesized Higgs boson mass.

The OS base (0 jet) search samples have the highest sensitivity to SM Higgs boson production. The dominant signal contributions originate from ggH production. Similar sensitivity is obtained from the OS base (1 jet) and OS base (≥ 2 jets) samples, where additional signal contributions from VH and VBF production have a more significant impact. The OS inverse $M_{\ell\ell}$ search sample, with dominant signal contributions from ggH production, is approximately 50% less sensitive than the OS base samples for the $m_H = 165$ GeV/c^2 hypothesis. But for the $m_H = 125$ GeV/c^2 hypothesis the sensitivities are comparable since a higher fraction of potential signal events satisfy the kinematic criteria of this sample. The SS (≥ 1 jets), Trilepton WH, and Trilepton ZH search samples, which focus exclusively on VH production, contribute sensitivities that are 20%–50% of those obtained from the best OS base samples. In addition to the non-negligible gain in combined search sensitivity that results from their inclusion, these samples are also unique in that both the production and decay mechanisms associated with potential Higgs boson events depend on vector boson couplings and are therefore useful for placing constraints on these couplings [128,129]. Because they contain much larger background contributions, the OS hadronic tau search samples contribute significantly less to the combined search sensitivity. Since the neural networks

TABLE XIV. Median expected 95% C.L. upper limits assuming the background-only hypothesis, and corresponding observed limits on Higgs boson production relative to SM expectations from the combination of all search samples for 19 mass hypotheses within the range $110 < m_H < 200$ GeV/c^2. The boundaries of the 1 and 2 standard deviations assuming the background-only hypothesis are also provided.

m_H	110	115	120	125	130	135	140	145	150	155	160	165	170	175	180	185	190	195	200
$-2\sigma/\sigma_{\rm SM}$	7.11	3.78	2.47	1.67	1.25	1.04	0.84	0.73	0.64	0.54	0.41	0.37	0.43	0.53	0.66	0.80	0.98	1.21	1.23
$-1\sigma/\sigma_{\rm SM}$	9.60	5.25	3.25	2.32	1.70	1.37	1.13	0.98	0.85	0.71	0.53	0.50	0.58	0.71	0.87	1.08	1.34	1.54	1.74
Exp/$\sigma_{\rm SM}$	13.4	7.41	4.51	3.25	2.33	1.89	1.60	1.37	1.16	0.98	0.74	0.70	0.83	1.00	1.18	1.51	1.88	2.12	2.48
$+1\sigma/\sigma_{\rm SM}$	18.8	10.4	6.36	4.52	3.20	2.62	2.28	1.91	1.60	1.38	1.04	0.99	1.18	1.39	1.63	2.15	2.63	3.01	3.49
$+2\sigma/\sigma_{\rm SM}$	26.0	14.3	8.90	6.19	4.34	3.60	3.22	2.62	2.19	1.94	1.45	1.37	1.66	1.92	2.23	3.01	3.62	4.26	4.81
Obs/$\sigma_{\rm SM}$	14.1	9.49	5.26	3.26	2.66	2.01	2.02	1.25	0.95	0.74	0.60	0.49	0.84	1.28	1.50	2.53	3.47	4.64	5.65

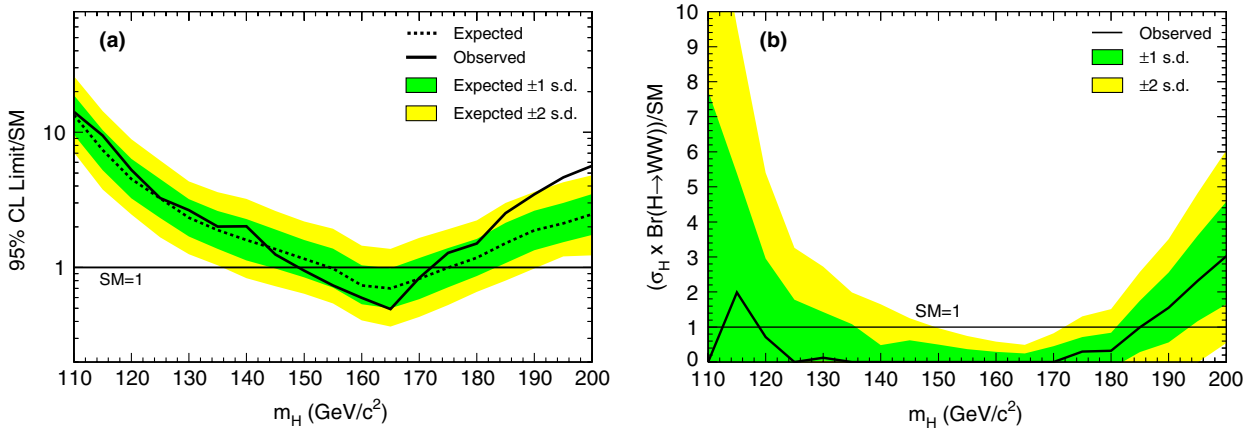

FIG. 20 (color online). (a) Median expected, assuming the background-only hypothesis, (dashed line) and observed (solid line) 95% C.L. upper limits on Higgs boson production relative to SM expectations from the combination of all search samples as a function of the Higgs boson mass. The dark and light shaded bands show the 1 and 2 standard deviations assuming the background-only hypothesis. (b) Best-fit cross section for inclusive Higgs boson production, normalized to the SM expectation, for the combination of all search samples as a function of the Higgs boson mass. The solid line indicates the fitted cross section, and the associated dark and light shaded regions show the 68% and 95% credibility intervals.

are unable to separate background and signal contributions in these samples for low Higgs boson masses, these samples are incorporated into combined limits only for mass hypotheses of 130 GeV$/c^2$ and above.

Table XIII presents limits on Higgs boson production obtained from combinations of search samples with analogous final states and from the combination of all search samples. Median expected 95% C.L. upper limits assuming the background-only hypothesis, and corresponding observed limits on Higgs boson production relative to SM expectations are shown for the 125 and 165 GeV$/c^2$ mass hypotheses. Limits obtained from the combination of all search samples for 19 Higgs boson mass hypotheses within the range $110 < m_H < 200$ GeV$/c^2$ are presented in Table XIV along with boundaries on the 1 and 2 standard deviations assuming the background-only hypothesis. These limits are also presented graphically in Fig. 20(a). SM Higgs boson mass values are excluded at the 95% C.L. in the range over which the observed limits lie below one (the expected SM production rate). The data excludes Higgs boson masses in the range $149 < m_H < 172$ GeV$/c^2$, where the median expected exclusion range, assuming the background-only hypothesis, is $155 < m_H < 175$ GeV$/c^2$.

We also fit for the Higgs boson production rate most compatible with the observed data. Best-fit cross sections normalized to SM expectations are displayed as a function of the Higgs boson mass in Fig. 20(b). In the cross section

TABLE XV. Median expected 95% C.L. upper limits assuming the background-only hypothesis, and corresponding observed limits on $\sigma(ggH) \times \mathcal{B}(H \to W^+W^-)$ in picobarns (pb) from the combination of all search samples for 29 mass hypotheses within the range $110 < m_H < 300$ GeV$/c^2$. The boundaries of 1 and 2 standard deviations assuming the background-only hypothesis are also provided. The WH, ZH, and VBF Higgs boson production mechanisms are assumed to contribute no events to the search samples.

m_H	110	115	120	125	130	135	140	145	150	155	160	165	170	175	180
-2σ	0.70	0.53	0.52	0.46	0.45	0.43	0.39	0.37	0.32	0.28	0.21	0.18	0.21	0.21	0.23
-1σ	0.95	0.77	0.70	0.65	0.61	0.58	0.52	0.51	0.44	0.38	0.28	0.24	0.27	0.29	0.31
Exp.	1.32	1.09	0.97	0.92	0.85	0.81	0.74	0.71	0.62	0.52	0.38	0.33	0.37	0.40	0.44
$+1\sigma$	1.84	1.47	1.36	1.29	1.19	1.14	1.05	1.00	0.86	0.72	0.52	0.46	0.51	0.56	0.61
$+2\sigma$	2.54	1.94	1.86	1.78	1.64	1.59	1.48	1.38	1.17	0.99	0.72	0.64	0.71	0.77	0.85
Obs.	1.42	1.18	1.04	0.97	0.82	0.69	0.71	0.67	0.41	0.33	0.26	0.28	0.33	0.46	0.54
m_H	180	185	190	195	200	210	220	230	240	250	260	270	280	290	300
-2σ	0.23	0.25	0.27	0.28	0.32	0.32	0.32	0.33	0.35	0.30	0.29	0.27	0.25	0.25	0.22
-1σ	0.31	0.34	0.36	0.39	0.42	0.42	0.44	0.45	0.47	0.41	0.39	0.37	0.33	0.33	0.29
Exp.	0.44	0.47	0.50	0.55	0.58	0.59	0.60	0.62	0.65	0.56	0.53	0.51	0.46	0.46	0.40
$+1\sigma$	0.61	0.65	0.69	0.77	0.80	0.84	0.83	0.86	0.91	0.79	0.74	0.70	0.64	0.65	0.57
$+2\sigma$	0.85	0.90	0.94	1.05	1.10	1.19	1.12	1.19	1.25	1.10	1.01	0.95	0.89	0.91	0.80
Obs.	0.54	0.66	0.81	1.01	1.01	1.38	1.10	1.14	1.34	1.19	0.97	0.95	0.92	1.01	0.81

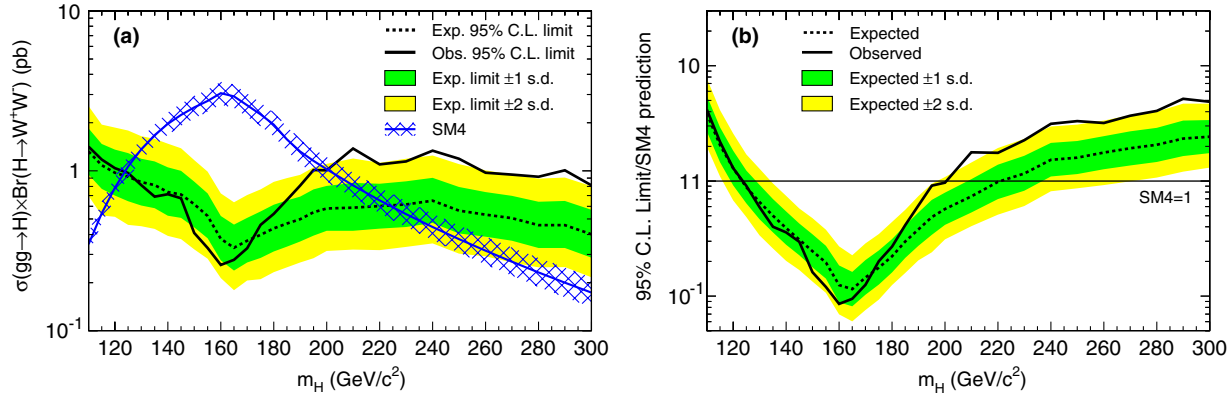

FIG. 21 (color online). Median expected 95% C.L. upper limits assuming the background-only hypothesis (dashed line), and corresponding observed limits (solid line) on (a) $\sigma(ggH) \times \mathcal{B}(H \to W^+W^-)$ in picobarns (pb) and (b) Higgs boson production relative to SM4 expectations from the combination of all search samples as a function of the Higgs boson mass. The dark and light shaded bands show the 1 and 2 standard deviations assuming the background-only hypothesis. In the (a) panel, the lighter colored line indicates the SM4 expectation and the hatched region encompasses the associated theoretical uncertainties.

fit, the SM ratios for the relative rates of the four contributing production mechanisms are assumed. Over a significant fraction of the tested mass range, the fit to the data indicates little or no contribution associated with Higgs boson production. For the $m_H = 125$ GeV$/c^2$ mass hypothesis, the fitted Higgs boson production rate relative to the SM expectation is $0.00^{+1.78}_{-0.00}$, which is compatible at the level of 1 standard deviation with both the SM Higgs boson and the background-only expectations.

C. Limits on ggH production and Higgs boson constraints in SM4

Because Higgs boson ggH production proceeds at lowest order via a virtual loop containing strongly interacting particles, the production rate from this mechanism is sensitive to the existence of particles that may be too massive for direct observation. The presence of a fourth generation of heavy fermions beyond the three families described in the SM enhances the ggH production cross section by a factor between seven and nine in the range of m_H accessible at the Tevatron. The presence of a fourth fermion generation affects ggH production only, and neither enhances nor suppresses WH, ZH, and VBF production.

In order to interpret the search in terms of the SM4 and other extensions to the SM that would affect the ggH production rate, we first extract upper bounds on the ggH production cross section times decay branching ratio $H \to W^+W^-$ assuming negligible contributions from WH, ZH, and VBF production. This assumption ensures that resulting limits are the most conservative with respect to possible enhancements or suppressions of the other

TABLE XVI. Median expected 95% C.L. upper limits assuming the background-only hypothesis, and corresponding observed limits on Higgs boson production relative to SM4 expectations from the combination of all search samples for 29 mass hypotheses within the range $110 < m_H < 300$ GeV$/c^2$. The boundaries of 1 and 2 standard deviations assuming the background-only hypothesis are also provided. The WH, ZH, and VBF Higgs boson production mechanisms are assumed to contribute no events to the search samples.

m_H	110	115	120	125	130	135	140	145	150	155	160	165	170	175	180
$-2\sigma/\sigma_{\mathrm{SM4}}$	1.98	1.09	0.66	0.45	0.33	0.25	0.20	0.17	0.13	0.10	0.07	0.06	0.08	0.09	0.12
$-1\sigma/\sigma_{\mathrm{SM4}}$	2.69	1.46	0.91	0.62	0.45	0.34	0.27	0.22	0.18	0.14	0.09	0.08	0.10	0.13	0.16
$\mathrm{Exp}/\sigma_{\mathrm{SM4}}$	3.83	2.05	1.29	0.87	0.62	0.47	0.38	0.31	0.25	0.19	0.12	0.11	0.14	0.18	0.22
$+1\sigma/\sigma_{\mathrm{SM4}}$	5.49	2.92	1.80	1.22	0.87	0.67	0.53	0.43	0.34	0.27	0.17	0.16	0.20	0.25	0.31
$+2\sigma/\sigma_{\mathrm{SM4}}$	7.77	4.13	2.49	1.69	1.20	0.92	0.73	0.59	0.46	0.37	0.24	0.23	0.28	0.35	0.43
$\mathrm{Obs}/\sigma_{\mathrm{SM4}}$	4.17	2.19	1.29	0.91	0.59	0.39	0.35	0.28	0.16	0.12	0.09	0.10	0.13	0.20	0.27
m_H	180	185	190	195	200	210	220	230	240	250	260	270	280	290	300
$-2\sigma/\sigma_{\mathrm{SM4}}$	0.12	0.16	0.19	0.23	0.29	0.36	0.44	0.53	0.64	0.62	0.71	0.74	0.78	0.83	0.88
$-1\sigma/\sigma_{\mathrm{SM4}}$	0.16	0.21	0.26	0.32	0.39	0.49	0.59	0.70	0.86	0.86	0.93	0.99	1.03	1.11	1.15
$\mathrm{Exp}/\sigma_{\mathrm{SM4}}$	0.22	0.29	0.36	0.45	0.53	0.69	0.82	0.97	1.20	1.22	1.27	1.37	1.43	1.54	1.61
$+1\sigma/\sigma_{\mathrm{SM4}}$	0.31	0.41	0.51	0.64	0.75	0.97	1.15	1.38	1.66	1.73	1.75	1.92	2.03	2.17	2.27
$+2\sigma/\sigma_{\mathrm{SM4}}$	0.43	0.58	0.70	0.90	1.03	1.34	1.60	1.94	2.28	2.42	2.41	2.64	2.87	3.02	3.17
$\mathrm{Obs}/\sigma_{\mathrm{SM4}}$	0.27	0.38	0.56	0.81	0.78	1.43	1.29	1.58	2.10	2.07	1.83	2.06	2.18	2.67	2.37

TABLE XVII. Median expected 95% C.L. upper limits assuming the background-only hypothesis, and corresponding observed limits on fermiophobic Higgs boson production relative to FHM model expectations from the combination of all relevant search samples for 19 mass hypotheses within the range $110 < m_H < 200$ GeV/c^2. The boundaries of the 1 and 2 standard deviations bands assuming the background-only hypothesis are also provided.

m_H	110	115	120	125	130	135	140	145	150	155	160	165	170	175	180	185	190	195	200
$-2\sigma/\sigma_{\mathrm{FHM}}$	0.59	0.61	0.63	0.65	0.74	0.77	0.83	0.86	0.89	0.88	0.89	0.83	0.92	1.03	1.17	1.45	1.76	1.92	2.04
$-1\sigma/\sigma_{\mathrm{FHM}}$	0.78	0.85	0.86	0.88	0.98	1.03	1.09	1.14	1.20	1.17	1.11	1.08	1.21	1.37	1.58	1.95	2.33	2.53	2.79
$\mathrm{Exp}/\sigma_{\mathrm{FHM}}$	1.08	1.18	1.21	1.24	1.35	1.41	1.51	1.60	1.64	1.61	1.50	1.50	1.69	1.95	2.21	2.72	3.24	3.51	3.90
$+1\sigma/\sigma_{\mathrm{FHM}}$	1.53	1.63	1.69	1.76	1.89	1.95	2.12	2.27	2.25	2.25	2.12	2.13	2.38	2.80	3.10	3.83	4.57	4.96	5.45
$+2\sigma/\sigma_{\mathrm{FHM}}$	2.13	2.22	2.33	2.47	2.61	2.67	2.95	3.19	3.04	3.10	2.99	2.99	3.33	4.00	4.30	5.32	6.39	6.95	7.51
$\mathrm{Obs}/\sigma_{\mathrm{FHM}}$	1.45	2.25	1.90	1.89	1.51	1.85	2.28	1.98	1.95	1.60	1.58	1.28	1.99	2.45	3.05	3.94	4.40	5.48	6.63

production mechanisms within the context of a particular new physics model. Because we are focusing on enhancements in the production, which could lie significantly above SM expectations, we extend the search mass range to 300 GeV/c^2.

Since we are in this case setting limits on the rate of a specific Higgs boson production and decay mode, no theoretical rate uncertainties are incorporated. However, because we analyze opposite-sign dilepton events with zero, one, and two or more reconstructed jets in different search samples, the uncertainties on the relative fractions of Higgs boson signal events within these samples are retained. Median expected 95% C.L. upper limits assuming the background-only hypothesis, and corresponding observed limits on $\sigma(ggH) \times \mathcal{B}(H \to W^+W^-)$ are listed in Table XV along with the boundaries of 1 and 2 standard deviations assuming the background-only hypothesis.

A comparison between observed upper limits on $\sigma(ggH) \times \mathcal{B}(H \to W^+W^-)$ and SM4 expectations based on the production cross sections and decay branching ratios listed in Table I as a function of m_H is shown in Fig. 21(a). To extract SM4 model constraints, rate uncertainties associated with the theoretical cross sections and branching ratios are included within the limit calculation. The resulting median expected 95% C.L. upper limits assuming the background-only hypothesis, and corresponding observed limits on Higgs boson production relative to SM4 expectations are shown in Table XVI. The same limits are shown graphically in Fig. 21(b). Within the SM4 model we exclude Higgs boson masses in the range $124 < m_H < 200$ GeV/c^2, to be compared against a median expected exclusion range of $124 < m_H < 221$ GeV/c^2.

D. Higgs boson constraints in FHM model

Within the FHM model described in Sec. II, the allowed fermiophobic Higgs boson, H_f, production mechanisms are WH_f, ZH_f, and VBF. Contributions from the dominant SM gluon-fusion production mechanism, ggH_f, are negligibly small. Despite a smaller overall production rate, potential signal contributions of a fermiophobic Higgs boson are actually larger for lower Higgs boson masses due to increases in the branching ratio, $\mathcal{B}(H_f \to W^+W^-)$, relative to the SM.

We extract FHM model constraints from the SS (≥ 1 jets) and trilepton search samples, for which the potential signal contributions originate solely from WH_f and ZH_f production. Potential WH_f, ZH_f, and VBF signal contributions to the OS base search samples are also incorporated. In the specific case of the OS base (≥ 2 jets) sample, the discriminant output used is that from the neural network trained to distinguish signal events originating from the production mechanisms relevant to the FHM model. From the combination of these search samples, we determine 95% C.L. upper bounds on the fermiophobic Higgs boson production rate normalized to FHM model expectations using the SM theoretical cross section predictions for WH, ZH, and VBF production and branching ratios as predicted by the FHM model for $H_f \to W^+W^-$ listed in Table I. Median expected 95% C.L. upper limits assuming the background-only hypothesis, and

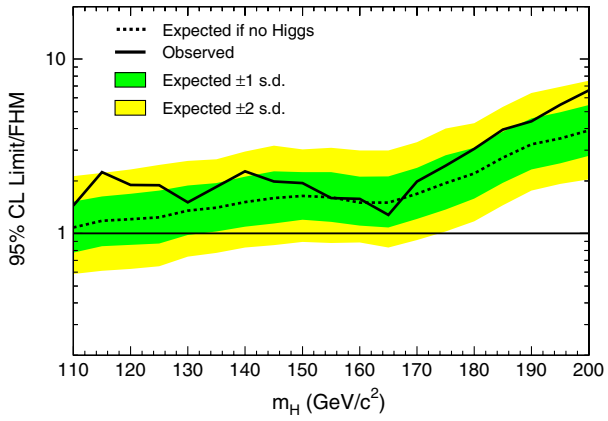

FIG. 22 (color online). Median expected 95% C.L. upper limits assuming the background-only hypothesis (dashed line), and corresponding observed limits (solid line) on fermiophobic Higgs boson production relative to FHM model expectations from the combination of all relevant search samples as a function of the Higgs boson mass. The dark and light shaded bands correspond to 1 and 2 standard deviations assuming the background-only hypothesis.

corresponding observed limits on fermiophobic Higgs boson production relative to FHM model expectations are listed in Table XVII and presented graphically in Fig. 22.

XI. CONCLUSION

We present the results of CDF searches for the Higgs boson focusing on the $H \to W^+W^-$ decay mode. The searches are based on the final CDF II data set corresponding to an integrated luminosity of 9.7 fb^{-1}. In the context of the SM, we exclude at the 95% C.L. Higgs bosons with masses in the range $149 < m_H < 172$ GeV$/c^2$. The expected exclusion range, in the absence of a signal, is $155 < m_H < 175$ GeV$/c^2$. In the case of a SM-like Higgs boson in the presence of a fourth generation of fermions with the lowest lepton and neutrino masses allowed by current experimental constraints, we exclude the range $124 < m_H < 200$ GeV$/c^2$ at the 95% C.L., where the expected exclusion region is $124 < m_H < 221$ GeV$/c^2$. Upper limits on fermiophobic Higgs boson production are also presented.

ACKNOWLEDGMENTS

We thank the Fermilab staff and the technical staffs of the participating institutions for their vital contributions. This work was supported by the U.S. Department of Energy and National Science Foundation; the Italian Istituto Nazionale di Fisica Nucleare; the Ministry of Education, Culture, Sports, Science and Technology of Japan; the Natural Sciences and Engineering Research Council of Canada; the National Science Council of the Republic of China; the Swiss National Science Foundation; the A.P. Sloan Foundation; the Bundesministerium für Bildung und Forschung, Germany; the Korean World Class University Program, the National Research Foundation of Korea; the Science and Technology Facilities Council and the Royal Society, U.K.; the Russian Foundation for Basic Research; the Ministerio de Ciencia e Innovación, and Programa Consolider-Ingenio 2010, Spain; the Slovak R&D Agency; the Academy of Finland; the Australian Research Council (ARC); and the EU community Marie Curie Fellowship Contract No. 302103.

[1] S. L. Glashow, Nucl. Phys. **22**, 579 (1961).
[2] S. Weinberg, Phys. Rev. Lett. **19**, 1264 (1967).
[3] A. Salam, in *Elementary Particle Theory: Proceedings of the Eighth Nobel Symposium* (Almqvist and Wiksell, Stockholm, 1969).
[4] F. Englert and R. Brout, Phys. Rev. Lett. **13**, 321 (1964).
[5] P. W. Higgs, Phys. Rev. Lett. **13**, 508 (1964).
[6] P. W. Higgs, Phys. Lett. **12**, 132 (1964).
[7] G. S. Guralnik, C. R. Hagen, and T. B. W. Kibble, Phys. Rev. Lett. **13**, 585 (1964).
[8] G. Aad *et al.* (ATLAS Collaboration), Phys. Lett. B **716**, 1 (2012).
[9] S. Chatrchyan *et al.* (CMS Collaboration), Phys. Lett. B **716**, 30 (2012).
[10] T. Aaltonen *et al.* (CDF and D0 Collaborations), arXiv:1204.0042.
[11] T. Aaltonen *et al.* (CDF and D0 Collaborations), Phys. Rev. D **86**, 092003 (2012).
[12] The ALEPH, CDF, D0, DELPHI, L3, OPAL, and SLD Collaborations, the LEP Electroweak Working Group, the Tevatron Electroweak Working Group, and the SLD Electroweak and Heavy Flavour Groups, arXiv:1012.2367v2; The most recent values from March 2012, as quoted, are available from http://lepewwg.web.cern.ch/LEPEWWG/.
[13] G. Abbiendi *et al.* (ALEPH, DELPHI, L3 and OPAL Collaborations and LEP Working Group for Higgs Boson Searches), Phys. Lett. B **565**, 61 (2003).
[14] G. Aad *et al.* (ATLAS Collaboration), arXiv:1307.1427.
[15] S. Chatrchyan *et al.* (CMS Collaboration), Eur. Phys. J. C **73**, 2469 (2013).
[16] A. Djouadi, J. Kalinowski, and M. Spira, Comput. Phys. Commun. **108**, 56 (1998).
[17] J. F. Gunion, H. E. Haber, G. Kane, and S. Dawson, *The Higgs Hunter's Guide* (Addison-Wesley, Boston, 1990).
[18] E. N. Glover, J. Ohnemus, and S. S. Willenbrock, Phys. Rev. D **37**, 3193 (1988).
[19] T. Han and R.-J. Zhang, Phys. Rev. Lett. **82**, 25 (1999).
[20] T. Han, A. S. Turcot, and R.-J. Zhang, Phys. Rev. D **59**, 093001 (1999).
[21] M. Dittmar and H. K. Dreiner, arXiv:hep-ph/9703401.
[22] T. Aaltonen *et al.* (CDF Collaboration), Phys. Rev. Lett. **102**, 021802 (2009).
[23] T. Aaltonen *et al.* (CDF Collaboration), Phys. Rev. Lett. **104**, 061803 (2010).
[24] V. M. Abazov *et al.* (D0 Collaboration), Phys. Rev. Lett. **104**, 061804 (2010).
[25] T. Aaltonen *et al.* (CDF and D0 Collaborations), Phys. Rev. Lett. **104**, 061802 (2010).
[26] T. Aaltonen *et al.* (CDF Collaboration), Phys. Rev. Lett. **109**, 111804 (2012).
[27] V. M. Abazov *et al.* (D0 Collaboration), Phys. Rev. Lett. **109**, 121804 (2012).
[28] T. Aaltonen *et al.* (CDF Collaboration), Phys. Rev. Lett. **109**, 111803 (2012).
[29] V. M. Abazov *et al.* (D0 Collaboration), Phys. Rev. Lett. **109**, 121803 (2012).
[30] T. Aaltonen *et al.* (CDF Collaboration), Phys. Rev. D **87**, 052008 (2013).
[31] V. M. Abazov *et al.* (D0 Collaboration), Phys. Lett. B **716**, 285 (2012).

[32] T. Aaltonen *et al.* (CDF and D0 Collaborations), Phys. Rev. Lett. **109**, 071804 (2012).
[33] D. Hidas, Ph.D. thesis, Duke University [Report No. FERMILAB-THESIS-2008-83, 2008 (unpublished)].
[34] S. Pagan Griso, Ph.D. thesis, University of Padova [Report No. FERMILAB-THESIS-2010-62, 2010 (unpublished)].
[35] B. Carls, Ph.D. thesis, University of Illinois [Report No. FERMILAB-THESIS-2012-06, 2012 (unpublished)].
[36] H. M. Georgi, S. L. Glashow, M. E. Machacek, and D. V. Nanopoulos, Phys. Rev. Lett. **40**, 692 (1978).
[37] S. Dawson, Nucl. Phys. **B359**, 283 (1991).
[38] A. Djouadi, M. Spira, and P. M. Zerwas, Phys. Lett. B **264**, 440 (1991).
[39] M. Spira, A. Djouadi, D. Graudenz, and P. M. Zerwas, Nucl. Phys. **B453**, 17 (1995).
[40] R. V. Harlander and W. B. Kilgore, Phys. Rev. Lett. **88**, 201801 (2002).
[41] C. Anastasiou and K. Melnikov, Nucl. Phys. **B646**, 220 (2002).
[42] V. Ravindran, J. Smith, and W. L. van Neerven, Nucl. Phys. **B665**, 325 (2003).
[43] D. de Florian and M. Grazzini, Phys. Lett. B **674**, 291 (2009).
[44] C. Anastasiou, R. Boughezal, and F. Petriello, J. High Energy Phys. 04 (2009) 003.
[45] U. Aglietti, R. Bonciani, G. Degrassi, and A. Vicini, Phys. Lett. B **595**, 432 (2004).
[46] S. Catani, D. de Florian, M. Grazzini, and P. Nason, J. High Energy Phys. 07 (2003) 028.
[47] A. D. Martin, W. J. Stirling, R. S. Thorne, and G. Watt, Eur. Phys. J. C **63**, 189 (2009).
[48] S. Moch and A. Vogt, Phys. Lett. B **631**, 48 (2005).
[49] C. Anastasiou, K. Melnikov, and F. Petriello, Phys. Rev. Lett. **93**, 262002 (2004).
[50] C. Anastasiou, K. Melnikov, and F. Petriello, Nucl. Phys. **B724**, 197 (2005).
[51] S. Catani and M. Grazzini, Phys. Rev. Lett. **98**, 222002 (2007).
[52] M. Grazzini, J. High Energy Phys. 02 (2008) 043.
[53] C. Anastasiou, G. Dissertori, M. Grazzini, F. Stöckli, and B. R. Webber, J. High Energy Phys. 08 (2009) 099.
[54] J. M. Campbell, R. K. Ellis, and C. Williams, Phys. Rev. D **81**, 074023 (2010).
[55] S. Dittmaier *et al.* (LHC Higgs Cross Section Working Group), arXiv:1201.3084.
[56] I. W. Stewart and F. J. Tackmann, Phys. Rev. D **85**, 034011 (2012).
[57] M. Botje *et al.* (PDF4LHC Working Group), arXiv:1101.0538.
[58] S. Dittmaier *et al.* (LHC Higgs Cross Section Working Group), arXiv:1101.0593.
[59] J. Baglio and A. Djouadi, J. High Energy Phys. 10 (2010) 064.
[60] G. Ferrera, M. Grazzini, and F. Tramontano, Phys. Rev. Lett. **107**, 152003 (2011).
[61] K. A. Assamagan *et al.* (Higgs Working Group), arXiv: hep-ph/0406152.
[62] O. Brein, A. Djouadi, and R. Harlander, Phys. Lett. B **579**, 149 (2004).
[63] M. L. Ciccolini, S. Dittmaier, and M. Kramer, Phys. Rev. D **68**, 073003 (2003).
[64] P. Bolzoni, F. Maltoni, S.-O. Moch, and M. Zaro, Phys. Rev. Lett. **105**, 011801 (2010).
[65] E. L. Berger and J. M. Campbell, Phys. Rev. D **70**, 073011 (2004).
[66] M. Ciccolini, A. Denner, and S. Dittmaier, Phys. Rev. D **77**, 013002 (2008).
[67] M. Ciccolini, A. Denner, and S. Dittmaier, Phys. Rev. Lett. **99**, 161803 (2007).
[68] A. Bredenstein, A. Denner, S. Dittmaier, and M. Weber, Phys. Rev. D **74**, 013004 (2006).
[69] A. Bredenstein, A. Denner, S. Dittmaier, and M. Weber, J. High Energy Phys. 02 (2007) 080.
[70] G. D. Kribs, T. Plehn, M. Spannowsky, and T. M. P. Tait, Phys. Rev. D **76**, 075016 (2007).
[71] C. Anastasiou, R. Boughezal, and E. Furlan, J. High Energy Phys. 06 (2010) 101.
[72] L. Brucher and R. Santos, Eur. Phys. J. C **12**, 87 (2000).
[73] R. Blair *et al.* (CDF Collaboration), Report No. FERMILAB-PUB-96-390-E, 1996.
[74] F. Abe *et al.* (CDF Collaboration), Nucl. Instrum. Methods A **271**, 387 (1988).
[75] D. Acosta *et al.* (CDF Collaboration), Phys. Rev. D **71**, 032001 (2005).
[76] D. Acosta *et al.* (CDF Collaboration), Phys. Rev. D **71**, 052003 (2005).
[77] A. Abulencia *et al.* (CDF Collaboration), J. Phys. G **34**, 2457 (2007).
[78] Positions and angles are expressed in a cylindrical coordinate system, with the z axis directed along the proton beam. The origin of the coordinate system lies at the center of the detector. The azimuthal angle ϕ around the beam axis is defined with respect to a horizontal vector running outwards from the center of the Tevatron, and radii are measured with respect to the beam axis. The polar angle θ is defined with respect to the proton beam direction, and the pseudorapidity η is defined to be $\eta = -\ln[\tan(\theta/2)]$. The transverse energy and momentum of a particle are defined as $E_T = E\sin\theta$ and $p_T = p\sin\theta$, respectively.
[79] T. Nelson, Int. J. Mod. Phys. A **16**, 1091 (2001).
[80] C. S. Hill, Nucl. Instrum. Methods Phys. Res., Sect. A **511**, 118 (2003).
[81] A. Sill, Nucl. Instrum. Methods Phys. Res., Sect. A **447**, 1 (2000).
[82] A. A. Affolder *et al.*, Nucl. Instrum. Methods Phys. Res., Sect. A **453**, 84 (2000).
[83] A. A. Affolder *et al.*, Nucl. Instrum. Methods Phys. Res., Sect. A **526**, 249 (2004).
[84] L. Balka *et al.*, Nucl. Instrum. Methods Phys. Res., Sect. A **267**, 272 (1988).
[85] M. Albrow *et al.*, Nucl. Instrum. Methods Phys. Res., Sect. A **480**, 524 (2002).
[86] S. Bertolucci *et al.*, Nucl. Instrum. Methods Phys. Res., Sect. A **267**, 301 (1988).
[87] A. Bhatti *et al.*, Nucl. Instrum. Methods Phys. Res., Sect. A **566**, 375 (2006).
[88] A. Artikov *et al.*, Nucl. Instrum. Methods Phys. Res., Sect. A **538**, 358 (2005).
[89] D. Acosta *et al.*, Nucl. Instrum. Methods Phys. Res., Sect. A **461**, 540 (2001).

[90] D. Acosta *et al.* (CDF Collaboration), Phys. Rev. Lett. **94**, 091803 (2005).

[91] A. Abulencia *et al.* (CDF Collaboration), Phys. Rev. D **75**, 092004 (2007).

[92] D. Acosta *et al.* (CDF Collaboration), Phys. Rev. D **71**, 052003 (2005).

[93] D. Brun and F. Carminati, CERN Program Library Long Writeup Report No. W5013, 1993 (unpublished).

[94] T. Sjöstrand, S. Mrenna, and P. Skands, J. High Energy Phys. 05 (2006) 026.

[95] H. L. Lai, J. Huston, S. Kuhlmann, J. Morfin, F. Olness, J. F. Owens, J. Pumplin, and W. K. Tung (CTEQ Collaboration), Eur. Phys. J. C **12**, 375 (2000).

[96] J. Pumplin, D. R. Stump, J. Huston, H.-L. Lai, P. Nadolsky, and W.-K. Tung, J. High Energy Phys. 07 (2002) 012.

[97] T. Aaltonen *et al.* (CDF Collaboration), Phys. Rev. D **82**, 034001 (2010).

[98] S. Frixione and B. R. Webber, J. High Energy Phys. 06 (2002) 029.

[99] J. Alwall, M. Herquet, F. Maltoni, O. Mattelaer, and T. Stelzer, J. High Energy Phys. 06 (2011) 128.

[100] M. L. Mangano, M. Moretti, F. Piccinini, R. Pittau, and A. D. Polosa, J. High Energy Phys. 07 (2003) 001.

[101] U. Baur and E. L. Berger, Phys. Rev. D **47**, 4889 (1993).

[102] T. Binoth, M. Ciccolini, N. Kauer, and M. Kramer, J. High Energy Phys. 03 (2005) 065.

[103] S. Jadach, Z. Was, R. Decker, and J. H. Kuhn, Comput. Phys. Commun. **76**, 361 (1993).

[104] T. Aaltonen *et al.* (CDF Collaboration), Phys. Rev. D **84**, 071105(R) (2011).

[105] T. Aaltonen *et al.* (CDF Collaboration), Phys. Rev. Lett. **105**, 252001 (2010).

[106] T. Aaltonen *et al.* (CDF Collaboration), Phys. Rev. D **79**, 072010 (2009).

[107] T. Aaltonen *et al.* (CDF Collaboration), Phys. Rev. D **79**, 072001 (2009).

[108] A. Abulencia *et al.* (CDF Collaboration), Phys. Rev. D **74**, 032009 (2006).

[109] T. Aaltonen *et al.* (CDF Collaboration), Phys. Rev. Lett. **101**, 252001 (2008).

[110] T. Aaltonen *et al.* (CDF Collaboration), Phys. Rev. D **82**, 112005 (2010).

[111] T. Aaltonen *et al.* (CDF Collaboration), Phys. Rev. D **82**, 112001 (2010).

[112] T. Aaltonen *et al.* (CDF Collaboration), Phys. Rev. D **85**, 052002 (2012).

[113] T. Aaltonen *et al.* (CDF Collaboration), Phys. Rev. D **80**, 071101 (2009).

[114] S.-C. Hsu, Ph.D. thesis, University of California San Diego [Report No. FERMILAB-THESIS-2008-61, 2008 (unpublished)].

[115] J. M. Campbell and R. K. Ellis, Phys. Rev. D **60**, 113006 (1999).

[116] M. Feindt and U. Kerzel, Nucl. Instrum. Methods Phys. Res., Sect. A **559**, 190 (2006).

[117] A. Hoecker, P. Speckmayer, J. Stelzer, J. Therhaag, E. von Toerne, and H. Voss, Proc. Sci., ACAT (2007) 040 [arXiv: physics/0703039].

[118] L. Breiman *et al.*, *Classification and Regression Trees* (Wadsworth and Brooks, Monterey, CA, 1984).

[119] For this analysis the maximum number of trees is set at 400, the maximum allowed depth for each tree is 5 and each node is required to have at least 400 events. At each node the cut value is optimized by scanning over the variable range with a granularity of 20 steps. We use the Gini index as a separation criterion and apply the adaptive boosting algorithm [120] with a boosting parameter of 0.2.

[120] Y. Freund and R. E. Schapire, J. Comput. Syst. Sci. **55**, 119 (1997).

[121] S. Moch and P. Uwer, Nucl. Phys. B, Proc. Suppl. **183**, 75 (2008).

[122] A. D. Martin, R. G. Roberts, W. J. Stirling, and R. S. Thorne, Eur. Phys. J. C **28**, 455 (2003).

[123] J. Klimenko, J. Konigsberg, and T. M. Liss, Fermilab Report No. FERMILAB-FN-0741, 2003.

[124] J. Beringer *et al.* (Particle Data Group), Phys. Rev. D **86**, 010001 (2012).

[125] T. Aaltonen *et al.* (CDF Collaboration), Phys. Rev. Lett. **104**, 201801 (2010).

[126] T. Aaltonen *et al.* (CDF Collaboration), Phys. Rev. Lett. **108**, 101801 (2012).

[127] T. Aaltonen *et al.* (CDF Collaboration), Phys. Rev. D **86**, 031104(R) (2012).

[128] T. Aaltonen *et al.* (CDF Collaboration), following article, Phys. Rev. D **88**, 052013 (2013).

[129] T. Aaltonen *et al.* (CDF and D0 Collaborations), this issue, Phys. Rev. D **88**, 052014 (2013).